UNIVERSITY OF OSLO
Department of physics

Master's Thesis

Ion Implantation of ZnO by the Group IV elements Si and Ge: Doping, defects and nanocrystallization

Bjørn Brevig Aarseth

A thesis submitted in partial fulfillment of the requirements for the degree of MSc

in

Materials, Energy and Nanotechnology

May, 2016

Ion Implantation of ZnO by the Group IV elements Si and Ge: Doping, defects and nanocrystallization

Bjørn Brevig Aarseth

Abstract

Zinc Oxide (ZnO) is a promising material for future use in both solar cells as a transparent conductive oxide, in addition to a range of other electrical applications, due to its low cost, transparency, and electrical properties. Using ion implantation group IV elements Si and Ge have been implanted into a ZnO matrix, and annealed at a broad range of temperatures to monitor the lattice disorder caused by implantation, dopant characteristics, and potential for formation of nanostructures. Si implanted ZnO shows promising defect annihilation, and a crystal quality very close to that of virgin ZnO after annealing at 800°C. In addition donor activation is indicated already at room temperature by SSRM and hall effect measurements, making Si a promising candidate for implantation processing in ZnO. Ge implanted material shows similar dopant properties as Si, but high amounts of implantation damage, and precipitation of new phases at higher annealing temperatures makes it less suited for implantation doping. However, interesting observations have been done using TEM imaging, EELS, and EDS on precipitates formed during annealing at 800°C and 1000°C. Ge precipitations with a diameter of ∼10 nm enclosed by Zn_2GeO_4 is indicated by EELS and EDS after annealing at 800°C. After 1000°C Ge precipitations seem to be fully oxidized into Zn_2GeO_4, and ∼100 nm long and 20 nm wide rods of the same material, as well as other particle shapes of varied sizes, are observed using TEM imaging, and is further indicated by XRD.

Acknowledgements

The list of people i want to thank for everything they have done for me these last years is way too long. Firstly, I would like to thank my day-to-day and main supervisor, Assoc. Prof. Lasse Vines, for your patience regarding my constant flow of questions, my very last minute need of proof reading, and the SIMS characterization of many of my samples. Secondly, Prof. Bengt Gunnar Svensseon, for the valuable input during the work on my thesis, and that you introduced me to semiconductor physics. This thesis would never even have had a remote chance og being realized, if it was not for the two you, and for that I am immensely grateful.

A huge thanks goes to Heine Nygard Riise, who has stuck with me through hours of measurements, and for teaching me to use the XRD and Hall measurement techniques, in addition to carrying out some of my temperature dependent Hall effect measurements as well providing me with sputtered thin film samples. I would also like to thank Victor Bobal for carrying out ion implantation on my samples, Alexander Azarov for preforming RBS and SIMS on my samples, Augustinas Galeckas for the PL measurements you preformed for me, Jon Borgersen for the SSRM measurements, Torunn Kjeldstad for the SEM imaging, and Phuong Dan Nguyen and Cecilie Granerød for providing me with exquisite TEM imaging, EDS analysis, and EELS measurement results.

Finally, i would like to thank all my friends at LENS for making MiNaLab such a pleasant place to work and learn.

Contents

Chapter 1

Introduction

One of the biggest challenges facing humanity in the future is access to a sufficient amount of clean energy production. Electricity demand is predicted to rise by one third within 2040, primarily driven by Asian and African countries [1]. At the same time greenhouse gas emissions must be reduced by 40 to 70 % by 2050, compared to 2010 values, just in order to limit the global mean temperature increase to 2°C [2]. For this to be at all possible, a shift toward cleaner energy sources is paramount. For this, solar energy conversion using photovoltaics (PV) is an exceptional alternative. Development of a large scale industry in this field, primarily based on silicon (Si)-technology, has dramatically increased the energy production from PV worldwide, helping it on the way to become a viable alternative to fossil energy sources. There are however, a fundamental upper limit for single junction silicon based solar cells, called the Shockley-Queisser limit [3], impeding increased growth. It is possible to implement expensive tandem cells, intermediate band devices, hot electron extraction, and carrier multiplication (CM) to overcome these limits. Another approach could be to join todays well developed Si technology with some of these new concepts. For example it is possible to remove the anti-reflective coating used today, typically silicon nitride, and replace it with a transparent conducting oxide (TCO), to reduce shading from metal contacts and increase charge collection. A material showing great qualities in this respect is zinc oxide (ZnO), which is both relatively cheap compared to other alternatives and environmentally friendly. Further a coupling between this ZnO layer and a cuprous oxide(Cu_2O) layer as absorber could make a tandem cell on top of the original Si cell, and drastically increase conversion efficiencies. With better technology like this, solar power will be more than a competitive alternative to fossil fuels.

If it were possible to embed semiconducting nanocrystals into this ZnO TCO layer it could radically improve the cell performance. This was initially the main focus of this thesis. More accurately to ion implant germanium (Ge) into ZnO and try to form, and understand the formation of nanocrystals of this material and characterize them. Being able to control the formation and by that the size of the Ge particles could make tuning of the band gap possible, and light absorption could be controlled. The theoretical limit for single junction Si cells is around 30 %, use of photon down-converters can increase it to about 40 % and hot carrier effects could reach efficiencies of over 68 % at one sun [4, 5].

Interesting results in a preliminary sample series of Si implanted ZnO, meant as a reference, demanded further research, effectively dividing the thesis into two main parts: Si implanted ZnO and Ge implanted ZnO. Generally, IV impurities are relatively unexplored in ZnO, with

both Si and Ge as proposed donors, interesting for TCO and other device applications. Thus both elements were introduced in separate ZnO samples, annealed, and then characterized mainly structurally and electrically, with optical characterization only conducted on selected samples.

For the Si implanted series, the main focus has been on the electrical properties of Si as a dopant, and the amount of defects related to the implantation and presence of a large foreign atom concentration after annealing. Structural characterization were initially done using secondary ion mass spectrometry (SIMS), X-ray diffraction (XRD), and Rutherford backscattering spectroscopy (RBS), while electric characterization used were Hall effect measurements and scanning spreading resistance microscopy (SSRM). The Ge implanted samples were subject to the same investigation of Ge dopant properties in ZnO, but additionally early indications of new phases at annealing temperatures of 800°C and 1000°C required further structural analysis using scanning electron microscopy (SEM) and transmission electron microscopy (TEM). Optical analysis was carried out using photoluminescence (PL) spectroscopy and optical transmission spectroscopy.

Chapter 2

Theory

This chapter is initially focused on the general theory of crystalline materials, with an emphasis on semiconductors. It is meant as an introduction to solid state physics, and is somewhat crucial for the understanding of later techniques and results. Secondly the chapter discuss ZnO and relevant previous work done on similar material systems, meant to act as a basis and motivation for this thesis.

2.1 Crystalline Materials

This section is based on the references by Kittel [6], Hemmer [7], Griffiths [8], and Streetman [9].

Crystalline materials are comprised of atoms structured in a long range ordered fashion. In contrast to liquids and gases, the interactions between atoms are strong in crystals, and atom movement is strongly restricted. Long range order means that the atoms are stacked in a repetitive pattern throughout the crystal, clearly differentiating them from *amorphous materials* where there is no long range order, only a random structure. This repetitive pattern is often characterized through a materials crystal *lattice*.

2.1.1 Crystal lattice

Purely mathematical a lattice can be described in three dimensions using vectors $\mathbf{a_1}$, $\mathbf{a_2}$, and $\mathbf{a_3}$, not parallel or in the same plane, and combine them to represent all possible lattice points, $\mathbf{R}$, where

$$\mathbf{R} = n_1\mathbf{a_1} + n_2\mathbf{a_2} + n_3\mathbf{a_3} \tag{2.1}$$

and n_i are integers. If the vectors $\mathbf{a_1}$, $\mathbf{a_2}$, and $\mathbf{a_3}$, encapsulate the smallest possible volume in the lattice, $\mathbf{a_1}(\mathbf{a_2} \times \mathbf{a_3})$, they are said to be *primitive vectors*. There is always only one lattice point in a primitive cell. Some structures are easier described by non primitive vectors, and a bigger unit cell is chosen. A good example is the body centered cubic structure. Unit cells can be split into different types of lattices, depending on the symmetry. These different types are called *Bravais lattices*. In three dimensions there are 14 different types, including non primitive choices. To get a real structure a *basis* has to be defined and added to the lattice, like shown in two dimensions in Fig. 2.1. The basis can consist of one or more atoms, with fixed distance between each other.

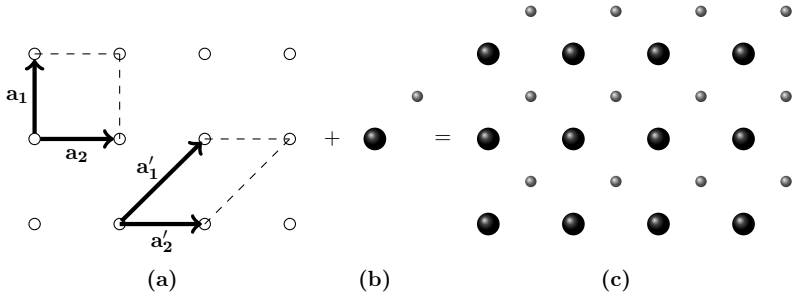

Figure 2.1: Here (a) shows the mathematic lattice, here both $\mathbf{a_1}$ and $\mathbf{a_2}$, and $\mathbf{a'_1}$ and $\mathbf{a'_2}$ span primitive cells, with the same volume, making both valid choices. (b) The basis, and (c) the structure as a combination of the basis and lattice.

In a crystalline material, being able to differentiate between different crystal planes can be very useful. To index each of these *Miller indices* are used, giving each plane a (hkl)-value. These are found by taking the reciprocal of the $n_{1,2,3}$-values where the plane in question intercepts the unit cell axes $\mathbf{a_{1,2,3}}$, respectively, and reducing this vector to its lowest possible integer numbers by division.

Reciprocal Space

A useful tool when working with material characterization is the *reciprocal space*. Reciprocal lattice vectors can be defined as

$$\mathbf{b_1} = 2\pi \frac{\mathbf{a_2} \times \mathbf{a_3}}{\mathbf{a_1} \cdot (\mathbf{a_2} \times \mathbf{a_3})} \; ; \quad \mathbf{b_2} = 2\pi \frac{\mathbf{a_3} \times \mathbf{a_1}}{\mathbf{a_1} \cdot (\mathbf{a_2} \times \mathbf{a_3})} \; ; \quad \mathbf{b_3} = 2\pi \frac{\mathbf{a_1} \times \mathbf{a_2}}{\mathbf{a_1} \cdot (\mathbf{a_2} \times \mathbf{a_3})}, \tag{2.2}$$

where $\mathbf{a_{1,2,3}}$ is the lattice vectors. If the lattice vectors are primitive, then b_1, b_2, and b_3 are the primitive reciprocal lattice vectors. As can be seen from the definition of the vectors,

$$\mathbf{a}_j \mathbf{b}_i = 2\pi\delta_{ij} \tag{2.3}$$

where if $i = j$, $\delta_{ij} = 1$ and if $i \neq j$, $\delta_{ij} = 0$. The reciprocal lattice can be expressed as the set of vectors

$$\mathbf{G} = v_1\mathbf{b_1} + v_2\mathbf{b_2} + v_3\mathbf{b_3}, \tag{2.4}$$

where v_i are integers.

The advantage gained by using the reciprocal lattice of a given lattice is that plane waves, on the form $e^{i\mathbf{G}\,\mathbf{r}}$, periodic with the given lattice can be easily made.

Diffraction

Diffraction of waves occurs for certain incident angles in crystalline materials. This theory is especially important for techniques like X-ray diffraction experiments and transmission electron microscopy, described in the next chapter. An incoming wave, $\mathbf{k}$, hits a lattice point and is diffracted into the outgoing wave $\mathbf{k'}$. This is regarded as an elastic scattering event, giving $\mathbf{k'}$ the same energy as $\mathbf{k}$. It can be shown that if the difference between the incoming and diffracted wave is equal to a reciprocal lattice vector,

$$\mathbf{k'} - \mathbf{k} = \mathbf{G} \tag{2.5}$$

there will be a peak in diffracted wave intensity. If the wave difference is not equal to $\mathbf{G}$ the intensity drops very fast. Equation 2.5 is called the Laue condition. By re-arranging the expression, it can be written as

$$2\mathbf{k} \cdot \mathbf{G} = G^2. \tag{2.6}$$

By inserting that $|\mathbf{k}| = 2\pi/\lambda$ and that the spacing between two parallel planes normal to $\mathbf{G} = h\mathbf{b_1} + k\mathbf{b_2} + l\mathbf{b_3}$ is $d(hkl) = 2\pi/|\mathbf{G}|$ the result is

$$2d(hkl)\sin\theta = \lambda, \tag{2.7}$$

where θ is the angle between the crystal plane and the incoming beam, and λ the incident beam wavelength. Here the hkl-values are not necessarily the same as in the Miller indices mentioned earlier, since they are not reduced to their lowest possible integer values. If it is assumed that they can be reduced by a factor n, the result is

$$2d\,\sin\theta = n\lambda, \tag{2.8}$$

called the Bragg condition.

Brillouin Zones

Equation 2.6 can be used as a starting point to introduce the concept of *Brillouin zones* (BZs). Dividing it by four gives

$$\mathbf{k}(\tfrac{1}{2}\,\mathbf{G}) = (\tfrac{1}{2}\,G)^2\,, \tag{2.9}$$

which is fulfilled when $\mathbf{k} = \frac{1}{2}\mathbf{G}$. Fig. 2.2 shows this for the two first possible $\mathbf{G}$ in the cubic lattice, and there by the two first Brillouin zones. For three dimensional structures like the

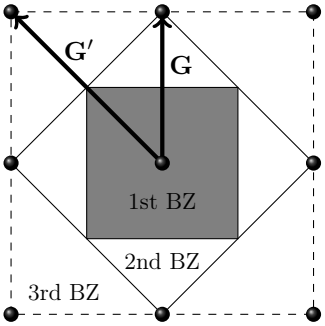

Figure 2.2: The 1st, 2nd and 3rd Brillouin zones for a cubic lattice.

body centered cubic, the BZs can become quite complex geometrical structures.

If the lattice parameter in the regular, cubic lattice, is a, then the value of G would be $G = 2\pi/a$, making $k = G/2 = \pi/a$ at the edge of the first Brillouin zone.

2.1.2 Electrical Properties of Crystalline Materials

To describe the electrical properties of crystalline materials the use of quantum mechanics is a necessity. Here particles can be described trough a wave function, $\Psi(x,t)$, which is found by solving the *Schrödinger equation*,

$$i\hbar\frac{\partial\Psi}{\partial t} = -\frac{\hbar^2}{2m}\frac{\partial^2\Psi}{\partial x^2} + V\Psi. \tag{2.10}$$

This is called the time dependent Schrödinger equation in one dimension, where i is $\sqrt{-1}$, t is time, $\hbar$ is Planck's constant divided by 2π, m is the particles mass and V is the potential in the vicinity of the particle. The wave function contains a lot of information about the particle. It has a statistical interpretation where

$$\int_a^b |\Psi(x,t)|^2 \, dx \tag{2.11}$$

is the probability of finding the particle between point a and b, at a time t. For this to work, the wave function has to be normalized, so that

$$\int_{-\infty}^{+\infty} |\Psi(x,t)|^2 \, dx = 1, \tag{2.12}$$

meaning that the probability of finding the particle in this interval is 100%. In addition it can be used to find expectation values of a range of parameters, like momentum, position etc., which again can be used to calculate the standard deviation of the parameter.

If the potential is assumed to be independent of t, it is possible to split the wave function in to two different parts,

$$\Psi(x,t) = \psi(x)\varphi(t), \tag{2.13}$$

where ψ is a function of x and φ a function of t. A time independent Schrödinger equation can be derived from this, with the form

$$-\frac{\hbar^2}{2m}\frac{\partial^2\psi}{\partial x^2} + V\psi = E\psi. \tag{2.14}$$

In the process the time dependent part can be shown to be

$$\varphi(t) = e^{-Et/\hbar}, \tag{2.15}$$

changing the wave function expression in equation 2.13 to

$$\Psi(x,t) = \psi(x)e^{-Et/\hbar}. \tag{2.16}$$

The same is valid for three dimensions, giving the following time independent Schrödinger equation,

$$\left[-\frac{\hbar^2}{2m}\nabla^2 + V(\mathbf{r})\right]\psi(\mathbf{r}) = E\psi(\mathbf{r}) \tag{2.17}$$

for a given position $\mathbf{r}$. In a perfect crystal, the potential, $V(\mathbf{r})$, will be periodic in position, meaning that

$$V(\mathbf{r}+\mathbf{R}) = V(\mathbf{r}), \tag{2.18}$$

if $\mathbf{R}$ is a lattice vector in the Bravais lattice. For this periodic potential the Bloch theorem says that solutions of equation 2.17 are the product of a plane wave and a function periodic with the lattice, $u_{\mathbf{k}}(\mathbf{r})$, on the form

$$\psi_{\mathbf{k}}(\mathbf{r}) = u_{\mathbf{k}}(\mathbf{r})\, e^{i\mathbf{k}\,\mathbf{r}}, \tag{2.19}$$

called Bloch eigenfunctions. This functions eigenvalue, E, is dependent on the wave vector $\mathbf{k}$ and the function will vary for different materials. $\mathbf{k}$ is as mentioned in the diffraction section

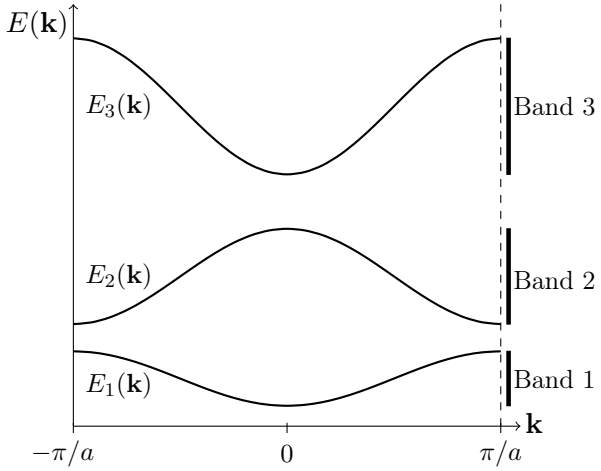

Figure 2.3: The energy plotted as a function of the wave vector, $\mathbf{k}$. The bands pictured to the right is a way to look at the band structure, ignoring the variations in $\mathbf{k}$, and looking at the available energies in the band as a whole.

coupled to the wave length of the wave, but can in addition be seen as the momentum vector, where $\mathbf{p} = \hbar\mathbf{k}$. Plotting $E(\mathbf{k})$ as a function of $\mathbf{k}$ will reveal energies available for electrons in a solid. These accessible states are called bands. Because of differences in expectation value for the potential energy of wave functions at certain $\mathbf{k}$, an energy gap, E_g, called band gap, will occur. $E(\mathbf{k})$ can be seen in Fig. 2.3. It is a result of the nearly free electron model, giving a first approximation to a materials band structure. More than one band can be seen because for every $\mathbf{k}$ in the material, there is expected to be more than one accessible energy level, just like for free particles within periodic boundary conditions, giving discrete levels $E_n(\mathbf{k})$, where $n = 1, 2, 3, \ldots$. When $\mathbf{k}$ changes the eigenvalues will change too, as seen in the Fig. below. The band structure of real materials is usually a lot more complicated than the figure shows, and will depend on what $\mathbf{k}$ directions it is plotted in. Normally these are shown by plotting $E_n(\mathbf{k})$ through chosen points in the materials 1st Brillouin zone.

The number of electrons in the system depends on the number of primitive unit cells in the sample, N, and how many valence electrons each cell contributes with. Every primitive cell gives one independent value of $\mathbf{k}$ in the energy band, and by adding spin that gives $2N$ possible states in each band.

Depending on the band structure and the electronic filling of bands, materials can be put in three different categories; metals, semiconductors, and insulators. What category a material belongs to, depend on the band environment around the highest occupied energy levels. Different types of environments can be seen in Fig. 2.4. When a filled, or almost filled, band overlaps with another band, giving electrons small transition energies to a high density of free states, the material will be conducting current quite easily (2.4a). The same goes for a half filled band (2.4b). These materials are called metals. If the highest occupied band is filled, with an energy gap up to the next available states in the next band, the material is called a semiconductor or an insulator, depending on the energy gap width (2.4c). It is often said that a band gap above $\sim 5 - 6\,eV$ is an insulator, but there are no abrupt transition between the two. A better way of separating the terms could be the amount of charge carriers. E.g. the semiconductor germanium will be insulating at zero kelvin, while it has a concentration of about $\sim 5 \times 10^{13} cm^{-3}$ at room temperature, making it conducting. Materials with larger

band gaps will have lower carrier concentrations at a given temperature, making them less conducting, and vice versa.

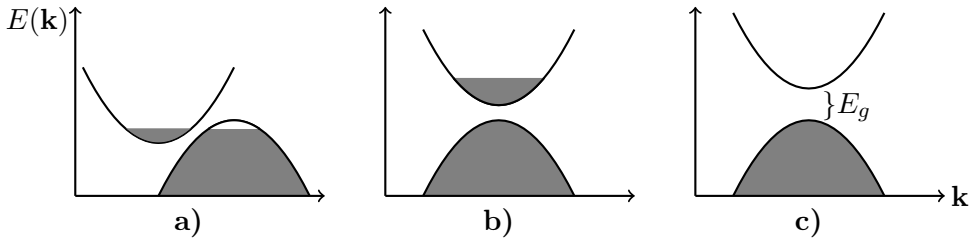

Figure 2.4: Showing the different band structures for a) a metal with overlapping bands b) a metal with a half filled band, and c) a semiconductor/insulator depending on the band gap, E_g, size.

2.2 Semiconductors

This section is based on the references by Kittel [6] and Streetman [9].

Semiconductors can be split in to two different categories; direct and indirect band gap semiconductors. Excitation paths for the two are shown in Fig. 2.5. The indirect gap (2.5a)

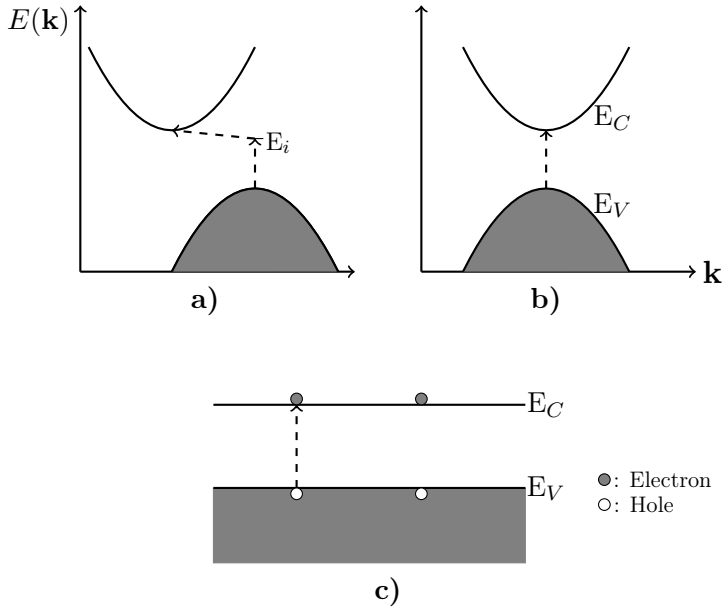

Figure 2.5: Excitation of a) an indirect, and b) a direct band gap. c) shows an excitation in a simplified band diagram independent of **k**, only illustrating the band gap size. In addition electron-hole pairs are pictured.

requires an addition of momentum (change in **k**, referred to as a phonon) to reach the upper band. This often takes place through an intermediate energy level inside the band gap, E_i, caused by defects in the material. In direct band gap (2.5b) materials the transition goes without a phonon, making this an easier transition, and thus more likely than the indirect transition.

2.2.1 Charge Carriers

In an ideal semiconductor, the only charge carriers present are excited from the lower band in Fig. 2.5, called the valence band (E_V), to the upper band, called conduction band (E_C). As a consequence, an electron-hole pair (EHP) is formed, where holes are the empty states left from excited electrons (Fig. 2.5c). Considering the hole as a charge carrier in the valence band is useful for describing the electron movement. It becomes a net positive particle moving in the opposite direction of the electrons. Mathematically it is a simplification, because instead of considering all electrons in the almost full band, only the states where electrons are missing are considered, without loosing any information about the system. Generation of EHPs are done by adding energy to electrons in the valence band, giving them enough to transfer over the band gap. This generation can be thought of as electrons being excited from their bound state between atoms in the material, becoming free electrons. EHPs can be generated thermally, from optically and more.

An ideal semiconductor like as presented above is called an *intrinsic material*. This is because electrons and holes are created in pairs,i.e. the electron concentration in the conduction band, n (electrons per cm^3), and the hole concentration in the valence band, p (holes per cm^3), are equal, and often written

$$p = n = n_i. \tag{2.20}$$

Here n_i is the intrinsic carrier concentration at a given temperature, usually 25°C, which, in an ideal semiconductor, is the concentration of EHPs thermally generated.

In order for the semiconductor to reach an equilibrium carrier concentration, these EHPs have to recombine after a certain time, to avoid a build up of EHPs. Electrons in the conduction band will drop down over the band gap, into the valence band, and recombine with a hole. This means that the generation rate g and the recombination rate r, have to be equal;

$$g = r \tag{2.21}$$

for equilibrium to occur.

The concentration of charge carriers in a semiconductor is easily manipulated. By modifying the number of charge carriers in a material the conductivity changes. This is called *doping* of semiconductors, done by adding a guest species (dopant) with either more or fewer electrons into the host material. If the dopant has more electrons, it is called n-doping, and the material ends up with an excess of free electrons. The opposite is p-doping, where the dopant has fewer electrons, giving the material an excess of holes. Both are illustrated in Fig. 2.6.

Semiconductor doping introduces new states into the band structure. N-doping adds *donor*-, and p-doping *acceptor*-states, shown in Fig. 2.7. The donor states come from the loosely bound fifth electron pictured by the n-dopant in Fig. 2.6. Very little energy is required to remove it from the dopant-atom, making it free to move. This is analog with it being excited from the donor state and into the conduction band. Since the electron is loosely bound, the donor-states are located close to the conduction band minimum. Acceptor states are similar, except these are located close to the valence band maximum, and are initially empty. Only a small amount of energy is needed to excite electrons from the valence band into these empty states, leaving behind holes. At zero kelvin the donor band will be full, with no excitations into the conduction band, and the acceptor band will be empty. As temperature is increased more excitations will happen, and charge carriers are generated, increasing the conductivity of the material.

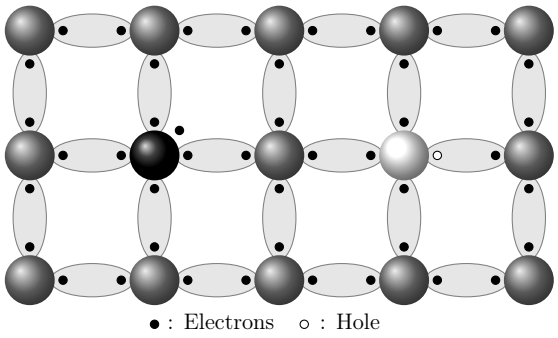

Figure 2.6: A 2D illustration of n-doping (white) and p-doping (black) in a material. The red n-type dopant adds an electron, while the p-type adds a hole by having fewer electrons than the host.

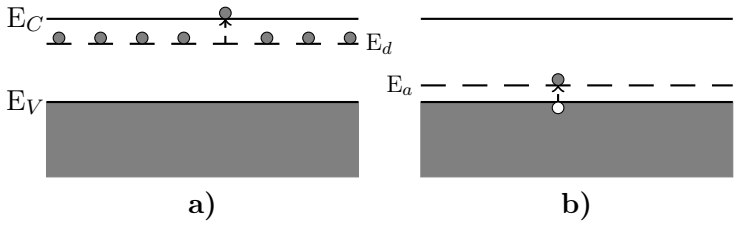

Figure 2.7: Energy band model including a) donor- and b) acceptor-levels. The donor band, E_d, is close in energy to the conduction band. Acceptor levels are close to the valence band.

Charge Carrier Concentrations

The charge carrier concentration, usually given in carriers/cm^3, is an important quantity for most of the electrical properties in semiconductors, thus keeping track of it is an important task. Fortunately, electrons follow what is called *Fermi-Dirac* statistics, making it possible to calculate electron energy positions using

$$f(E) = \frac{1}{1 + e^{(E-E_F)/kT}}\,, \tag{2.22}$$

where k is Boltzmann's constant, and E_F is the *Fermi level*. This Fermi-Dirac distribution gives the probability of an energy level E being occupied at a given temperature, T. At the Fermi level energy E_F, the probability of an electron occupying a state is $1/2$. The probability of some energy state E being empty then corresponds to $[1 - f(E)]$, which is the probability of finding a hole at this energy. Higher temperatures will increase the carrier concentration, see Fig. 2.8. The Fermi level position energy will change when the material is doped. N-doping will increase its position, while p-doping will lower it. The consequence of this is, as seen earlier that an electron is more likely to be in the conduction band in an n-doped material, and holes more likely to be in the valence band in p-doped materials.

To calculate carrier concentrations using Fermi-Dirac statistics the *density of states* (cm^{-3}) has to be known. Using this the carrier concentration in the conduction band at equilibrium could be expressed as:

$$n_0 = \int_{E_C}^{\infty} f(E)N(E)dE\,, \tag{2.23}$$

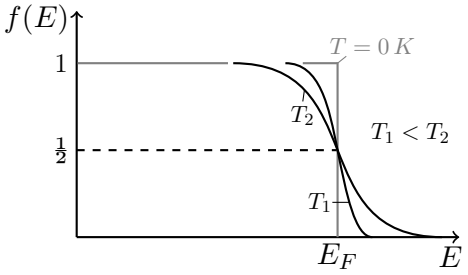

Figure 2.8: Plot of the Fermi-Dirac distribution.

where $N(E)dE$ is the density of states in the energy range dE. For holes in the valence band this becomes

$$p_0 = \int_{-\infty}^{E_V} [1 - f(E)]N(E)dE\,. \tag{2.24}$$

The result of these integrations can be written

$$n_0 = N_c f(E_C). \tag{2.25}$$

Here N_c is the effective density of states at the conduction band edge, and $f(E_C)$ is the probability of electron occupation at the conduction band edge. This is a simplification, but the Fermi-Dirac function falls to zero quickly over E_C, making it a good approximation. It can be simplified further, using

$$f(E_C) = \frac{1}{1 + e^{(E-E_F)/kT}} \simeq e^{-(E_C-E_F)/kT}\,, \tag{2.26}$$

which is a good approximation if $(E - E_F)/kT >> 1$. Using this, equation 2.25 becomes

$$n_0 = N_c e^{-(E_C-E_F)/kT}. \tag{2.27}$$

Through similar approximations it can be shown that

$$p_0 = N_v e^{-(E_F-E_v)/kT}, \tag{2.28}$$

where N_v is the effective density of states at the valence band edge. Further, in an intrinsic material, the Fermi level, E_F, will be equal to an intrinsic level, E_i, located around the center of the band gap. This makes the product of the intrinsic concentrations, n_i and p_i, look like

$$n_i p_i = (N_c e^{-(E_C-E_F)/kT})(N_v e^{-(E_F-E_v)/kT}) = N_c N_v e^{-E_g/kT}. \tag{2.29}$$

The same way the product of the equilibrium concentrations becomes

$$n_0 p_0 = N_c N_v e^{-E_g/kT}. \tag{2.30}$$

Combining these two gives

$$n_0 p_0 = n_i^2, \tag{2.31}$$

a very useful expression for calculations of carrier concentrations in doped semiconductors.

For extrinsic materials this means that the donors or acceptors will be activated at a certain temperature making the intrinsic charge carrier generation negligible for a certain temperature range, called the extrinsic or operation regime of the semiconductor. At high enough temperatures a large amount of charge carriers can be excited over the band gap, and thus make the extrinsic concentration negligible, leaving the doping ineffective and the semiconductor effectively intrinsic.

Charge Compensation

Once a semiconductor is doped, e.g. using acceptor atoms, it is possible add donors to such an extent that the semiconductor becomes n-doped. This means that if both acceptor and donor atoms present, it is possible to type inverse the material from p- to n-type, by compensating all acceptors with donors, and if more is added the material becomes n-doped. This can be seen through the requirements of space charge neutrality in materials. In order for a material to be neutral, it has to fulfill

$$p_0 + N_d = n_0 + N_a \,, \tag{2.32}$$

where N_d and N_a are the ionized dopant atom concentration (cm^{-3}).

Mobility and Conductivity

In semiconductors doping and defects in general will alter the electrical properties of the material, more specifically it will change the *conductivity* of the sample. More defects degrade the periodic potential in the material, causing increased scattering and a degradation of the *mobility*, i.e. the ease at which electrons move through the material when an electric field is present. These are very important values as it comes down to how well samples conduct electricity. Especially hall measurements, presented in section 3.8.

The conductivity, σ and resistivity, ρ, of a material containing both electron and hole carriers are defined as

$$\sigma = q(n\mu_n + p\mu_p) \;\; \rho = 1/\sigma \tag{2.33}$$

where q is the electron charge, $n\,(p)$ is the electron (hole) concentration, and $\mu_n\,(\mu_p)$ is the electron (hole) mobility of the material. The resistivity of a material is the most used measure of merit for TCOs and a range of other devices when it comes to electrical properties of the used material.

The mobility will vary with temperature as well as the concentration of impurities, and by that change the conductivity of the sample. As temperature increases, as will lattice vibrations, and the amplitude of these. This will increase charge carrier scattering, and reduce the mobility. At the same time impurity scattering will reduce with increasing temperature because of an increase in the thermal motion of electrons. This means that at low temperatures the thermal motion of electrons will be slow, causing electrons to be scattered more by charged defects and impurities than at higher temperatures, where the velocity is larger.

Impurity and thermal scattering are two possible mechanisms that can dominate in a semiconductor at given temperatures. Depending on what kinds of defects are present in the material, the mobility as a function of temperature can vary. The total mobility of a material can be approximated as

$$\frac{1}{\mu} = \frac{1}{\mu_1} + \frac{1}{\mu_2} + ... \tag{2.34}$$

This is called Matthiessen's rule, where $\mu_1, \mu_2, ...$ denotes mobility contributions from different scattering mechanisms and each scattering mechanism is assumed independent of other mechanisms. This means that the scattering mechanism that contributes with the lowest mobility will be the dominant scattering mechanism, and limit the mobility of the material. At different temperatures different mechanisms can dominate, e.g. at low temperature the mobility can increase with temperature because of reduced impurity scattering, but at a certain temperature lattice vibrations will begin dominating, and the mobility will begin to decrease with temperature.

2.3 Nanocrystals

This section is based on the references by Alivisatos [10] and Beard [11].

When the size of semiconductor crystals are reduced sufficiently, often to below what is called the Bohr exciton radii of the material, intrinsic properties become size and surface dependent. This means that nanocrystal (NC) properties, e.g. band gap, can be tuned by varying the crystal size, making NCs a very interesting subject for a range of applications within solar cells and other electronic devices. In this section the NC physics will be briefly explained.

2.3.1 The Effect of Size

A bulk semiconductor will follow the physics explained in the previous, and have near a continuous energy level distribution in its bands, interrupted by band gaps in between. For a NC the confinement produces discrete energy states in the valence and conduction band. The difference between the two can be seen in Fig. 2.9a). The quantization causes the effective

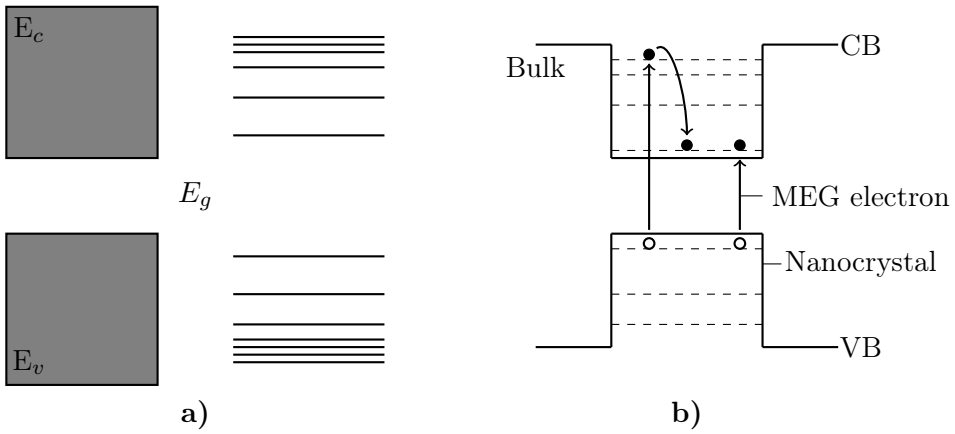

Figure 2.9: **a)** In a bulk semiconductor (left) there is continuous bands of energy states, while in a NC there is discrete quantized states in both the valence and conduction band. **b)** A simplified band diagram showing a NC incorporated in another semiconductor. The dashed lines are the quantized energy levels inside the crystal, and the multiple exciton generation (MEG) process is exemplified.

band gap of the material to increase, and the smaller the NC the bigger confinement and thus band gap. This is often viewed in terms of the exciton bond length of the material. Coulomb forces act between electrons and holes, creating an effective bond, forging an exciton. For crystal sizes below this exciton bond length, the exciton becomes confined, and its energy increase. Exciton bond length varies with material.

Potential use in Applications

Fig. 2.9b) shows a simplified picture of an embedded NC in a bulk semiconductor with a bigger band gap. Multiple exciton generation (MEG) is exemplified as well. In this process one electron is excited across the NC band gap with an energy surpassing, or at least equal to, $2E_g$. In stead of thermalizing down to the CB edge, as would usually happen in a bulk semiconductor, and give the excess energy off as heat, it is used to excite a second electron

in to the conduction band of the NC. This happens through impact ionization, where the energetic electron interacts with the electron in the valence band and transfers the excess energy to the second electron, giving it energy enough to transfer to the conduction band. By exciting an electron with an energy equal to, or larger than, 3Eg or 4E$_g$, two or three, respectively, extra EHPs could be excited. In an application like a solar cell this could greatly increase the absorption, and thus substantially increase efficiencies, by e.g. down converting a photon of 2E$_g$ to two photons of energy E$_g$.

2.4 Zinc Oxide

In this section some basic properties of Zinc Oxide (ZnO), including structural and electric properties, will be presented. Mainly the section is based on the references by Özgür et al. [12], McCluskey and Jokela [13], and Claflin and Look [14] with some specific references in the text.

2.4.1 Materials Properties

ZnO inhibits the wurtzite crystal structure, seen in Fig. 2.10, at ambient conditions. Here each Zinc atom is surrounded by four oxygen atoms, and vice versa, in a tetrahedral configuration. It is described by the lattice parameters a, b and c, where $a = b \approx 3.25$Å and $c \approx 5.20$Å [15,16].

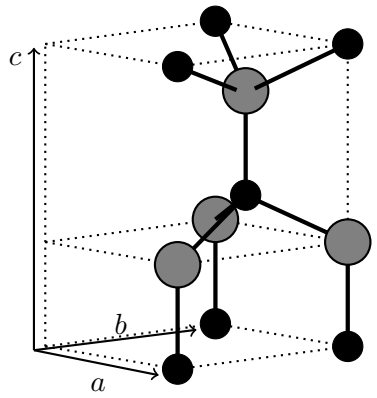

Figure 2.10: Schematic of the wurtzite structure of ZnO.

The band gap is wide, ∼3.4 eV, at room temperature and direct [17]. It is commonly an n-type material [18], and is proving very difficult to p-type dope. The n-type doping is still a subject of discussion, where some blame O vacancies (V_{O}), others blame Zn interstitials (Zn_{i}). V_{O} has a low formation enthalpy in p-type material, and might be a compensating defect hindering the formation, but the donor energy is calculated to be too deep to contribute much with n-doping. The Zn_i are unstable at room temperature, and has a high formation energy, but some interstitial complexes involving it has been proposed as a possible shallow donor, e.g. both $\mathrm{Zn_i}$-$\mathrm{Li_O}$/N_O and $\mathrm{Zn_i}$-$\mathrm{V_O}$ [18,19]. In addition first principle calculations have shown that hydrogen (H) should have a shallow donor energy, which has been confirmed by several experiments [20,21]. Fabrication of ZnO not containing the highly mobile H-atom proves very hard, making it a viable candidate.

When it comes to intentional n-doping of ZnO, it has been shown to be considerably easier than p-doping. Most group III elements, B, Al, Ga, and In have shown to be good donors, and

most are quite well researched [22–26], all easily capable of giving rise to carrier concentrations above 10^{20} cm^{-3}. Often one or more of these efficient donor atoms are found as non-intentional impurities in ZnO, and can thus contribute the native n-type of ZnO material.

2.4.2 Growth

The three most favored growth techniques for bulk ZnO are melt, vapor phase and, hydrothermal (HT) growth. High vapor pressure of ZnO makes melt growth challenging, and the vapor phase deposition can be difficult to control. But low super-saturation in solution makes HT growth a viable candidate, and resulting in very good single crystals. The experimental setup is quite simple, where single crystal seeds suspended in a solution, saturated from nutrient ZnO, by wires. Using the right pressure and catalysts the seeds grow into big single crystals over time. Downsides to this method is that the growth rate can be low, meaning that growth of large crystals are time consuming. Secondly quite large concentrations of alkali metals, like potassium and lithium, are incorporated into the crystals.

When it comes to thin film growth of ZnO it has been shown that there exists a strongly preferential growth on various substrates in the (0001) direction. This causes films made by magnetron sputtering, chemical vapor-deposition, etc. to all show a preferential orientation in the (0001) direction on different substrates like silicon, glass, sapphire, and diamond.

2.5 Previous Work

Articles have over the years stated that too little research has been done using IV-elements in ZnO [12], but there are still some information on certain material systems. These will be presented in this section. Additionally, research done on implantation damage and effects of subsequent annealing of ZnO will also be presented.

2.5.1 Implantation and annealing of ZnO

For many devices selective area implantation is a key step in device processing. To understand the effects of radiation damage on the materials properties is thus important. Work done by Vlasenko and Watkins [27] and Kucheyev et al. [28] show that ZnO is quite radiation hard, and a lot of annealing occurs even at low temperatures. The former suggested that Zn interstitials (Zn_i) are mobile at temperatures below room temperature (RT), causing recombination with Zn vacancies (V_{Zn}). Some damage remains, both in the Zn sublattice and O sublattice, and problems arise related to distinguishing between these intrinsic defects. Thus it is often referred to as a overall implantation damage or disorder, often measured using RBS. In addition implantation of ZnO has been shown to produce effective isolation, by introducing acceptor-like defects, both at high and low ion doses [29–32].

HT grown Tokyo Denpa samples, as used in this thesis, often contain high concentrations of Li. This strongly affects the sample resistivity, as Li can occupy both interstitial (Li_i) and Zn lattice (Li_{Zn}) positions, where Li_i is a donor and Li_{Zn} an acceptor. This was studied by Vines et al. [33]. They found that in n-type samples the Li_{Zn} configuration was dominant, supported by Johansen et al. [34], causing an acceptor like behavior. Heat treatments does however reduce the Li concentration quite sufficiently, and thus resistivity. Further Neuvonen et al. [35] looked at how Li profiles and resistivity in the implanted region changed as the material was implanted with various species, and heat treated at a range of temperatures

using SIMS and SSRM. Samples implanted with the inert species Ar and Ne, yielding about the same amount of defects, showed no Li depletion. Samples implanted with Zn however, was depleted of Li at depths beyond R_p at annealing temperatures above or equal to 600°C, and showing a reduced resistivity. O implanted samples showed an accumulation of Li at R_p and increased resistivity. Using this information they concluded that Zn_i was released during annealing in the Zn-implanted samples, forcing Li_{Zn} into the highly mobile interstitial configuration, leading to Li depletion. The same way they concluded that O_i was a stable acceptor in the O-implanted samples. This work was supported by Azarov et al. [36], using the Li concentration to monitor preferential sublattice occupation of a range of implanted impurities.

2.5.2 Doping with IV materials Si and Ge in ZnO

Si has been shown to act like a donor in ZnO. Riise [37] showed that Si-doping gave close to the same results as Al-doping, a known ZnO n-type dopant [17, 38–43]. In addition density functional theory (DFT) studies [44, 45] have shown that Si_{Zn} by far is the most stable configuration, as compared to Si_O and Si_i. In this configuration it is expected to exhibit a double donor state, Si_{Zn}^{2+}. This has yet to be shown experimentally, but this could of course be due to the complicated compensating nature of certain defects in the ZnO material.

Further experiments by Schofield [46] and Lai et al. [47] both reported carrier concentrations above 10^{20} cm^{-3} in ZnO film co-sputtered with Si. In the latter resistivity was decreased from 10^2 Ω cm in pure ZnO film, to 8.5×10^{-3} Ω cm in a ZnO film containing 0.5 atom% Si. Das et al. [48] reported a resistivity of 6.2×10^{-4}Ω cm at ∼1 atomic% Si, and observed an increase in ZnO band gap at high levels of doping, using absorption and PL measurements. This was related to a high carrier concentration-induced Burstein-Moss blue shift. This is, to some extent, in agreement with Liu et al. [49], who proposed a band gap increase in ZnO due to Si doping using DFT. Using Si ion implantation Izawa et al. [50] reported a resistivity of ∼5×10^{-3} Ω-cm in Tokyo Denpa high resistive ZnO samples. They assigned the low resistivity to Zn_i-complexes formed due to implantation, proposed to be observed by PL at an emission energy of 3.33 eV.

As to the doping effect of Ge, it is by DFT expected to be of the same character as Si doping [44]. The Ge_{Zn}^{2+} is calculated to be the most stable site for Ge as well. Also using DFT Lv et al. [51] proposed that the doping effect of Ge would induce a Burstein-Moss blue shift in the material. Secondly they proposed that Ge would tend to cluster at high doping percentages, which might cause a reduction in conductivity of the samples. Experimental studies on the electrical properties of Ge doped ZnO seem to be scarce, but one article on the matter has been published by Kamioka et al. [52]. They reached a resistivity of 9.09×10^{-3} Ω-cm, after a high concentration Ge box implant and subsequent annealing of highly resistive ZnO at 800°C. As-implanted samples had a resistivity of 1.45×10^{-2} Ω-cm. The origin of the low resistivity was attributed to Zn_i in the as implanted, and both Zn_i and activated Ge donors in samples annealed at 1000°C, by using RBS and attributing PL emission of 3.33 eV to the thermally activated Ge donor.

2.5.3 Nanocrystals of group IV elements Si and Ge in ZnO

A lot of effort has previously been put into Si doping of ZnO, with the aim of producing Si nanocrystals incorporated into the ZnO matrix. Effects like MEG and down-conversion of pho-

tons could drastically improve efficiency of photovoltaics. Lai et al. [47] reported fabrication of Si nanocrystals using co-sputtering of Si and ZnO at varied Si target RF voltages, without heat treatment of the samples. XRD, FTIR, and PL all showed presence of nanocrystals. Schofield [46] used co-sputtering of Si and ZnO, followed by annealing, and by characterizing using HRTEM Si nanocrystals was thought to be confirmed. This was later put in question by Riise [37], and the Si reflections were attributed to ZnO. The same work concluded that formation of Si nanocrystals at high annealing temperatures were highly unlikely due to the low formation energy of SiO_2, making this phase more energetically favored than a pure Si precipitate.

Ge NCs have been proposed as a viable candidate for MEG as well. DFT studies of NCs in host matrices and hydrogenated in vacuum show that Ge has great potential [53–55], but there are few experimental articles published on the subject thus far. There are, however, an increasing amount of articles being published on Ge NC synthesis in ZnO matrices, and characterization of these [56–62].

Yu et al. [56] did an experiment using a solid state reaction between ZnO and GeO_2 powder at 1100°C for six hours. XRD showed that at above 0.7 mol% GeO_2, a Zn_2GeO_4 phase emerged, and this was suggested as the solubility limit of Ge in ZnO. Further PL-studies showed a blue shift in samples containing up to 0.7 mol% Ge, samples with a Ge concentration above this was red shifted. The blue shift was explained as a Burstein-Moss shift, i.e. a band filling effect caused by Ge doping. The red shift was attributed to a band tail, caused by an excessively high donor concentration, leading to an effective reduction of the bandgap energy. Zheng et al. [57] made multilayer films of ZnO and Ge using RF-sputtering, and annealed at temperatures from 550-680°C. They too observed a Zn_2GeO_4 phase using XRD, with the amount increasing at higher temperatures, in addition to some Ge crystallites. Three main emission peaks were visible from 500-900 nm using PL, and they were attributed to transitions between V_O^* and V_{Zn}(532nm), recombinations in quantum confined Ge excitons from nanocrystals (700nm), and optical transitions in GeO color centers (761nm), respectively. A red shift is seen in the 700 nm peak at the higher temperatures, associated with a growth in Ge nanocrystals. This is in direct conflict with what Pal et al. [58] reported in 2003, where they saw a decrease in Ge nanocrystal size at higher annealing temperatures. In addition the article by Fan et al. [59] speculates that GeO color centers in their rf sputtered layered samples are found at a wavelength of 395nm, annealed using rapid thermal annealing. Jiang et al. [60] reported a PL peak at 548 nm in samples of co-sputtered ZnO and Ge on quartz. These were attributed to color centers of Ge in Zn_2GeO_4 grains.

To sum up, mostly optical characterization has been done on co-sputtered or sequential layer sputtering of Ge and ZnO, with very varying results and opinions. Literature on other approaches are scarce, and no real consensus seems to have been found, motivating further research on the subject.

Chapter 3

Experimental Methods

This chapter is devoted to explaining the key experimental fabrication, as well as characterization techniques used in this thesis. The first two sections are devoted to fabrication, while the rest are characterization techniques. The latter is arranged from structural, electrical, and lastly optical techniques, respectively.

3.1 Sputtering Deposition

This section is based on the reference by Campbell [63].

Material *sputtering* is an application of many uses, like surface etching, material analysis (SIMS), and thin film deposition. The latter has proven a very applicable deposition method both in research and production.

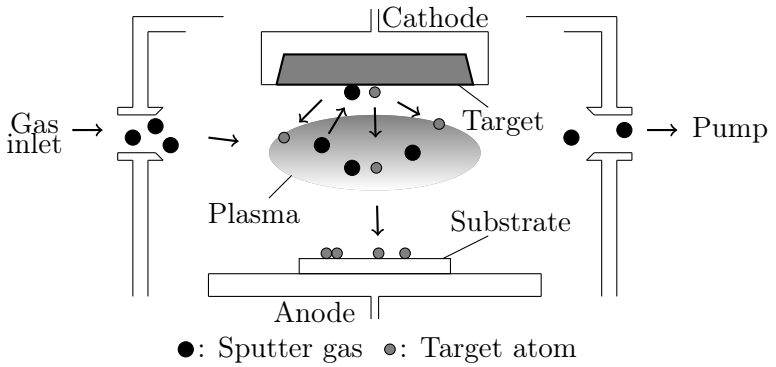

Figure 3.1: Schematic of the sputtering setup and principles.

The experimental setup, seen in Fig. 3.1, consists of a chamber containing a cathode with the sputtering target and an anode where the substrate is mounted, usually with a small distance, e.g. ~ 10 cm, apart. The sputtering target consists of the thin film material being deposited on the substrate. Before a deposition the chamber is evacuated and filled with an inert sputter gas, like e.g. argon (Ar), at a pressure usually lower than the ambient. A large voltage is applied between the anode and cathode, ionizing the Ar gas, essentially creating a plasma. The resulting electrons are accelerated towards the positive anode, ionizing more Ar atoms, while the remaining positive Ar ion is accelerated towards the target. If the incoming Ar ions energy is sufficient they will sputter, i.e. knock out, the target atoms. If the energy is

too the ion will be implanted, and if it is low it will be reflected or physisorbed on the surface. If sputtered, the target atoms will be accelerated in all directions, like a pool break shot, and some will end up at the substrate, forming a film.

This mode is called direct current (DC) sputtering and is suitable for conducting targets. If the target is isolating, or not sufficiently conducting, the constant addition of electrons to the anode and positive ions on the cathode will result in a charge build-up, essentially extinguishing the plasma, and stop the deposition. For these kind of materials radio frequency (RF) sputtering is used. Here the voltage oscillates, changing polarization at radio frequency, meaning that each electrode is bombarded with ions and electrons subsequently, thus avoiding charging effects. Normally this would sputter the film just as much as the target, but by increasing the anode to cathode area ratio, the substrate will be sputtered less, and an effective film deposition is possible. DC sputtering usually has larger sputter rates, making it favorable when possible.

Ionization probability of the plasma can be increased by adding a magnetic field in to the chamber, making the electron paths longer, and increasing the possibility of ionizing more Ar-atoms on their way. This is called magnetron sputtering.

All of this makes sputtering a very versatile deposition technique, capable of depositing on a wide range of materials.

3.2 Ion Implantation

This section is based on the references by Campbell [63] and Morgan [64].

Ion implantation is a well researched and powerful tool to introduce impurities into a target material. In the semiconductor industry it has been a common technique to dope materials, because the implantation depth is easy to control. Additionally implantation profiles not possible through surface diffusion become available. A downside is that very shallow or deep profiles can be challenging, and that large amounts of defects are usually generated. A possible implantation setup is shown in Fig. 3.2.

Ions are made from a feed gas, or vapor from a solid source, by running it trough a voltage difference, making a plasma. The ions are accelerated further into the apparatus with an even higher voltage difference. The ion energy is dependent of the acceleration voltage, and it thus

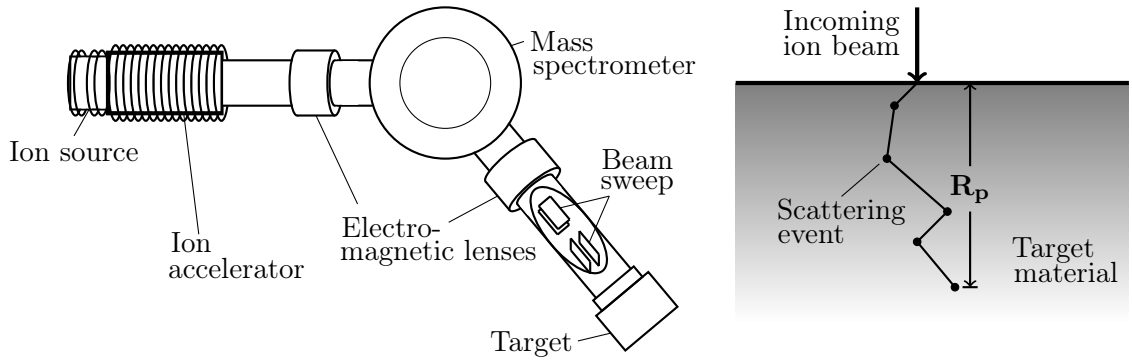

Figure 3.2: The left figure shows a schematic of an ion implantation setup. The right figure shows the difference between the R_p of the incident ion beam ions and the path length they have inside the material.

decides how far into the target material the ions are implanted. The mass separator uses a magnetic field to separate the incoming ions, only letting the ones with the right velocity, mass and charge through the bend in the setup. Basically making it a mass spectrometer. It is even possible to separate different isotopes of the ion. It follows the formula

$$\frac{Mv^2}{r} = qvB. \tag{3.1}$$

The electromagnetic lenses focuses the beam, making divergent ion paths converge. Beam sweeping is not present in all implanters, but it makes it possible to raster a well converged ion beam over the target, making the implantation very uniform. It is done by controlling a voltage between the plates, bending the beam in different directions depending on the voltages of the two pairs of plates (Fig. 3.2). Finally there is the target/sample holder, cotaining the sample.

When an ion is traveling through the material it will be scattered by both nucleus and electrons, and eventually stop. How far it travels depends on the acceleration energy and the stopping power of the accelerated species in the target material. Ions will stop at different locations since the scattering is relatively random, but the average depth into the material they end up at is called the *projected range*, R_p. As seen from Fig. 3.2, this is quite different from the ions path length in the material. Using R_p, the impurity concentration, N(x), at a distance x into the material can be described, to a first approximation, by a Gaussian on the form

$$N(x) = \frac{\phi}{\sqrt{2\pi}\Delta R_p} e^{-(x-R_p)^2/2\Delta R_p^2}. \tag{3.2}$$

Here ΔR_p is the standard deviation (straggling) of the projected range and ϕ is the dose, i.e. the number of ions implanted per cm^{-2}. The equation is normalized so that an integral from x=0 to ∞ equals the dose.

The stopping power can be decomposed in two, an electronic, S_e, and a nuclear, S_n, contribution. Both depend on the charge number and mass of both the incoming ions and target material, but they differ in what energies they dominate the stopping. The scattering mechanism are different, an electron has a weight about five orders of magnitude lower than a nucleus, which means that a single scattering event with an electron will not alter the momentum of the ion significantly. Hundreds of thousand of these collisions happen during an implant, which makes a continuum mechanism a good approximation. This makes

$$S_e \propto \sqrt{E}, \tag{3.3}$$

where E is the ion energy, thus the electronic stopping power increases with ion velocity. This approximation is valid up to very high energies, often above what is used for normal implantations, where it breaks down, and the stopping power is reduced with energy. The nuclear stopping power is a more complex function. It can be treated as screened coulomb scattering events, and the energy loss depends on the impact parameter (says something about how close the incoming ion and target atom would come to each other if no scattering were to occur). A smaller impact parameter gives a larger loss (the c) beam in Fig. 3.3). In addition the mass ratio between the incoming ion and target atom plays a big role, the smaller ratio, the larger energy loss. At low ion energies, the collision between incoming ions and target atoms will be elastic, because of bonds in the target not being broken by the incoming ion. So the stopping power increases at low energies. As the energy is increased it will reach a

maximum, and start to decrease. This is due to higher velocities in the incoming ions, which make the collision time shorter, and the target atom will not be able to change the ion velocity as much.

What makes ion implantation so useful and broadly used is the reproducibility and that projected range and depth profiles are easily calculated using numeric calculations in programs like SRIM by Ziegler [65]. A drawback, for some applications, is the damage following an implantation. The highly energetic incoming ions collide with the lattice atoms in the target, and the energy transfer is usually high enough to break bonds, making vacancies and interstitials, as well as possible extended defects. High energy and dose implantations can render a lattice amorphous at the depth where the most energetic collisions take place. To mend the damage acquired during implantation subsequent annealing of the material is often required.

3.2.1 Channeling

When an incident ions direction is parallel to a major crystal orientation, it could be able to penetrate deep into the crystal, due to the reduced stopping power in the channel. This phenomena is called *channeling*. Figure 3.3 shows three different incoming ion trajectories. Here b) is the channeling ion, traveling a larger distance into the material. In c) the incoming ion travels parallel to b) but hits too close to the target atoms, and are deflected. The last trajectory, a), has an incident angle compared to the major crystal direction, not able to enter a channel, and is scattered at a shallower depth than the two other ions. The consequence of

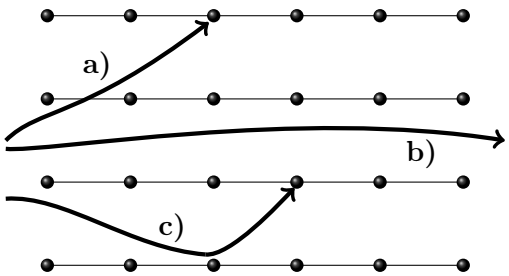

Figure 3.3: Three different incident paths of incoming ions. a) Skewed incident angle, no channeling occurs. b) Incident velocity parallel to a major crystal direction, and channeling occurs. c) Parallel with b), but is too close to the channel edge (small impact parameter) , and is deflected with a too big angle to channel.

channeling when implanting is that ions will penetrate deeper into the sample and create a tail in the Gaussian impurity concentration as a function of depth (equation 3.2). This effect can be very pronounced for light atoms implanted into heavy matrices, but can be seen for heavier implants as well.

When the ion beam is tilted above a critical angle to a major crystal direction, the tail in concentration is removed, and the amount of channeling strongly reduced. The critical angle can be calculated, and depends on incident ion energy, atomic species in the ion beam and target, as well as the atomic spacing along the major crystal direction. In Si a typical tilt angle to avoid it is about 7°.

3.3 Secondary Ion Mass Spectrometry

This section is based on the reference by Heide [66].

In secondary ion mass spectrometry (SIMS) ions bombard a surface, transferring enough energy to the surface atoms for them to escape the surface. Some of these atoms will be ionized in the process, and by analyzing these through mass spectroscopy atomic concentrations as a function of depth can be measured.

3.3.1 Principles

A schematic of the SIMS principle is shown in Fig. 3.4. Incident primary ions from an ion source sputter the surface of a sample, resulting in scattering of its particles. Some of these ions can be ionized in the scattering process, making it possible to extract them through an energy analyzer and a mass spectrometer using electric fields. Thus, it is a destructive technique, damaging the sample while information is gathered about the composition. Mass spectra can be extracted, using the magnetic mass spectrometer, monitoring all the different secondary ionic species emerging from the sample as the primary ion beam sputters into the sample. Depth profiles of desired elements can be measured by only allowing secondary ions of these to pass trough the mass spectrometer, and monitor how the current changes with sputtered depth into the sample. Lastly, images of surface composition as a function of position in samples can be obtained by scanning the primary ion beam over a surface, and measuring current changes in the selected secondary ion signal. To measure unknown concentrations, a reference sample, with a known impurity concentration should be measured as well, to convert SIMS intensity in counts/s to absolute concentration in atom/cm^3, giving quantitative analysis of a chosen impurity. To calibrate the depth profile of a unknown element, the sputtering time is measured. Then, by measuring the crater depth, using e.g. stylus profilometry, the depth profile can be converted from seconds to length. Often done by assuming constant erosion rate.

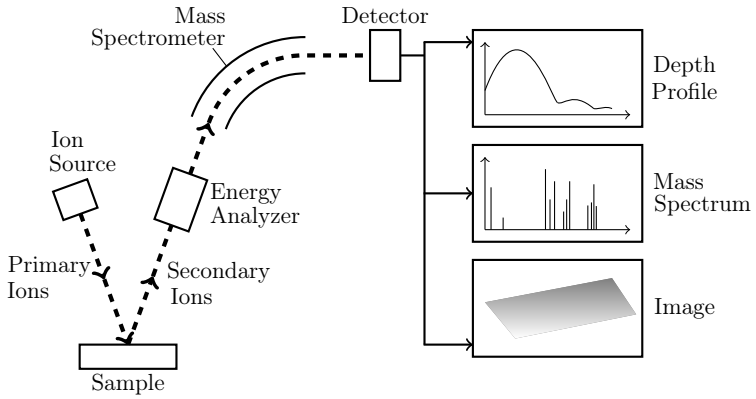

Figure 3.4: Schematic of the SIMS aperture.

The secondary ionization process depends strongly on the sputtered ions environment, as well as the primary ion beam. Positive ionizations can be enhanced by using an electronegative primary ion, like oxygen, while negative ionizations favor electropositive ions, like cesium. Usually a SIMS instrument would be equipped with both, as different samples could favor different primary ions.

3.3.2 Interpreting SIMS Measurements

SIMS has a some challenges when it comes to interpreting the secondary ion signal, which can obscure the analysis of gathered data. There is crater edge effects, memory effects, mass interference, profile broadening effects from ion bombardment, surface roughness, and matrix effects.

Crater edge and memory effects arise when not only species are collected from the crater bottom. In the edge effects atoms from the crater walls are collected by the mass spectrometer. This is especially important when sputtering deep craters, when the beam could drift, and if there is misalignments in the system. Apertures where the mass spectrometer entrance is close to the sample is particularly exposed to this effect.

Mass interference happens when there is more than one species in the sample with about the same m/q (mass/charge) ratio. As a consequence the measured signal is a sum of several species. This is especially a problem for heavier species, where there are more combinations of complexes at given masses. How good the atomic weight resolution is depends on the mass spectrometer, increased resolution will prevent over counting of elements, though the problem can usually be solved by using a voltage offset. Taking advantage of the narrower energy distribution of heavier particles, their signal can be almost completely wiped out.

Primary ions can cause recoil implantation as well as cascade mixing, which will broaden the concentration to depth profile, by analyzing particles that usually do not belong at the given depth. The solution to this is a reduction in the primary ion energy, reducing the collision energy, or alternatively reduce the angle of incidence.

Surface roughness in the crater will reduce the depth resolution in SIMS. This can emerge during sputtering because of crystals lying in different directions with varied sputtering velocities depending on the orientation, or because of a surface roughness in the sample to begin with.

Lastly matrix effects can make multilayer depth profiling complicated. Often when sputtering through one layer and into another the secondary ionization efficiency of a given species will change drastically. This effect can have two explanations, either it is a change in sputtering yield from one matrix to the other, or more common a great change in ionization probabilities for the two matrices. This effect is especially relevant in search for different phases, like NCs, giving a change in measured signal if there is a new phase present.

3.4 X-ray Diffraction

This section is based on the references by Birkholz [67] and Sardela [68].

X-ray diffraction (XRD) is a powerful tool to gather structural information about a material. By utilizing elastic x-ray scattering, properties like crystal structure, crystalline quality, inter planar distances and more become available through a relatively easy and fast experiment.

3.4.1 Working principles

The basic theory of diffraction was established in section 2.1.1, and the experimental equipment is designed to utilize this. A general schematic of the set-up can be seen in Fig. 3.5. An X-ray source produce X-rays that are directed towards the sample, and refracted into the detector. Often a monochromator is situated in between the sample and detector to make sure only

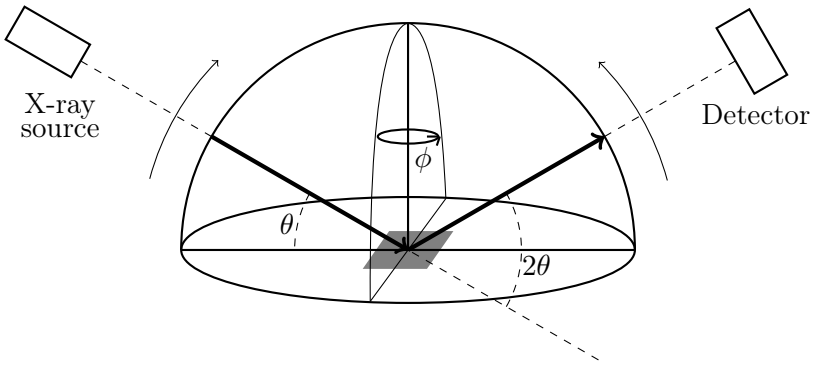

Figure 3.5: A schematic of the XRD experimental equipment.

waves of a given wavelength pass through. A common radiation used is the Cu Kα, with a wavelength of 0.154 nm. There are several different modes in which XRD can give structural information about the sample, but in this thesis the most important one is the $\theta/2\theta$-scan, supported by a ϕ-scan.

$\theta/2\theta$-scan

In the $\theta/2\theta$-scan the intensity of diffracted X-rays are measured as a function of the 2θ angle seen in Fig. 3.5, ie. the angle between the incoming and diffracted wave. This is done by moving the X-ray source, the detector, or both in a circular fashion, depending on the experimental set up. Planes with given Miller-indices will fulfill the Bragg-condition (eq. 2.8) at different 2θ-values, making the result, a diffractogram, a "fingerprint" of the measured material. Materials with different lattice constants and crystal structures will of course give different results. For materials containing more than one phase the diffractogram will contain all present phase peaks, making it possible to e.g. detect foreign phases, in a material. To be detected these have to be big enough for diffraction to occur in a measurable manner. Meaning that the positive interference between waves has to large enough to be detected.

In addition the $\theta/2\theta$-scan can give indications of the crystalline quality of a material. This is done by comparing the full width at half maximum (FWHM) values and the intensity of the same peaks (e.g. the (002) miller indexed plane) in different diffractograms. If the material quality is poor the peak will be wide and thus have a large FWHM-value, while if it is good the peak will be tall and slim with a low FWHM-value.

ϕ-scan

A ϕ-scan is a scan where the X-ray source and detector is locked at a given 2θ-value, while the stage is rotated around the sample surface normal vector (Fig. 3.5). When doing thin film or bulk XRD, the only diffracting reflexes are the ones perpendicular to the surface, i.e. only the preferred growth direction of the film or bulk substrate. This means that for a ZnO film with a surface normal perpendicular to the (0002) plane, other peaks like (1100) would not be visible.

3.5 Rutherford Backscattering Spectrometry

This section is based on the references by Morgan [64] and H. Bakhru [69].

Rutherford backscattering spectrometry (RBS) is a way of analyzing materials in a non destructive way. It uses backscattering of incident ions in the MeV range to detect anomalies in the targets crystal structure. Through the measurement of these backscattered ions energy, it is possible to measure the depth of where these scattering events take place. It is thus very suited for detection of impurities and structural variations as a function of depth. Of course an ion beam has a limited range into the crystal, which limits the analysis in terms of measurement at a large sample depths. Measurements in combination with channeling can give a lot of information about defects and crystal structure.

3.5.1 Principles of RBS

An ion penetrating through a target material, will lose energy to electrons through collisions and excitations, in addition to energy lost in nuclear collisions. Depending on how the incident ion hits nuclei, its trajectory will change. If it is scattered in the reverse direction, it is called backscattering. After such an event, the ion will again lose energy to electrons on its way out of the target material, and when emerged it can be collected. The nucleus collision can be treated as a two-body kinetics problem, and the electron collisions provide information about depth of the penetration. This is the basics of Rutherford Backscattering spectrometry. A schematic of the experimental setup can be seen in Fig. 3.6.

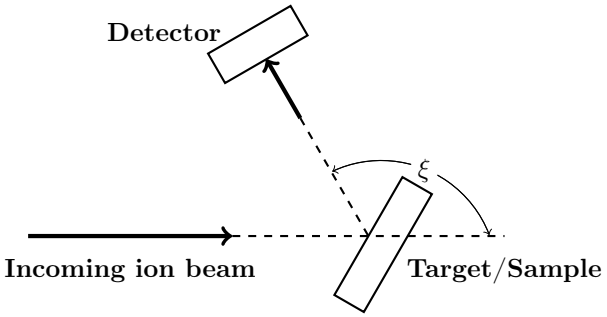

Figure 3.6: A schematic of an RBS setup.

The ion beam normally consists of either hydrogen or helium ions. Helium ions will give better depth resolution, while hydrogen will not as easily be dechanneled by small amounts of disorder. Thus the given material and its parameters will decide what is the most suited ion beam. A thin film, with disorder, would not suffer from a lot of dechanneling, since the signal would be high anyway. But for a thicker layer a hydrogen beam could be better. Usual ion energies is 0.1–1 MeV for hydrogen beams and 1–4 MeV for helium. While higher ion energies will reduce dechanneling, too high could lead to undesired reactions in the target. Helium beams are most widespread, since it is easily accomplished in a small accelerator and its properties are widely documented, in addition to being a inert species.

There are three main mechanisms within the backscattering that provide information about the target. Firstly there is the kinematic factor, defined as

$$\frac{E_1}{E_0} = K = \left[\frac{(M_2^2 - M_1^2 \sin^2 \xi)^{1/2} + M_1 \cos \xi}{M_2 + M_1} \right]^2 . \tag{3.4}$$

Where E_0 is the incoming ion energy, E_1 is the energy measured from the backscattered ion, ξ is the angle between the incoming and backscattered ion beams, and M_1 and M_2 the mass of incoming ions and target atoms, respectively. In an ordinary RBS measurement E_0, M_1 and ξ will be part of the experimental setup, and thereby known, while E_1 is measured. This makes it possible to calculate the backscattering target atoms mass, M_2. The second is the depth profile, gained by looking at the energy an incident ion loses to collision and excitation of electrons on its way in and out of the target material. It can be written as

$$\Delta E = [S]t \tag{3.5}$$

where $[S]$ is called the backscattering energy loss factor and t is the depth. $[S]$ changes slowly with thickness and energy, and is dependent on the kinematic factor as well as the stopping power, S_e and S_n, of the target material. I.e. there is a direct correlation between the width of a signal peak, and the width of a given layer ΔE. Thirdly it is possible to se differences in intensity depending on the scattering cross section of the target atoms. E.g. with a ZnO target, the Zn peak would be more intense than the O peak, since Zn is a heavier atom with a larger cross section, as well as larger mass, and thus a higher probability of backscattering an incoming ion.

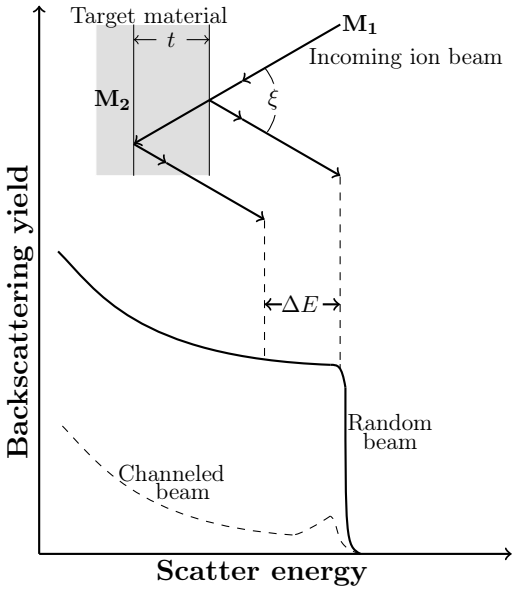

Figure 3.7: A Rutherford backscattering yield, including a schematic of scattering processes in the material.

There are some drawbacks to the RBS technique. Ion beams have a finite range into the material, making analysis deeper than a few μm hard. The lower limit of technique sensitivity is often referred to as 0.1 atom% of displaced atoms. And while it is easy to distinguish heavy atoms in light substrates, the opposite, light atoms in a heavy substrate, proves difficult. In addition, two heavy atoms, usually over 40 amu, can be difficult to distinguish in a spectra. Often complementary techniques like SIMS and XRD (both explained in previous sections) are used in addition to RBS for better understanding of the material.

3.5.2 RBS Application

Semiconductors are very sensitive to composition, making RBS a good characterizing tool. It is fast, non destructive and can give a lot of information about impurities and defects. A good example is studies on dopants and implantation damage in materials. The RBS yield will depend on the number of dopants in displaced positions. Heat treatment can make these impurities diffuse to substitutional sites, and by comparing the two, mapping of the needed annealing temperature can be done. The same is true for extended defects. This is important factors in semiconductors. To increase carrier concentrations, the dopants often has to be in substitutional positions. Defects on the other hand, especially radiation induced ones like vacancies and interstitials, can reduce carrier concentrations.

This is done by comparing a random, where there is no channeling, and a channeling incident beam. In the bottom part of Fig. 3.7 a schematic of both yields can be seen. The channeling beam has a lower intensity, which is due to that an ion is less likely to be backscattered once it has entered a channel. The more defects there is in the material, the closer the two lines will be, i.e. there would be little difference between the lines in an amorphous solid. For an ion implanted sample, a top in yield would be expected around the R_p, due to scattering from interstitial impurity atoms. In addition an increase can be seen at lower scatter energies. This is mostly due to scattering from extended defects and dechanneling because of defects at a shallower depths, leading to backscattering deeper into the material.

3.6 Transmission Electron Microscopy

This section is based on the references by Egerton [70] and Brandon [71].

The small wavelength accelerated electrons can reach makes electron microscopy able to magnify to a greater extent, and thus produce more detailed pictures. A very popular technique utilizing this is *transmission electron microscopy* (TEM). Electrons are accelerated at high voltages, typically 100-400kV, focused using electromagnetic lenses, and sent through the sample. The transmitted electrons are detected by a phosphorous screen or a CCD camera, making it possible to see both images and diffraction patterns from the sample (Fig. 3.8). Changes in aperture makes it possible to change between diffraction- and image-mode easily.

There are three types of contrast making it possible to see images in the TEM: *Mass-density-*, *diffraction-*, and *phase contrast*. When electrons travel through a solid, the atomic nucleus will scatter the much lighter electrons from their path, while they remain still. The amount of electron scattering in a given point then depends on the mass-density (product of density and thickness) in that point. Thus giving thicker and denser areas more scattering, causing variations in the resulting picture. Diffraction contrast is a similar and the main contrast source in crystalline TEM samples. Incident electrons can be diffracted in accordance with Bragg's law if the sample is tilted in the right direction. Usually the diffracted electrons do not get through apertures, and the image contrast appears. This type of contrast is very sensitive to sample tilting, as opposed to the mass-density contrast. Lastly phase contrast can be used. This is more complex, it produces the highest quality images for crystalline materials, and is thus often called *high resolution transmission electron microscopy* (HRTEM). It utilizes two electron waves with different phase, like a diffracted and a transmitted wave. It will result in a interference pattern between the two waves, showing the periodicity of the crystal.

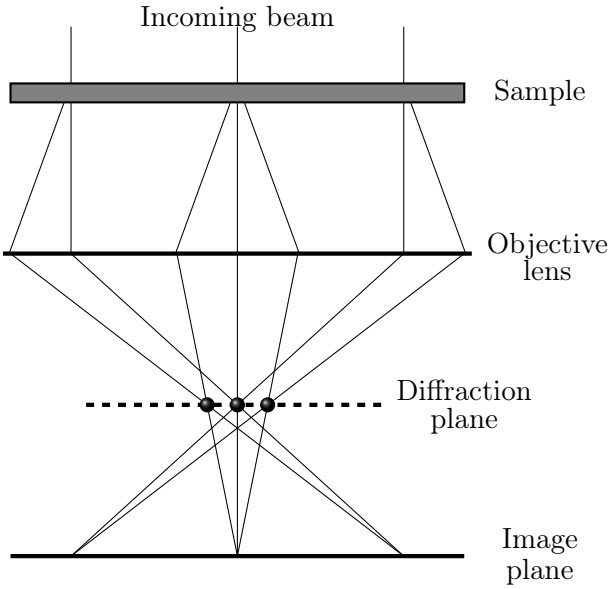

Figure 3.8: Schematic of the TEM beam after it has been transmitted through the surface. Part of the transmitted beam is diffracted, some is scattered, and some is transmitted right through the surface.

Imagery like this usually use elastically scattered electrons to form an image. A technique that uses the inelastic scattered electrons is *electron energy-loss spectrometry* (EELS).

A downside to the TEM technique is that the sample preparation required beforehand is complex. Here the sample has to be thinned down using a grinder or another tool, and can be quite challenging and time consuming.

3.7 Scanning Electron Microscopy

This section is based on the reference by Leng [72].

The *scanning electron microscopy* (SEM) is a widely used technique, with clear resemblances to the TEM. One primary difference is that the SEM setup relies on a backscattering of electrons, instead of transmission. In addition the electron beam is focused and scanned over the surface, putting it together to create an image of the surface of the material. One of the favorable things about the SEM is the great depth of field, even at high magnifications.

The acceleration voltage of the electron beam is about an order of magnitude below the TEM, with ∼10-40 kV. Electromagnetic lenses are used to focus the beam, and to raster it over the surface. Two types of electronic signals are used to create an image, *secondary-* (SE), and *backscattered electrons* (BSE). The latter is a result of elastic scattering by nucleus in the target material, and the former is a inelastic scattering event where the incident electron collides with electrons in the target material and produce SE with substantially lower energy than the incoming electrons. BSE gives a compositional contrast, as heavier atoms elastically scatter electrons with greater ease, while SE gives information about the sample topography.

3.8 Hall measurements

This section is based on the references by Streetman [9], Blood and Orton [73], van der Pauw [74], Hemenger [75], and Roro et al. [76].

3.8.1 The Hall Effect

An effective way to measure carrier concentration is using the Hall effect. This method takes advantage of the force acting on a charged particle when it moves in a magnetic field. Using vector notation, the relationship follows

$$\mathbf{F} = q(\mathbf{E} + \mathbf{v} \times \mathbf{B}), \tag{3.6}$$

where $\mathbf{F}$ is the force, q the electron charge, $\mathbf{E}$ the electrical field, $\mathbf{v}$ the velocity, and $\mathbf{B}$ the applied magnetic field. For an electron in a n-type semiconductor, shown in Fig. 3.9 with a current going from A to B (I_x), the force working in the y-direction is expressed as

$$F_y = -q(E_y - v_x B_z). \tag{3.7}$$

With no voltage applied between points C and D, the electrons will experience a force in the

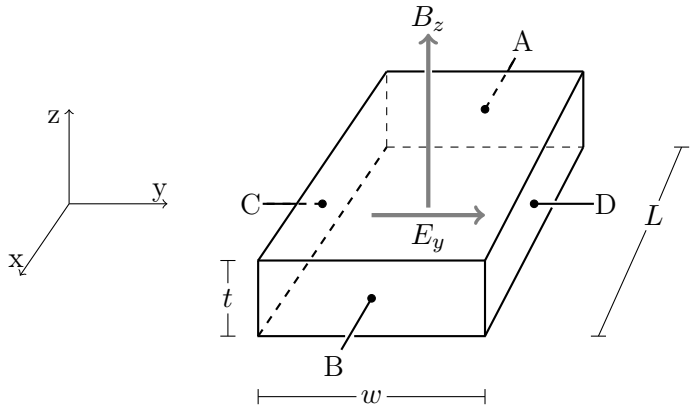

Figure 3.9: Figure describing the Hall effect.

-y direction. For electrons to keep a steady flow from A to B, F_y has to be zero, which is fulfilled when there is an electric field of magnitude

$$E_y = v_x B_z. \tag{3.8}$$

This electric field will be set up as the applied magnetic field shifts the electron distribution in the y-direction. This is called the *Hall effect*, and it applies a voltage $V_{CD} = E_y w$ called the *Hall voltage*, V_H. Using that $v_x = J_x/qn_0$, equation 3.8 can be written

$$E_y = \frac{J_x}{qn_0} B_z = R_H J_x B_z, \quad R_H = (qn_0)^{-1}, \tag{3.9}$$

where R_H is called the *Hall coefficient*. Using this it is possible to make an expression for the charge carrier concentration utilizing measurable quantities

$$n_0 = \frac{1}{qR_H} = \frac{J_x B_z}{qE_y} = \frac{(I_x/wt)B_z}{q(V_{CD}/w)} = \frac{I_x B_z}{qtV_{CD}}. \tag{3.10}$$

By measuring resistance, and using that the conductivity of electrons follows $\sigma = q\mu_n n_0$, the resistivity and mobility can be calculated using the following expressions

$$\rho(\Omega - cm) = \frac{V_{AB}/I_x}{L/wt}, \quad \mu_n = \frac{R_H}{\rho}. \tag{3.11}$$

3.8.2 The van der Pauw Method

A way to utilize the theory above is to use the van der Pauw method. It is a technique designed to measure the resistivity, mobility and carrier concentration in a sample of any given shape, as long as the following conditions are fulfilled:

- The contacts are at the edge of the sample.
- The contacts are small in area.
- The sample is of homogeneous thickness.
- The sample does not contain isolated holes.

Examples of how the experimental setup looks can be seen in Fig. 3.10. There are four contacts made on the sample, current is run through two of them, and the resulting voltage loss is measured over the two others. If the resistance calculated using the current and voltage

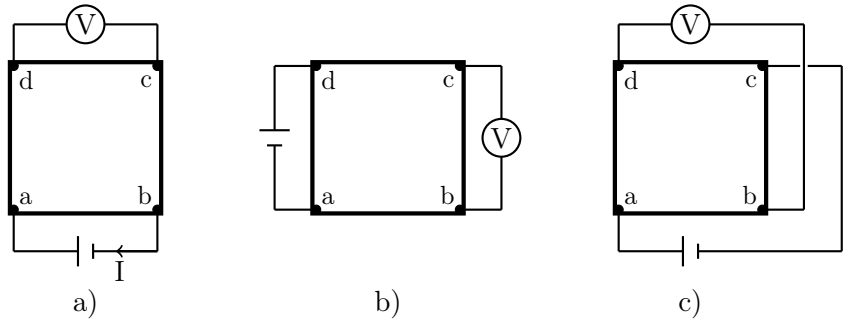

Figure 3.10: Simple schematic of possible sample connections using the van der Pauw method.

loss in Fig. 3.10a) and b), henceforth called R_a and R_b, respectively, the samples resistivity can be measured using

$$\rho = \frac{\pi t}{\ln 2} \frac{(R_a + R_b)}{2} f\left(\frac{R_a}{R_b}\right). \tag{3.12}$$

Here f is a function that decreases with increasing R_a/R_b ratio, and equal to unity for $R_a = R_b$. By taking an average of R_a and R_b using measurements with the same setup, but switching the voltmeter and current source positions, as well as reversing the current in both configurations, will yield more representative result.

Then, by using the setup in Fig. 3.10c), with a magnetic field applied perpendicular to the sample surface, the *Hall voltage*, V_H, can be measured. From this the mobility and carrier concentration can be calculated using theory from section 3.8. By reversing the field and varying the terminal positions a larger ensemble of measurements, and thus a more representative result, can be obtained.

3.8.3 Temperature dependent Hall measurements

Temperature dependent Hall (TDH) measurements utilize the van der Pauw method, but measure the quantities mentioned above as a function of sample temperature. Using the carrier concentration plotted against temperature, it is possible to see the rate at which carriers freeze out, and by that calculate impurity levels in the semiconductor band gap. The general theory this builds on is described earlier in section 2.2.1. It is done by using an a bit modified version of the space charge neutrality (eq. (2.32)),

$$n + n_d = N_d - N_a \tag{3.13}$$

together with

$$n = N_e^{-(E_c - E_F)/kT} \tag{3.14}$$

and

$$n_d = N_d \left[\frac{1}{1 + \beta e^{-(E_d - E_F)/kT}} \right]. \tag{3.15}$$

Here n_d is the density of electrons on donor atoms, E_d the donor energy in the band gap, β a factor of degeneracy for the donor level (usually $1/2$ for simple donors), E_c the conduction band bottom energy, and N_c the effective density of states in the conduction band, often written as $N_c = 2(2\pi m^* kT/h^2)^{3/2}$, where m^* is the electron effective mass. This amounts to

$$n^2 + n(N_a + N_c') - (N_d - N_a)N_c' = 0 \tag{3.16}$$

when solved for n, where

$$N_c' = \beta N_c e^{-(E_c - E_d)/kT}. \tag{3.17}$$

By fitting the measured TdH data with this, parameters like N_d, N_a, and $E_c - E_d$ can be found.

3.9 Scanning Spreading Resistance Microscopy

This section is based on the reference by Eyben [77].

Scanning spreading resistance microscopy (SSRM) is based on the atomic force microscope (AFM), but upgraded with a conductive cantilever, and an applied bias between this and the back side of the sample. The experimental setup can be seen in Fig. 3.11. An AFM can work in more than one setting, but a common one is contact mode. Here the cantilever-probe is scanned over the sample, as it meets irregularities the cantilever is deflected, deflecting the laser light, registering the irregularity at the detector.

Using the conductive cantilever and a back contact the SSRM makes it possible to measure the spreading resistance in small points all over the sample, by applying a voltage between the front and back side of the sample. By measuring the current in each point, a resistance map can be calculated for the measured areas. This is especially useful for layered materials, and heavily doped areas, showing the differences in resistance across the sample. Usually the measurements are done on a cleaved edge of the sample surface.

3.10 Optical Transmission Spectroscopy

This section is based on the references by Streetman [9], and Soares [78].

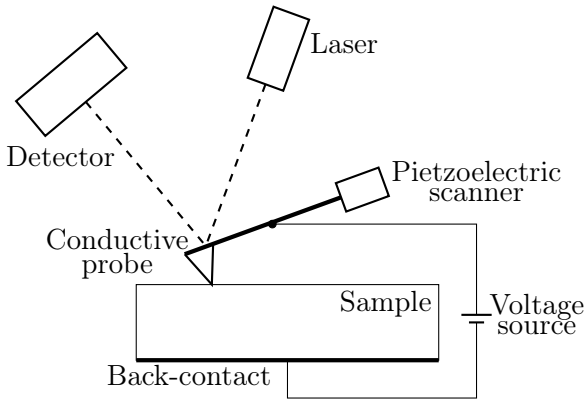

Figure 3.11: A schematic of the SSRM experimental setup.

3.10.1 Optical Absorption

Irradiating a sample with photons is a good (contact less) way to gather information about the electrical properties of the material. Absorption measurements are the easiest way to do this, and is often referred to as *optical absorption*, though the absorbed photons are not exclusively in the visible range[1]. The experimental aperture needed is what makes this measurement simpler than e.g. photoluminescence. A monochromator transmits photons to the sample, and a detector measure what comes out on the other side. By adjusting the incident photon wavelength a plot of the absorption coefficient α can be made as a function of photon energy, in accordance with the *Beer-Lambert law*

$$I_t = I_0 e^{-\alpha t}, \tag{3.18}$$

where I_t is the transmitted light intensity through a sample of thickness t, with an incident intensity of I_0. Alternatively the transmittance, in percentages of the incident intensity, could be plotted as a function of the photon energy. Because semiconductors will absorb very little of the incoming radiation with lower energy than the band gap, E_g, of the material, this plot gives information about the band gap of the material, and band gaps of possible secondary phases in the material. In addition it can be possible to detect large carrier concentrations in the material.

3.10.2 Experimental setup

Transmittance measurements are often done using a spectrophotometer in transmittance mode, seen in Fig. 3.12. Here light from the source goes through a monochromator and is split into two beams, one beam that goes through the sample and one reference beam. Both beams enter a detector, and the transmittance (T) of the sample is easily calculated from the measured power of the reference beam (P_0) using

$$T = \frac{P_T}{P_0} \times 100, \tag{3.19}$$

where P_T is the power of the light passing through the sample.

[1]Most semiconductors have band gaps in the optical range, but infrared as well as UV radiation is widely used.

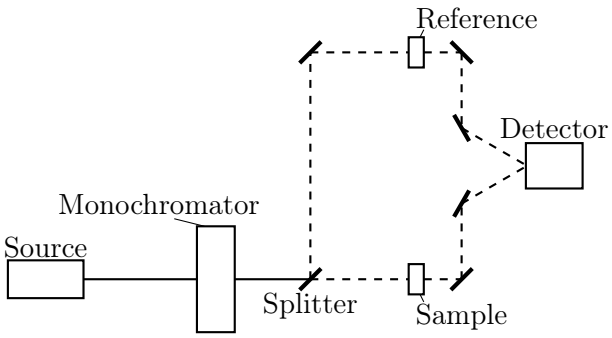

Figure 3.12: Schematic of a spectrophotometer in transmission mode.

3.11 Photoluminescence Spectroscopy

This section is based on the references by Streetman [9], Gilliand [79], and Pettinari et al. [80].

3.11.1 Photoluminescence

Another useful technique for electrical characterization is photoluminescence (PL). It too relies on excitation of a material by absorption of photons, but the measured quantity is the luminescence created from radiative recombination of excited charge carriers in the material. Defect levels, and any other energy levels in the band gap of the material will emit radiation unique to their energy upon radiative recombination. Some transitions of this kind can be seen in Fig. 3.13. This can include transitions like the donor-to-valence band and conduction

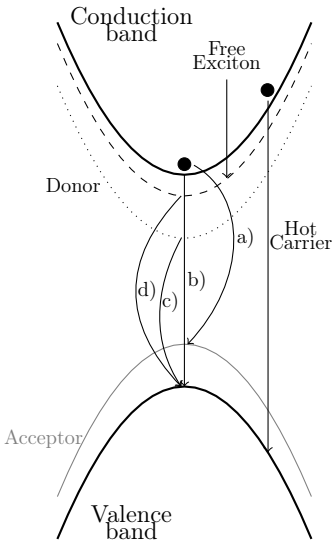

Figure 3.13: Examples of different transitions visible in a PL measurement. **a)** goes from the conduction band to an acceptor level, **b)** is a band to band transition, **c)** is from a donor level to the valence band, and **d)** is from a free exciton level to the valence band.

band-to-acceptor level, which usually leads to emissions below the band gap energy. Excitonic recombination like this is likely to give narrow emission bands, making them useful for identifying species/defects present in the sample.

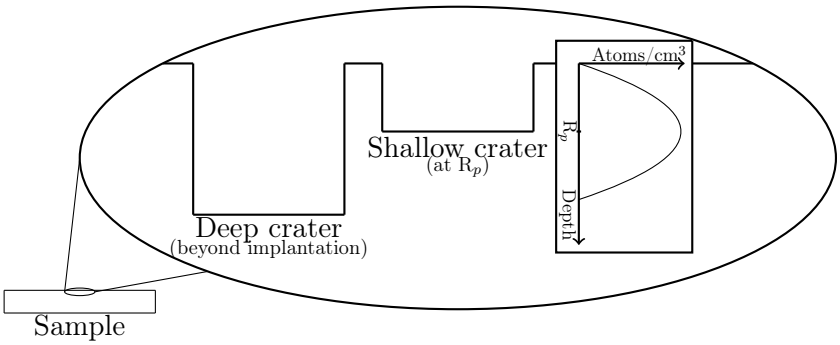

Figure 3.14: A schematic illustrating a sample with sputtered craters for PL analysis. A implantation profile inset of the sample is included, illustrating that the shallow crater is at R_p and the deep crater is beyond the implanted area.

For layered samples and samples with implantation profiles too deep to effectively collect luminescence from the surface, PL measurements of desired areas can prove challenging. A possible solution, utilized in this thesis, is to sputter craters down to the selected sample depth, using SIMS or other sputter technique, and thus be able to selectively collect data from chosen depths in the sample. More precisely for implanted samples this would enable probing at R_p, and beyond. By sputtering one crater to R_p-depth, and another to beyond-implantation-profile-depth, the emission from the implanted layer can effectively be compared to bulk emission, and thus help interpretation of the result as well. Both examples are illustrated in Fig. 3.14, showing the surface of the sample including craters and an implantation profile as a reference to the depth of these. When using this technique the crater width has to be larger than the PL light probe. If that is not the case, the result will be a mixture of crater and surface emission.

3.11.2 Experimental setup

The experimental setup can be seen in Fig. 3.15. A laser produces monochromatic radiation which is deflected using mirrors on to the sample surface. Often an electromagnetic lens is used to focus the laser, to make the probing area smaller. Because of the short absorption length for light of higher-than-band-gap energy, the PL measurement is in a backscattering configuration. The emitted light is focused into a detector by another lens. The sample is often cooled, using a cryostat. For low temperature measurements there are fewer carriers, giving a lower recombination rate, but there is little thermal smearing (phonon coupling) from charge carriers thermally excited following the Fermi-Dirac statistics, giving narrower emission peaks.

Normally in a PL experiment the excitation energy of the laser radiation is kept fixed, while the detection energy is varied. Because of short relaxation times for electrons excited higher than band edges, through non radiative emissions like phonons, compared to radiative recombinations, practically all electrons will be at the minimum excited energy when the radiative recombination take place. The measured intensity is plotted as a function of emitted photon wavelength or energy.

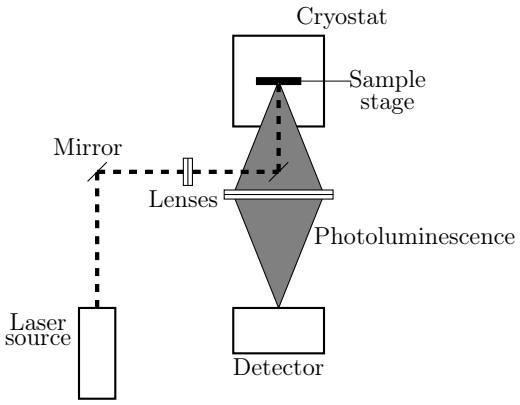

Figure 3.15: A schematic of the PL setup.

3.12 Experimental Information

In this study, there is two main sample groups, Si implanted ZnO and Ge implanted ZnO, as well as one additional Zn implanted ZnO series, meant as control samples for comparison.

3.12.1 Equipment

Ion Implantations were done with a 1MV NEC tandem ion accelerator, and conducted by Victor Bobal. The energies used varied for the different ions to get the wanted depth in each case. Calculations of the projected range of the implantations were done using the SRIM software package by Ziegler et al. [65].

Sputtering of the ZnO thin film were done using a Semicore TriAxis magnetron sputtering device, and was conducted by Heine Nygard Riise. The deposition were done in Ar sputter gas at 400°C, with a ZnO target and a forward power of 25 W, the chamber pressure was 7.0 mtrorr, and the sputter time was 365 minutes.

Laser Cutting were executed using a Rofin laser cutter at 50 kHz, 32 A, speed of 400 mm/s and an execution count of 300 scribes.

SIMS measurements were done using Cameca IMS7f microanalyzer. A beam of 10 keV O_2^+ was rastered over the surface, usually over a area of 125×125 μm^2. Crater depths was measured using a Dektak 8 stylus profilometer, and constant erosion rate was assumed when the sputtering time was converted to depth. Calibration of the Ge and Si signal was preformed using the implanted concentration as reference. Done in collaboration with Lasse Vines and Alexander Azarov.

XRD utilized a Bruker AXS D8 Discover system with a K_α X-ray source. Using a asym. Ge 220 2-bounce monochromator to filter out the $K_{\alpha 2}$ radiation, leaving only the $K_{\alpha 1} = 1.54444$ Å wavelength.

RBS measurements using the same 1MV NEC tandem ion accelerator used during implant of guest species with He-ions of energy 1.62 MeV incident in the [0001] direction, and a detector angle of 165 degrees. Measurements were conducted by Alexander Azarov.

Hall Effect Measurements were done using a LakeShore 7604 system, with a temperature range of 10-350 K.

PL Utilized a cw 325nm HeCd laser (7mW) as excitation source. Luminescence was collected by a long working distance microscope and directed both to imaging spectrograph (HORIBA

Jobin Yvon, iHR320) with two exit ports coupled to EMCCD camera (Andor DL-658M) and photon counting PMT (Becker&Hickl, PMC100) and also to fiberoptic spectrometers (Ocean Optics, HR4000 and USB4000 with 0.2/2nm spectral resolutions, respectively). Measurements were conducted by Augustinas Galeckas.

SSRM utilized a Bruker Dimension 3100 SPM instrument, with NANOSENSORS™CDT-NCHR probes [81]. All samples utilized voltage was 4 V and was measured directly on the cleaved edge, except T1Si-1000C, which was polished beforehand and measured at 500 mV. All measurements were conducted by Jon Borgersen.

SEM measurements utilized a Hitachi SU8230 Ultra High Resolution Cold FE-SEM, with acceleration voltages between 5-15 kV. Done in collaboration with Torunn Kjeldstad.

TEM were mainly conducted on a FEI - Titan G2 60 - 300 kV. Imaging were done with a acceleration voltage of 300 kV, and was conducted by Phuong Dan Nguyen. EELS measurements were done at 60 kV and was conducted by Cecilie Granerød. Additionally a Jeol JEM-2100F TEM, with a acceleration voltage of 200 kV were used for lower magnification STEM imaging, conducted by Phuong Dan Nguyen.

Transmission Measurements used a Shimadzu SolidSpec-3700 DUV, utilizing an integrating sphere for measurements. With available wavelengths from 175-2600 nm and a resolution of 0.1 nm. Measurements were done in collaboration with Kristin Bergum.

3.12.2 Bulk samples

The bulk samples utilized are commercially available ZnO from Tokyo Denpa of different resistivity grown hydrothermally. The wafers are cut perpendicular to the c-axis and originally mainly of $10 \times 10 \times 0.5$ mm^3 in size. Some wafers were cut into smaller pieces using a diamond diamond pen to help cleave the surfaces, while others were cut using a laser cutter. All samples were implanted on the Zn-face of the wafer. High resistive samples are highly compensated by a large Li concentration. Low resistive samples have a significantly smaller concentration, due to heat treatment at 1300°C for 4 hours at Tokyo Denpa.

3.12.3 Experimental procedure

3.12.3.1 Si implanted ZnO

Two temperature series were done with Si implanted ZnO Tokyo Denpa wafers. The first was an initial test of the material combination, called T1Si. A $10 \times 10 \times 0.5$ mm^3 wafer with a resistivity >1 kΩ-cm (high resistive) was implanted with a dose of 10^{16} cm^{-2} Si ions at a energy of 375 keV, giving a concentration $\sim 10^{20}$ cm^{-3} at a projected range of $\sim$ 325 nm. Further it was cut in four equal pieces of 5×5 mm^2. Then three of the pieces were heat threated for an hour, one at 600°C, one at 800°C, and the third at 1000°C, while the fourth was kept as implanted. Each of them were named T2Si-600C, -800C, -1000C, and -asimp, respectively. RBS, SIMS, XRD, Hall effect, and SSRM measurements were then used for characterization.

The study was repeated with a second series of Si implanted samples, called T2Si, targeting annealing temperatures in the 500-800°C range, to reproduce and further examine the T1Si series. A 10×10 mm^2 Tokyo Denpa wafer with a resistivity of ∼0.18 Ω-cm (low resistive) was cut using laser into four 5×5 mm^2 pieces. It was implanted using the same energy and dose (375 keV and 10^{16} cm^{-2}, respectively). One was annealed for an hour at 500°C, another at 600°C and the third at 700°C, with the fourth kept as implanted. They were then

characterized using XRD, RBS, and SIMS, before the 500°C and 600°C were annealed at 750°C and 800°C, respectively, for an hour. These two where then characterized again using RBS, XRD, TDH, and SIMS. In addition the as-implanted sample was heated at an hour at 600C to do TDH-measurements at this temperature as well.

Lastly a 10×5 mm^2 ZnO wafer with a resistivity equal to 0.10 Ω-cm was implanted with a Zn dose of 10^{16} cm^{-2} with an ion energy of 800 keV, giving a projected range of ∼330 nm. Further it was cut in two, where one was annealed at 600°C, and the second annealed at 800°C.

A Schematic showing all steps in the experimental procedure for the Si and Zn implanted ZnO samples can be seen in Fig. 3.16.

3.12.3.2 Ge implanted ZnO

As with Si, two temperature series were done, referred to as T1Ge and T2Ge, by Ge implantation in ZnO. Initially a $10 \times 10 \times 0.5$ mm^3 ZnO sample of resistivity >1 kΩ-cm was implanted with Ge to a dose of 10^{16} cm^{-2} at an energy of 800 keV, giving a concentration of about $\sim 10^{20}$ cm^{-3} at a projected range of $\sim$ 325 nm. The wafer was cut into four $\sim 5 \times 5$ mm^2 pieces. One piece was annealed at 600°C, a second at 800°C, and a third at 1000°C, while the fourth was kept as implanted. The four samples were then subject to RBS, SIMS, XRD, PL, TDH , SSRM, SEM, and TEM characterization. The sample series were called T1Ge.

The second series, called T2Ge, were Ge implanted ZnO as well, except instead of bulk wafers the ZnO used was a thin film of about 500 nm, made by sputtering. The substrate was half a 4-inch quartz wafer. A 10×10 mm^2 piece was cut out, implanted with a dose of 10^{16} cm^{-2}, with an energy of 600 keV, yielding a calculated R_p =240 nm. It was cut in four equal 5×5 mm^2 , and heat treated the same way as the bulk implanted series (600°C, 800°C, 1000°C, while the fourth was kept as implanted). The samples were then characterized using XRD, and optical transmission spectroscopy.

A Schematic showing all steps in the experimental procedure for the Ge implanted samples can be seen in Fig. 3.17.

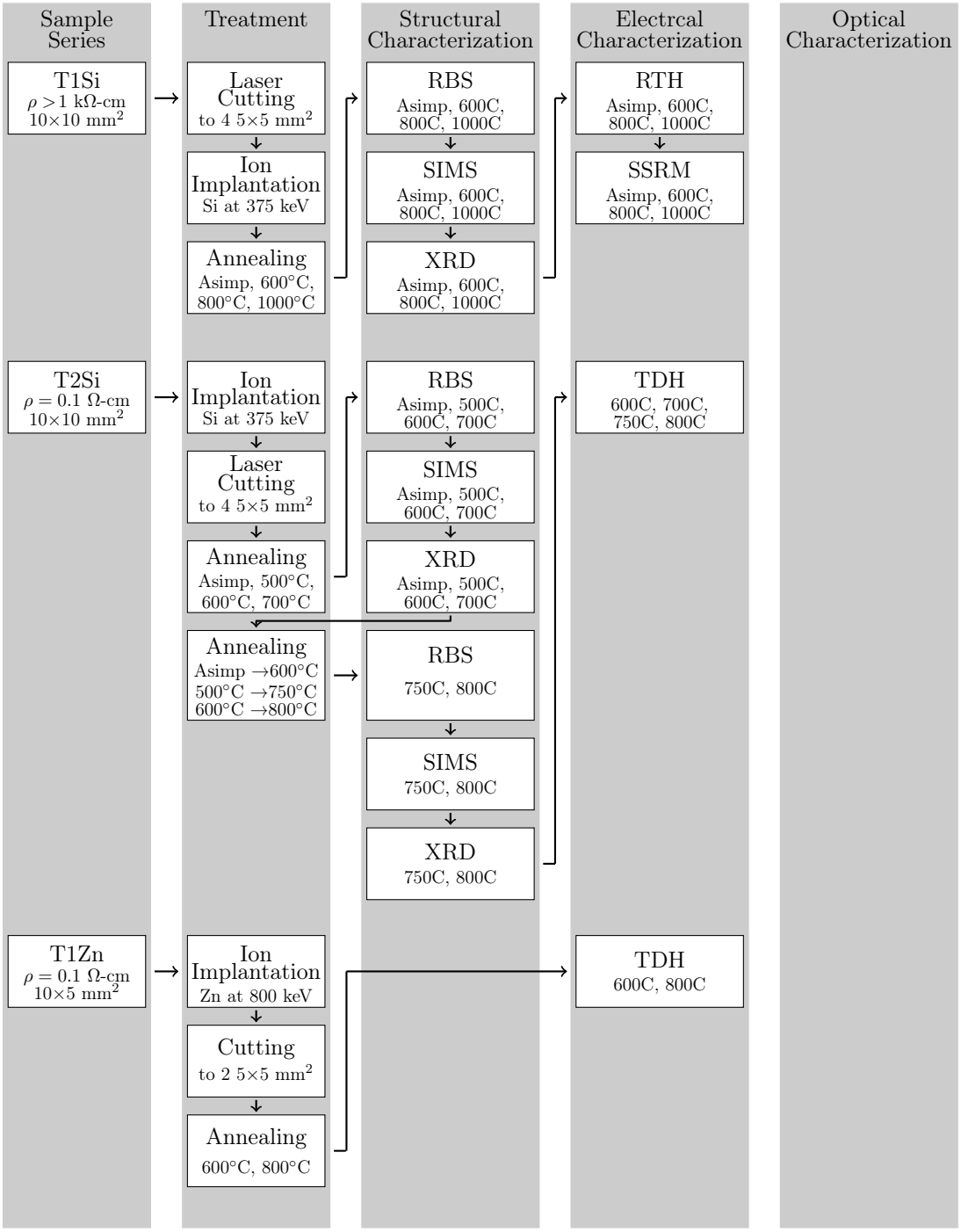

Figure 3.16: Schematic of the experimental procedure steps done in the Si and Zn implanted ZnO.

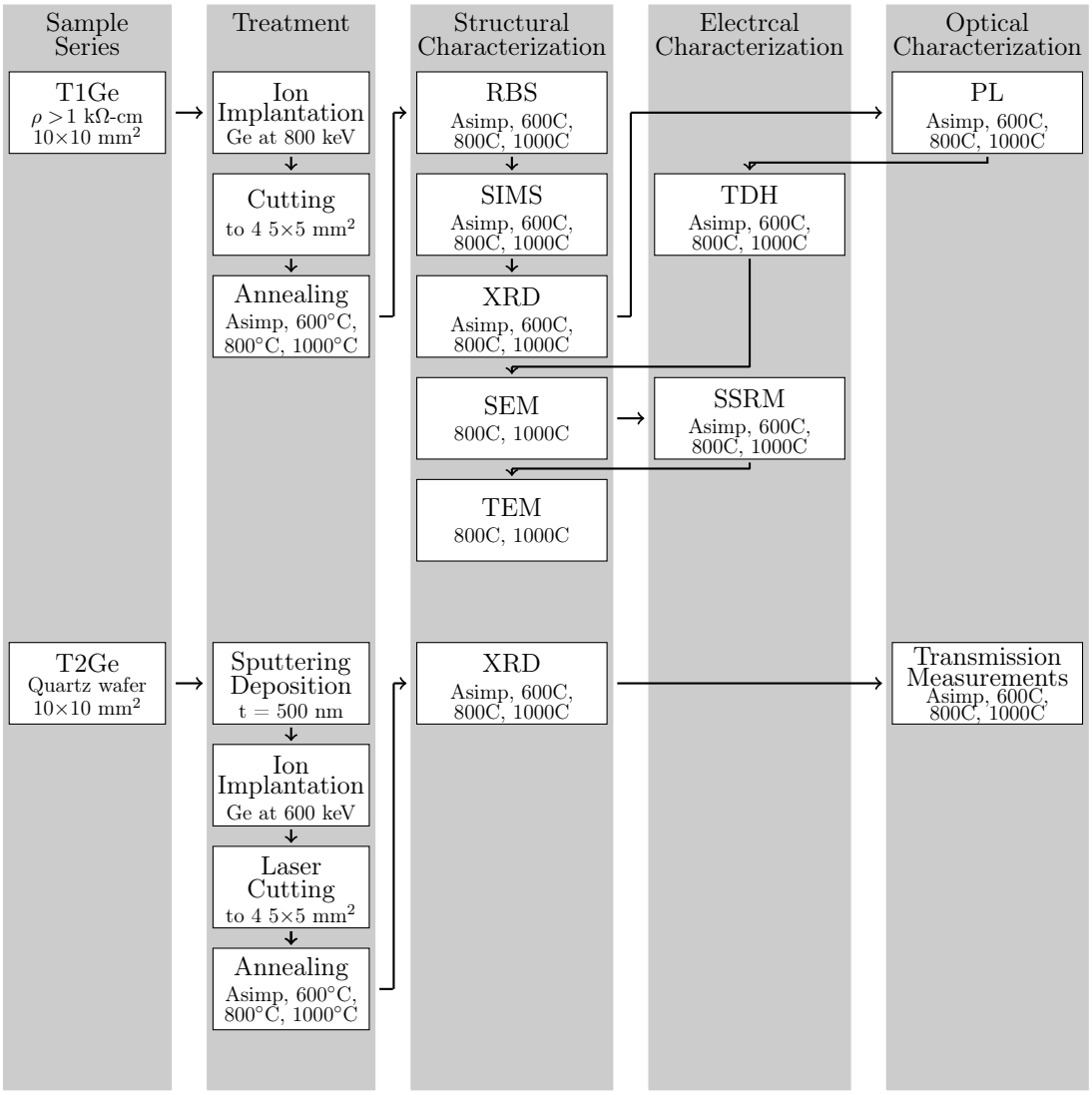

Figure 3.17: Schematic of the experimental procedure steps done in the Ge implanted ZnO.

Chapter 4

Results and Discussion

This chapter presents and discuss the experimental results acquired. Section 4.1 contains the results from the two Si implanted ZnO temperature series, including all characterization methods used. Additionally TDH effect measurement of the Zn implanted ZnO is included in this section, to give additional information about implantation damage versus doping in ZnO. Section 4.2 presents the Ge implanted ZnO temperature series results.

4.1 Si implanted ZnO

The first series of samples (T1Si) were initially considered as references for the samples containing Ge, but interesting results gave way for more research into the system. Annealing temperatures in this series were chosen in a wide range, with big steps (600, 800, and 1000°C). Because of this a new sample batch (T2Si) were Si implanted and annealed to gain further insight in the defect an dopant behavior occurring at annealing temperatures between 500 and 800°C. Lastly, the ZnT1 samples were included for comparison.

4.1.1 SIMS results

SIMS were carried out to monitor the distribution of Si and Li in the samples after annealing and subsequent annealing. As can be seen from Fig. 4.1a), the distribution of Si remains similar between the annealing steps, possibly indicating an activation energy for Si diffusion higher than what is overcome at present annealing temperatures. The projected range of the implant was ∼350 nm, making the SIMS profile slightly deeper than calculated, and there is an approximately ∼ 900 nm thick layer containing a concentration over 10^{19} cm^{-3} Si atoms. The reason for some of the mismatch between the 600C sample and the rest can be that the wafer was cut prior to the implantation, and the 600C sample may have been tilted more than the others during implantation, causing less channeling than in the others.

Fig. 4.1b) shows the Li distribution in the different samples as measured by SIMS. In the as-implanted sample the concentration is constant, giving the concentration of Li in the high resistive Tokyo Denpa samples before annealing. For the 600C sample there is a reduced Li concentration at the tail of the implanted region, extending from ∼800-1100 nm. For the 800C sample, the region behind the concentration peak (∼ 500 nm) has a substantially reduced Li signal extending several μm into the sample. Hence Li has diffused either deeper into the sample, or to the surface. In the 1000C sample the signal is a bit more irregular again, with

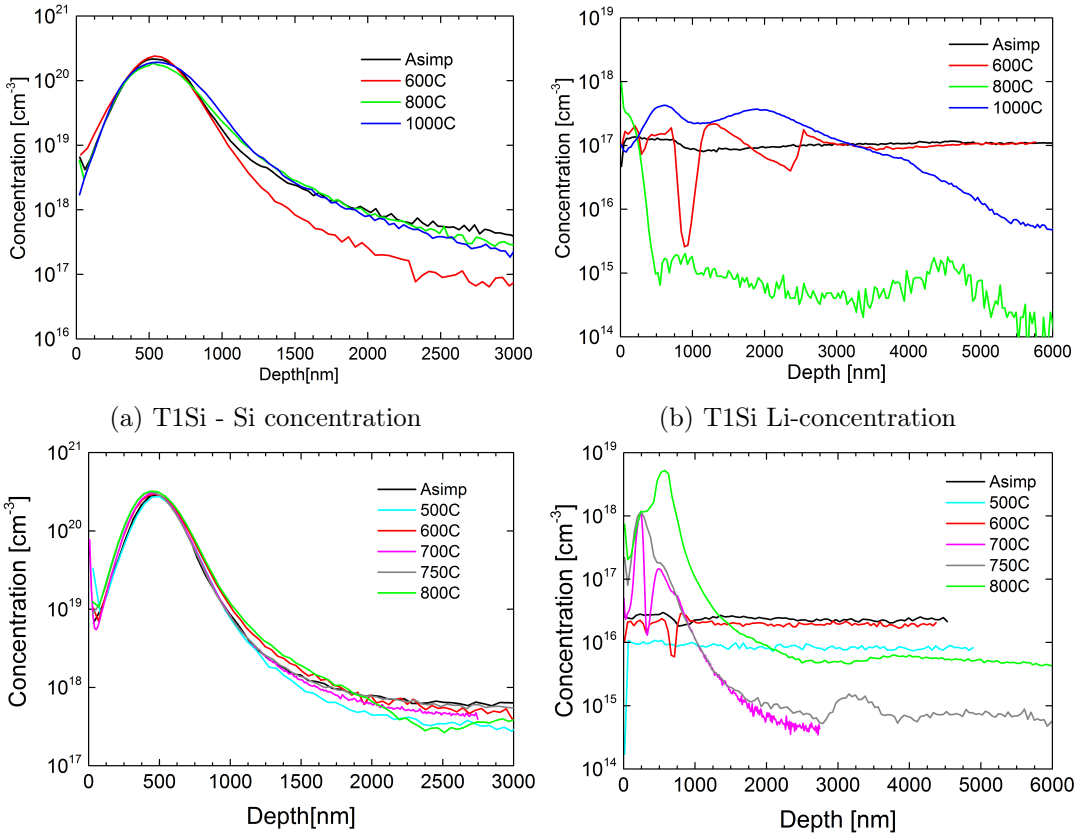

(a) T1Si - Si concentration

(b) T1Si Li-concentration

(c) T2Si Si-concentration

(d) T2Si Li-concentration.

Figure 4.1: SIMS analysis results of Si implanted and annealed ZnO. a) and b) show the Si and Li distribution in T1Si, while c) and d) show the same for T2Si, respectively.

a higher count behind the implantation peak. The depletion of Li in the 800C sample could indicate activation of donors, as proposed by Azarov et al. [36], where annealing at 750-800°C produces Zn_i because of activation of dopants. Zn_i is highly mobile, and will diffuse to the surface, or further in to the material. When Zn_i diffuse deeper into the material it will kick out Li_{Zn} at these depths, and forms Zn_{Zn}. The Li_i formed is even more mobile at this temperature, and will thus be able to diffuse away, ether to the surface or deeper into the material. When a significant amount of dopants are activated, Li can be depleted for tens of microns below the implanted region. This is observed here, shown by Fig. A.1 in appendix A.

The SIMS results of T2Si supports the measurements of T1Si. The concentration of Si (Fig. 4.1c)) is more uniform because all samples had the same implantation angle, due to the fact that sample cutting took place after the implantation. Because of this the implantation peak is narrower, and ∼100 nm shallower than for T1Si. That the peaks remain similar to such an extent regardless of this, confirms that no large scale Si diffusion takes place during annealing. The Li concentration (Fig. 4.1d)) of T2Si further substantiates the results in T1Si, but a buildup of Li is observed at, and slightly behind R_p. In addition the Li tail is increased in concentration, and the depth of the depletion is increased to close to 100μm in the 800C sample and 50μm in the 750C sample. A clear peak evolution can be seen from the 700-800C samples, where the peak at ∼210 nm clearly seen in the 700C sample, stays constant, but the

second peak at ∼500 nm widens and grows considerably with higher annealing temperatures. The Li is likely back-diffused from deeper into the sample, and the buildup could indicate that a Li is trapped near R_p. This is further substantiated by similarities between the Li and Si signal tails, and indicates that a Si-Li complex may be formed, or that Li is collected by V_{Zn}. A figure comparing the long range similarities in Li and Si over a larger range can be seen in appendix A, Fig. A.2.

The Li SIMS profile is significantly different for the T1Si and T2Si 800C samples, with a much higher Li concentration in the T2Si sample. This has not been researched further, but could probably be related either to calibration errors when calculating concentration from count rate, that the T2Si 750C and 800C samples have been sequentially annealed from the 500C and 600C, respectively, or the virgin difference in Li concentration for high and low resistive Tokyo Denpa samples.

4.1.2 XRD results

XRD was employed to verify the crystal quality after the ion implantation and to investigate potential new phases arising after the heat treatments. As seen in Fig. 4.2a) the ZnO (0002) reflection is very pronounced in all samples, which is typical for ZnO [0001] bulk substrates. For the as-implanted and 600C sample there is pronounced shoulders in the (0002) peak. This could be due to strained layers of ZnO inside the crystal, caused by damage from the implantation. ZnO is radiation hard, and some defects anneal out even at room temperature [27, 28], but a substantial amount of ion induced damage is expected, in particular due to the high implantation dose, which may lead to strained layers as observed by XRD. This would explain the shoulders in the as-implanted sample, and would indicate that 600°C is not a sufficiently high temperature to anneal out these layers. The shoulder is not present in the 800C and 1000C samples, indicating that these temperatures are high enough to substantially reduce the strain in th layers. After 1000°C and 800°C, the (0003) reflection is visible as well, which will be discussed further in section 4.2.2. The rest of the small peaks visible in the diffractogram are reflections given from the sample stage of the XRD-instrument. It is worth noting that no Si related peaks are visible, which is consistent with the SIMS measurement, where no change is observed in the Si profile.

Fig. 4.2b) presents XRD results of all annealing steps in T2Si. The XRD measurements confirms the results from T1Si as well, as the shape of the (0002) peak is very similar to the previous series at least at low annealing temperatures. There is however, a larger shoulders in the 800C sample peak for the latter series. The 800C sample in T2Si was subsequently annealed from the 600C sample, and would indicate that the 600°C anneal increases the stability of the strained layers, making 1 hour at 800°C insufficient for removing the entire shoulder, i.e. that the annealing history is important for the resulting defect configurations and concentrations. The (0003) peak is visible in the 600C, 750C and 800C samples as well, indicating good crystal quality.

The FWHM-values of the ZnO (0002) peak is plotted against annealing temperature are shown in Fig. 4.3a) for T1Si. The results show a clear trend, with a close to linear decrease in FWHM-value with increasing annealing temperatures up to 800C, indicating a reduction in defect concentration. In the 1000C sample the FWHM-value increases by ∼0.002° from the 800C sample value, indicating an increase in disorder.

The FWHM-values of T2Si, shown in Fig. 4.3b), do not display the same linear trend. There is a small reduction in ∼0.001° between the as-implanted sample and the 500C sample,

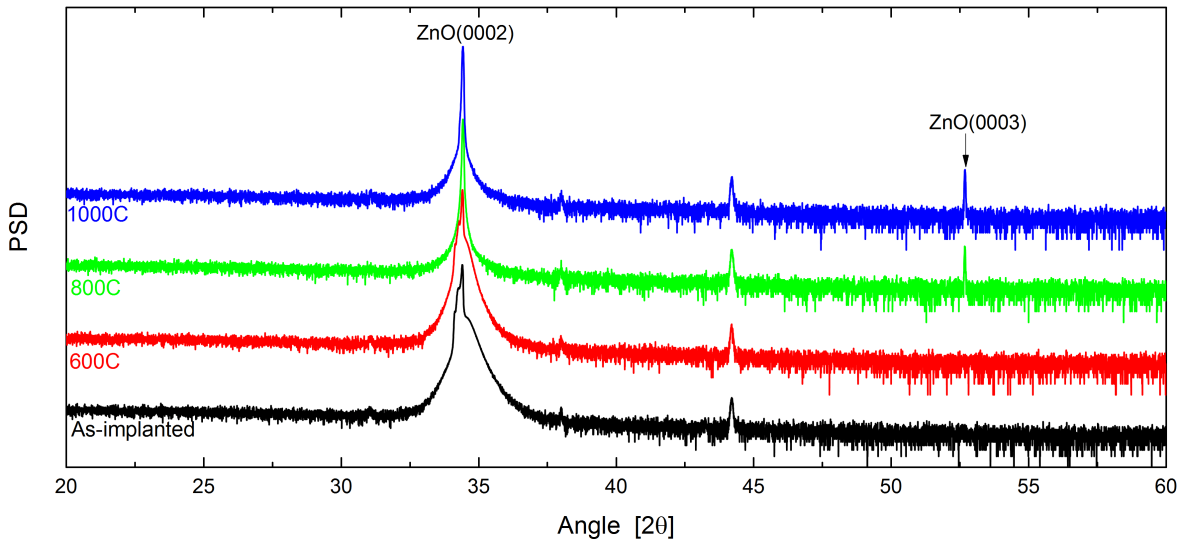

(a) T1Si

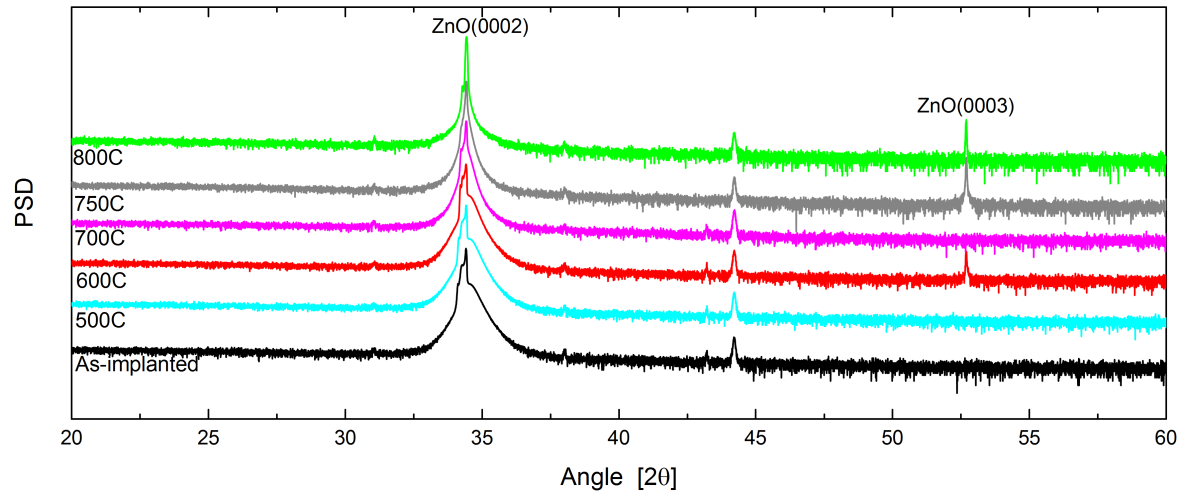

(b) T2Si

Figure 4.2: XRD results.

but a sudden increase of ∼0.011° in the 600C sample. It decreases at 700°C, but is still higher than the as-implanted and 500C samples. Further reduction is observed with annealing at 750°C, making this the lowest FWHM-value observed. The 800C sample shows a substantially higher than all but the 600C sample. This is probably related to that the 800C sample is the same ass the 600C sample, and is thus consistent with observed shoulder width in Fig. 4.2b). The 600C FWHM-value is reduced with annealing at 800°C, but is not enough to anneal the defects out. The same is observed for the 500C and 750C samples, where the 750C sample was made by annealing the 500C sample for another hour at 750°C.

One interpretation of the sudden FWHM-increase could be that these layers are in the process of being annealed into the main structure, becoming less strained, and thus widening the peak quite substantially. However, this hypothesis does not explain why the same effect

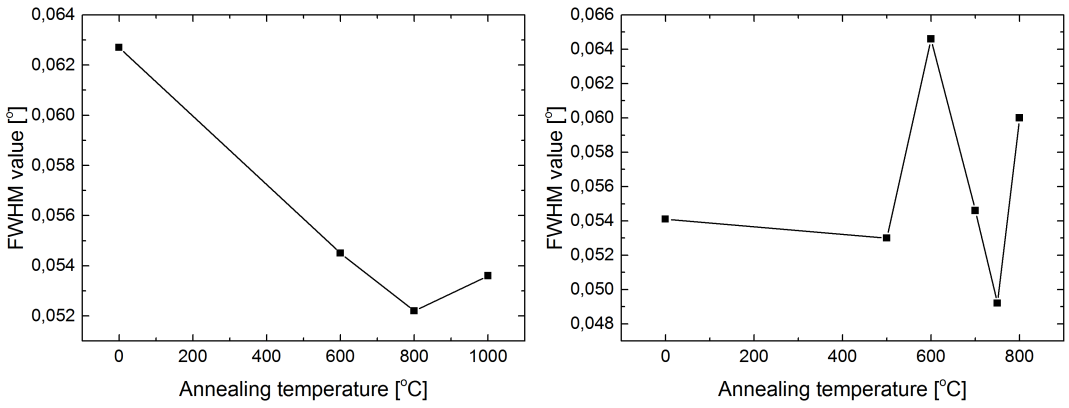

(a) T1Si (b) T2Si

Figure 4.3: FWHM values of the (0002) ZnO peaks in the diffractograms above plotted against annealing temperature.

is not observed in the T1Si-series. The fluctuations in both plots of FWHM-values are small, and it is questionable how much the values reveal of the difference in defect concentrations of the sample. However, the instrument has a broadening factor of 0.008°, but fluctuations due to insufficient instrument accuracy should be negligible at this order of magnitude.

4.1.3 RBS results

As stated above, implantation is expected to induce a high amount of defects in the samples. Thus, the vacancy generation caused by implantation of 500 Si atoms was simulated using SRIM [65]. Displacement energies of 52 and 30 eV was used for O and Zn [82], respectively, and the result is presented in Fig. 4.4. Using observations by Svensson et al. [83], the expected vacancy generation was calculated to be $\sim 6.74 \times 10^{21}$ cm^{-3}, assuming that 1 % of generated vacancies remain after dynamical annihilation. The paper is based on lower doses, and Si material, but it is applied as a first approximation. Since RBS is more sensitive to heavy atoms, Zn displacements in the lattice are the main backscattering source in the case of ZnO, meaning that the O displacements will be difficult to observe in the RBS spectra.

RBS was utilized to obtain further information about the disorder in the implanted region after annealing. The results of the investigation of T1Si can be seen in Fig. 4.5a). The thinner

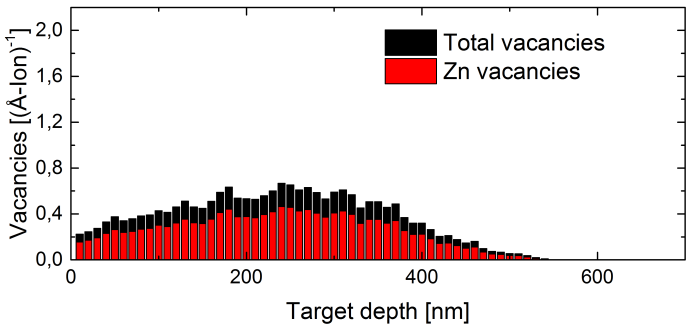

Figure 4.4: The average vacancy generation after simulation of 500 Si impacts.

lines with the high yields, marked with an R in the legend is the random, i.e. unchanneled, signal. It shows the Zn surface at channel number $\sim$ 400 and an O-signal can be seen at channel number $\sim$ 175. The thicker lines at lower yield represent the channeled signal. Here the peak at channel number 400 marks the surface of the samples. The as-implanted and 600C samples show a similar behavior, both containing a significant disorder in the Zn lattice as observed by higher yield. Significant backscattering at larger depths is visible. This could be attributed to a high concentration of extended defects. Many extended defects will not cause dechanneling at their location, but rather skew the ion beam a little, and thus cause dechanneling deeper into the material. The 600C samples channeled signal shows a lower concentration of defects compared to the random signal, but it is higher than the as-implanted yield, especially in the shallower region. Possible reasons for this could be the different tilt angle of the sample during Si implantation, as indicated by SIMS in Fig. 4.1, implying a higher disorder in the sample, or that the sample was not aligned in a perfect channeling direction during the measurement.

Interestingly the 800C and 1000C samples show a yield very close the virgin, i.e. non implanted, sample. This means that the amount of defects in the sample seems to be substantially reduced when the anneal temperature surpasses 800°C. The 1000C sample shows an increased yield compared to the 800C sample. This is consistent with the observations in XRD results, where a larger FWHM-value of the (0002) ZnO peak was observed for the 1000C sample as well. It thus seems to be more defects in the 1000C than in the 800C sample, which is consistent with SIMS and is likely coupled to the suggested formation of the Li-Si defect complex. Li is a very light element, and would not display a large change in RBS signal. However, if Si is displaced as well, it would give a greater backscattering probability, which could explain the higher RBS yield seen in the 1000C sample.

The RBS results of series T2Si support the results in T1Si, but the smaller temperature steps in this series makes it easier to distinguish at what temperature defects disappear. All temperatures can be seen in Fig. 4.5b). The random signal for all temperatures is unchanged compared to T1Si. The channeled as-implanted and 500C sample are very close, meaning that little defect annihilation is present at 500°C. The annealing at 600°C seems to have more effect, while annealing at 700°C does not further improve quality drastically. This supports the suggestion of the T1Si 600C sample not being perfectly aligned, and thus have not channeled properly. At 750°C the sample quality is clearly improved, and further at 800°C the crystal quality is as good as for the 800C sample in T2Si, thus confirming the results of the earlier series. Moreover this implies that annealing of defects seems to increase significantly in the range between 750°C and 800°C.

Due to the large buildup of Li seen by SIMS in the 800C sample, this could be expected to be observed through higher RBS yield for the T2Si 800C sample than for the equivalent sample in the T1Si series, if there is a Li-Si complex distorting Li positions. This is not the case, since the 800C signals are observed to be close to exact replicas. This could indicate that the Li recombines with V_{Zn}, and does not form a Li-Si complex.

χ_{min}, which is the ratio of the minimum yield right behind the surface peak in the channeled signal, and the random signal at the same depth, is plotted against sample name for both sample series in Fig. 4.6, to clarify the trends observed in Fig. 4.5. Starting with the T1Si samples (Fig. 4.5a)), it is consistent with what is observed at greater depths above. The virgin sample has a signal ratio of $\sim$2.4 %, which increases to 4.8 % in the as-implanted sample, due to near surface implantation damage. The high ratio of the 600C sample may be due to the suggestion of a worse alignment of the He beam during measurement of this sample. The 800C sample show a significant improvement from the as-implanted sample, with a ratio of 3.2 %,

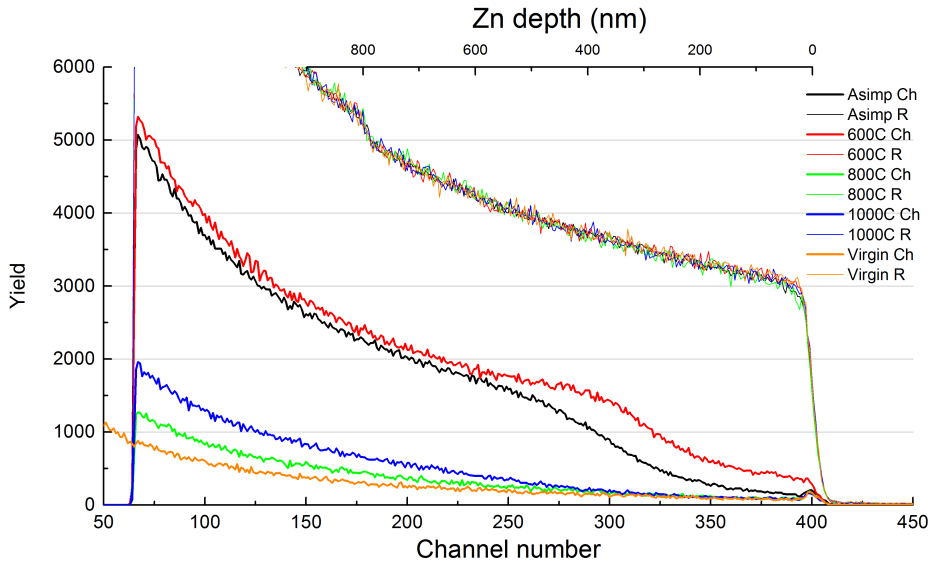

(a) T1Si

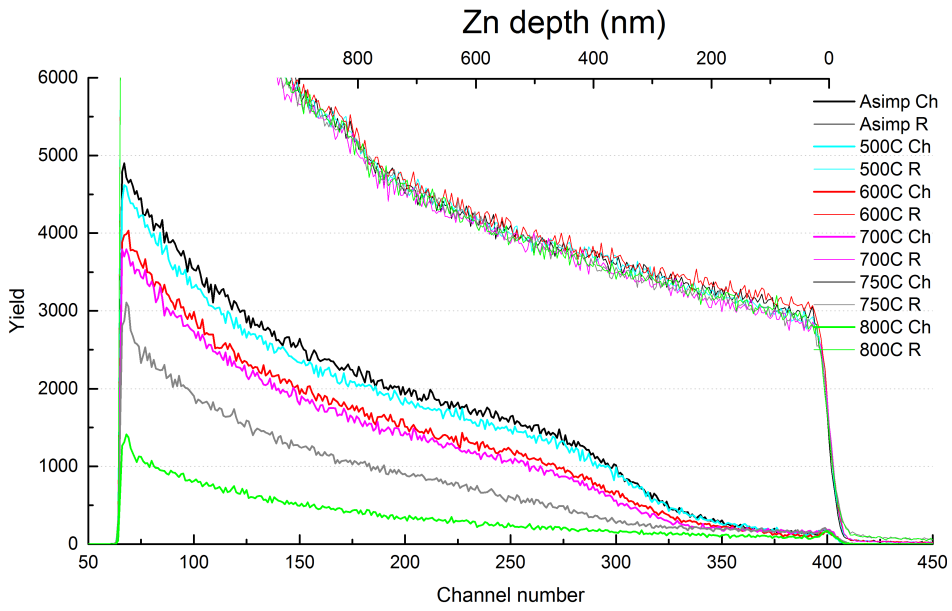

(b) T2Si

Figure 4.5: RBS spectra of the T1Si (a) and T2Si (b) plotted against channel number.

while the 1000C sample shows a value of 2.6 %. This is interesting, as it could indicate that the region near the surface anneals better at 1000°C than at 800°C, despite the RBS yield being lower for the 800C sample deeper into the material. Alternatively, small variations in the incoming He probing beam angle could give large variations of the RBS yield so close to the surface, and thus increase variation. The T2Si samples in Fig. 4.5b) shows substantial variation in the χ_{min} value as well. The 800C sample show a ratio of 2.9 %, which is slightly lower than the T1Si-800C sample, but also indicate a good crystal quality compared to the virgin sample.

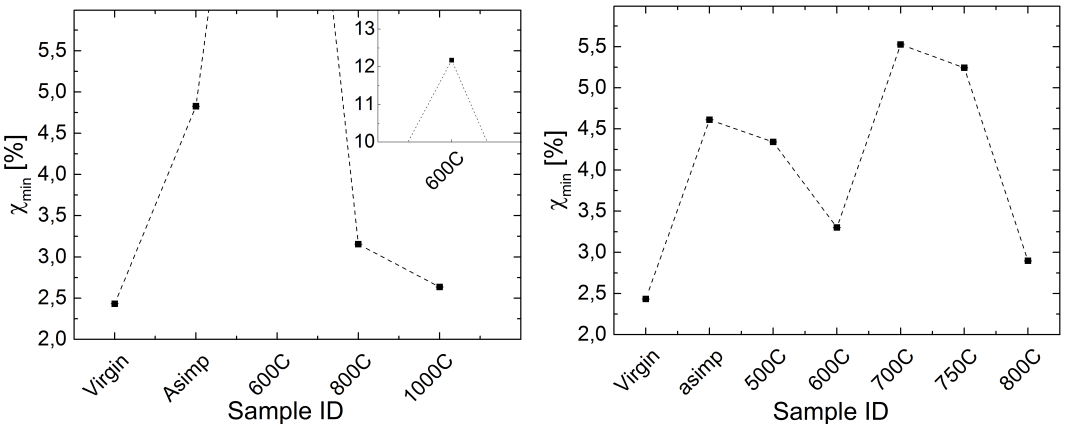

(a) T1Si (b) T2Si

Figure 4.6: The ratio of the minimum yield after the surface peak and the random signal at the same depth, χ_{min}, from the RBS measurements of T1Si (a) and T2Si (b) is plotted against sample ID. The inset in a) shows the T1Si-600C samples χ_{min}.

4.1.4 SSRM results

To measure the conductivity of the samples as function of depth scanning spreading resistance microscopy was applied to the T1Si series, measuring the cross section of the sample. Fig. 4.7 shows the average resistance scanned over a square area of 2×2 or 3×3 μm. The sample edge (the implanted surface) is near the left side in each plot. The tip scanned close to but not over the edge, resulting in an uncertainty in the depth profile of ∼100-200 nm.

Beginning with the as-implanted sample (Fig. 4.7a) has its lowest resistance at R_p, indicating a significant formation of donors in the implanted region. This could imply that a significant amount of Si is activated already at room temperature. The 600C sample has a wider region of reduced resistivity near R_p. This could be caused by activated donors at this range, but in addition the deeper part of the low resistive area matches the depleted Li area seen in the SIMS measurements (Fig. 4.1). Due to the compensating nature of Li in n-type material, this could partly explain the width. The resistivity of the sample will be determined by the sum of defects and impurity atoms. When Li is present, even in the implanted area, it will compensate the Si donor atoms, and effectively increase the resistance, as stated by Vines et al. and Johansen et al. [33, 34] proposing Li_{Zn} as the dominant Li position in n-type material. This could be why the Li depleted area has about the same resistance as the R_p region, where the Si concentration is higher. A lower Li concentration will cause a lower Si concentration to be able to effectively donate more electrons to the conduction band. The fluctuations in resistance near the surface is somewhat consistent with Li concentration as well, but could also be due to contact problems due to a rough surface. The 800C sample shows a low resistance over a wide area. SIMS results show a Li depletion for several microns behind R_p, which explains the lower resistance measured. It can be seen however, that the resistance from R_p and about another ∼500 nm is lowered compared to deeper into the sample, despite the Li concentration being the same or slightly higher than at larger depth, which further indicating good donor properties in Si. Lastly, the 1000C sample shows a generally higher resistance around R_p than the rest of the samples, but lowered compared to the rest of the sample, compliant with the high Li concentration shown by SIMS, but further indicates

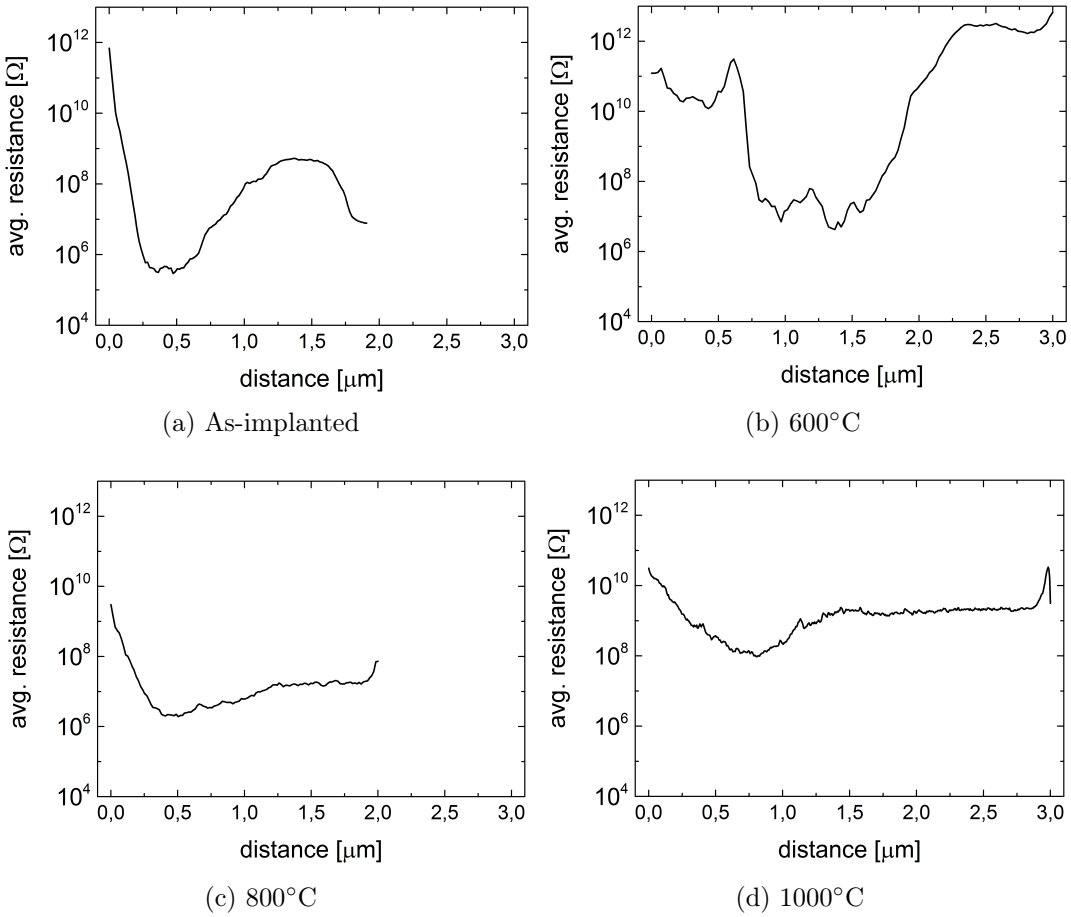

(a) As-implanted

(b) 600°C

(c) 800°C

(d) 1000°C

Figure 4.7: SSRM average resistances from all samples in T1Si, scanned over a square are of 2×2 and 3×3 μm.

that Si has good donor capabilities. In addition the slope towards the surface is not as steep as in the other samples, which is compliant with Li concentrations here as well.

4.1.5 Hall effect measurement results

4.1.5.1 Room temperature Hall effect measurements of T1Si

Room temperature Hall (RTH) effect measurements were applied to monitor the resistivity, carrier concentration, and hall mobility as a function of annealing temperatures in the T1Si series. The results are plotted in Fig. 4.8. However, both the implanted layer and bulk will contribute to the Hall resistance, and must be decomposed in order to extract information about the implanted layer. Hence, in this thesis the results will be used more as a deductive tool for comparison, rather than an exact measurement. A simplified model of a two layer stack has been employed, where all Hall measurement results are based on a conducting layer thickness of 1 μm, meaning it is assumed that all current goes through this thin layer. 1 μm was chosen because this is close to the implantation peak width, and hence regarded as a first approximation. This will be referred to as "the 1 μm approximation" throughout the thesis.

The as-implanted sample has a low carrier concentration of 5.2×10^{14}, but a large mobility

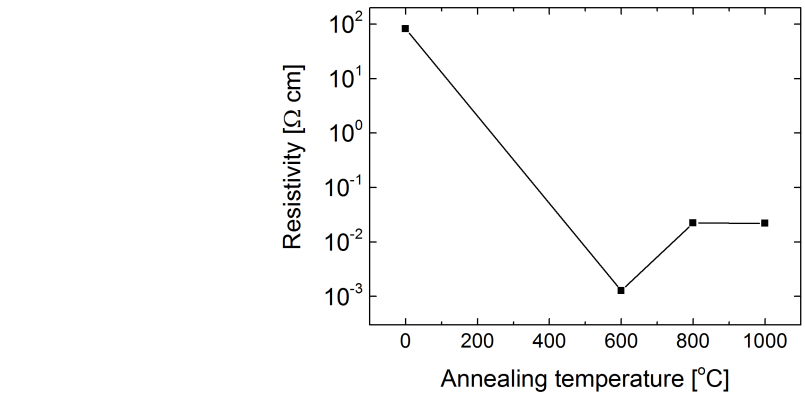

(a) Resistivity

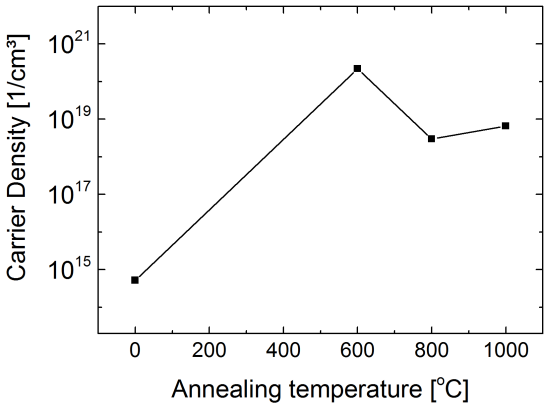

(b) Carrier concentration

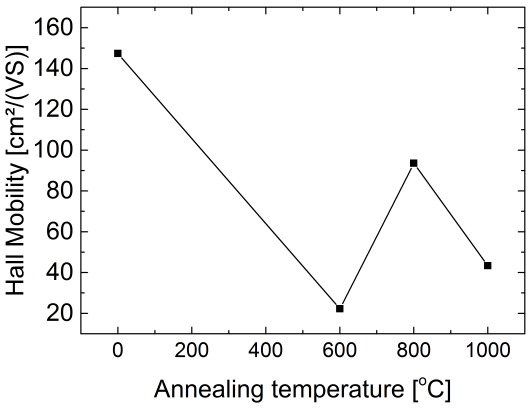

(c) Hall mobility

Figure 4.8: T1Si hall resistivity (a), carrier concentration (b), and mobility (c) plotted against annealing temperature. The Backside of the as-implanted sample is measured in this experiment.

of 147 cm^2/Vs, which in total gives a resistivity of 82.2Ω-cm. This was measured on the backside, i.e. the un-implanted side, making this more of a bulk measurement. This explains the similarity to bulk values. Due to this being a backside measurement, the sample thickness was set to 500 μm for this particular sample. If the implanted layer in this sample is conducting better than the bulk, this would mean that the current mainly go through the implanted layer, and thus the resistivity is lower than as-grown high resistive samples (ρ>1 kΩ-cm). The resistivity would however, be larger than that of a frontside measurement, because of the need to probe bulk as well, hence the large mobility. In the 600C sample the resistivity is reduced substantially, and a value of 1.2×10^{-3}Ω-cm is reached. This indicates that the current mainly flows in the implanted channel and dominates the result. This is further supported by the high amount of charge carriers seen, 2.2×10^{20} cm^{-3}, signifying that the Si dopants are activated at this temperature. The low mobility could be attributed to the high amount of implantation damage, cf. RBS and XRD results, in addition to ionized scattering centers in possible donor ions. The 800C sample shows a higher resistivity of 2×10^{-2}Ω-cm, caused by a decrease in carrier concentration. Based on the low Li concentrations shown in SIMS, the resistivity could be expected to decrease. There is a clear build up of Li at the surface, which could make a highly compensated layer here, and thus increase resistivity. The mobility

could be increased due to an increase in crystal quality, which is in compliance with the RBS and XRD results, but the current is likely to flow in the more conducting depleted region, and thus the mobility is likely to reflect more bulk-like values. The 1000C sample has about the same resistivity as the 800C, with a small increase in the carrier density, but it shows a lower mobility. The reduction in mobility could be due to the increased Li concentration, increasing the ionized impurity scattering in the implanted region, but this does not explain the increased carrier concentration in the sample, which could be expected to decrease due to the high concentration of Li.

4.1.5.2 Temperature dependent Hall effect measurements of T2Si

Temperature dependent Hall (TDH) effect measurements were carried out for the T2Si series. The 1 μm approximation was applied to these measurements as well[1]. The validity of this approximation will be discussed later. The measurements were done on the 600C, 700C, 750C and 800C samples. TDH were only done at the final annealing stages of the series, due to the need for indium contacts deposited in the samples corners.

Fig. 4.9a) shows the sample resistivity as a function of temperature, the solid line represents the 1 μm conducting layer approximation, while the dashed lines show values calculated using the whole 500μm sample thickness. Beginning with the solid line, the 600-750C samples show a low resistivity, $1.4 \times 10^{-3}\Omega$-cm to $2.2 \times 10^{-3}\Omega$-cm even at 20 K. The 800C has a higher resistivity at low temperatures. As the temperature increase all samples behave the same way, and all resistivities end up in the $\sim 1.7 - 1.8 \times 10^{-4}\Omega$-cm range at room temperature. This is very low values for ZnO, and must be treated with caution. The low resistive substrate could yield the 1 μm approximation inadequate, meaning that a sufficient part of the current flows through the substrate as well as the implanted layer, due to the lower differences in resistance between the two layers. This would result in a too high carrier concentration in accordance with eq. 3.12. The results acquired using larger thickness gives a higher resistivity, and at room temperature it is measured to $\sim 8.5{\times}10^{-2}$ Ω-cm. This is only slightly lower than the resistivity values supplied for this low resistive sample batch by Tokyo Denpa (0.18 Ω-cm), indicating that the resistivity in bulk is too close to the implanted layer value, and that current from the TDH effect measurement is a combination of the bulk ZnO and the implanted region. As a consequence, when 1 μm implanted layer is not the main conductor, the results represent most of the bulk sample, and retrieval of specific information from the measurements are difficult. That the resistivity shows a slightly smaller value than un implanted samples does, however, indicate a very a good donor effect from the silicon implantation.

Fig. 4.9a) shows the carrier concentration as a function of the reciprocal absolute temperature and b) the mobility as a function of temperature for all measured samples. Looking at the carrier concentration, the reason for the high resistivity in the 800C sample at low temperature becomes evident. The measured carrier concentration is several orders of magnitude lower than that of the rest of the samples in this temperature range. It can be seen for all samples that the carrier concentration is lowered with decreasing temperature, but past a certain point (1000/T$\approx$12 for the 600-750C samples and 1000/T$\approx$34 for the 800C sample) it seems to increase with lowered temperature. This increase in carrier concentration has been observed previously, and is proposed to arise because of surface currents in the sample that dominate at low temperatures [76, 84]. Look et al. [84] proposed it could be due to hydrogen

[1]The 1 μm approximation was explained in the RTH effect measurement result section above.

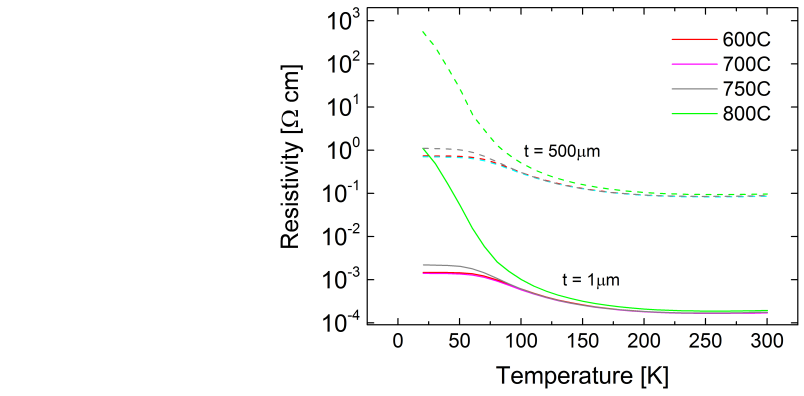

(a) Resistivity

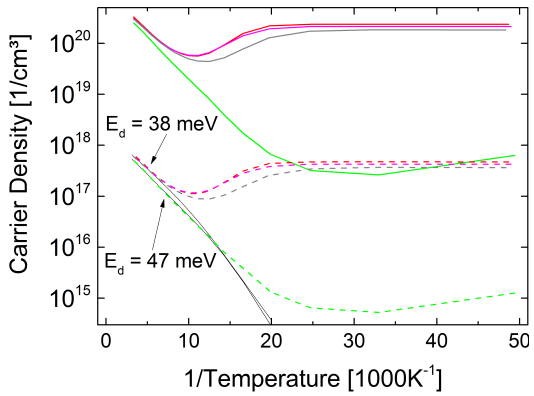

(b) Carrier concentration

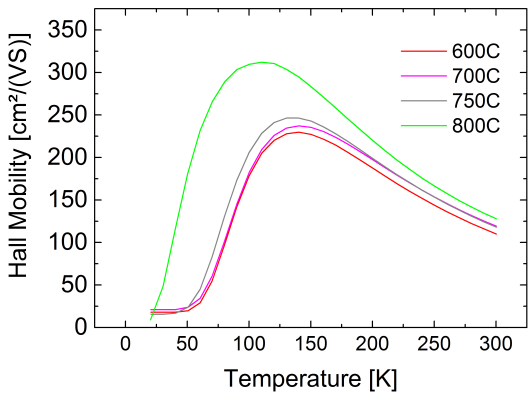

(c) Mobility

Figure 4.9: T4Si TdH results, where a) shows the resistivity as a function of temperature, b) shows the carrier density as function of reciprocal temperature, in addition to calculated energy levels, and c) the mobility as a function of temperature.

donors at the surface, either adsorbed from the ambient, or diffused out from bulk, during annealing. The 800C sample does not show these currents to the same extent, and thus has a significantly lower carrier concentration at lower temperatures, leading to the higher resistivity. This could be supported by the increased Li concentration near the surface in this sample, thus reducing the carrier concentration here, effectively compensating the H donor. This could indicate that the 600-750C samples resistivity, excluding surface currents, should be more similar to the 800C resistivity in shape, where there is less surface currents. The carrier concentration calculated using a uniform sample thickness of 500 μm (dashed lines) shows a carrier concentration over two orders of magnitude lower than the 1 μm approximated samples.

The mobility plots of samples annealed from 600-750°C show a similar mobility versus temperature, with a peak mobility of ~240 cm^2/Vs. For the 800C sample observed peak mobility increases to over 300 cm^2/Vs. This seems to be consistent with the RBS measurement result, where the 800C shows a nearly perfect crystal structure. However, that the mobilities of all samples are substantially higher than expected, even for the 600C and 700C, which in RBS showed a high amount of defects, could further indicate that the 1 μm approximation

is not valid, and thus more than the implanted layer has been probed. Values measured by Schifano et al. in similar HT grown ZnO bulk samples (purchased by SPC Goodwill with $\rho \approx$5.1 Ω-cm) showed a mobility of ∼125cm^{-2}/Vs. These samples have a higher resistivity as-grown, and thus probably more acceptor related defects, but it shows that the mobility in the T1Si samples remain very high and that accepting defects present in the implanted region are negligible. The surface currents could be responsible for a decrease in mobility at low temperatures for the 600C, 700C and 750C samples, meaning that the values might be too low all the way up to ∼150 K. This hypothesis is consistent with results presented by Roro et al. [76], who used a two layer model trying to exclude the surface current contribution to the carrier concentration, as well as the mobility. These calculations lead to decrease in carrier concentration at lower temperatures, which in turn increased the mobility in the same range.

Using the 500 μm values, the dopant energy level were extracted using using the model presented by Schifano et al. [85], where, assuming independent scattering mechanisms (Matthiessen's rule), the carrier concentration and mobility are fitted by using the donor ion-, and acceptor ion concentration, in addition to the donor energy, as input parameters. The rest of the parameters are assumed to be the same as in [85], and a single donor level was assumed as well. The fitted energy levels are plotted along with the carrier concentration in Fig. 4.9. Because of uncertainty regarding surface currents the energy levels are only plotted for the 750C and 800C, giving donor levels of 38 and 47 meV below the conduction band, respectively. If the current probes mainly bulk, there seems to no reason for the donor energies to be different, thus the 800C value would be the most correct, with the energy of 47 meV. This is very close to the well known values for common background donors for Al (52 meV) and Ga (55 eV) [86], which further indicates that these TDH measurements probe mainly bulk material.

4.1.5.3 Temperature dependent Hall effect measurements of Zinc implanted ZnO

TDH measurements were done on Zn implanted low resistive ZnO as well, and the resulting resistivity, carrier concentration, and mobility are displayed in Fig. 4.10a), b), and c), respectively. The resistivity presented with the solid line is calculated using the 1 μm approximation, while the dashed lines are calculated using the whole bulk sample width of 500μm. Starting with the 1 μ resistivity, it shows a very similar behavior to the Si implanted samples. The measured room temperature resistivity is ∼1.9×10^{-4} for both the 600C and 800C samples. This is a very low value of resistivity, indicating that either Zn is a very efficient, or that the 1 μm approximation is flawed for these samples as well. The dashed lines show a room temperature resistivity of ∼9.5×10^{-2}-0.1 Ω-cm, which is very close to the low resistive virgin sample resistivity, given as 0.1 Ω-cm by Tokyo Denpa. This indicates that the measurement current probes the whole sample thickness, and thus that the donor contribution from the ∼1 μm thick Zn implanted layer is close to negligible. The carrier concentration show the presence of surface current in the 600C sample, while the 800C sample does not, which could further substantiate that Li compensates the surface at 800C, since Zn_i is expected to be responsible for the Li depletion, it should be present in these samples as well because of the high dose Zi implantation done. The effect of surface currents, as observed for the Si implanted samples, is consistent with these measurements, where both the resistivity and mobility decrease and become degenerated at lower temperatures. In contrast, the 800C sample show the same trends as the 800C sample in the Si implanted sample, where the low temperature degeneracy in the resistivity and mobility is not present, indicating that values for both properties should be higher in this range, and thus making the 600C and 800C Zn implant profiles more similar.

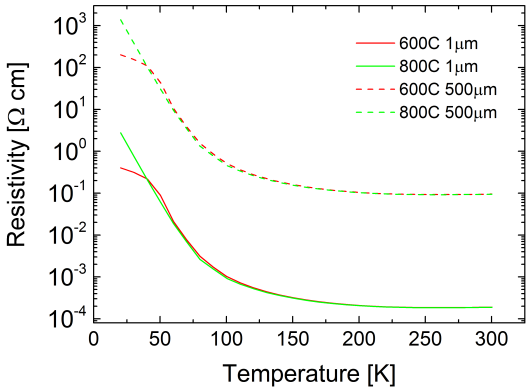

(a) Resistivity

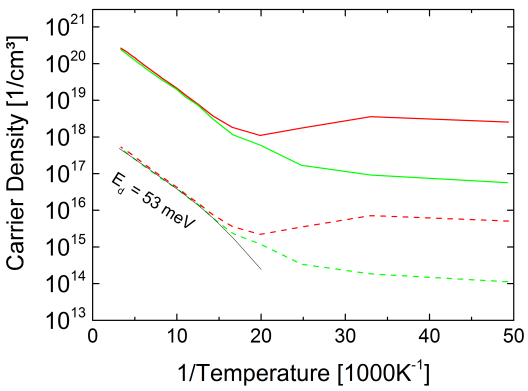

(b) Carrier concentration

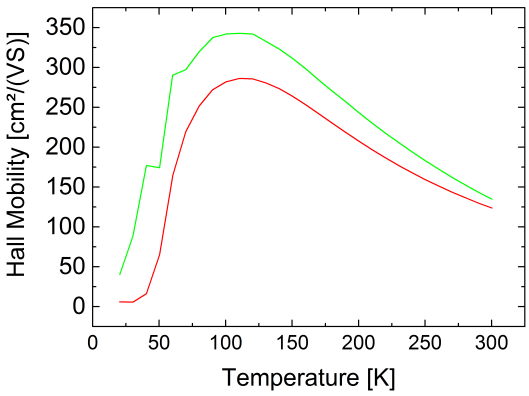

(c) Mobility

Figure 4.10: T4Si TdH results.

Energy level calculations done using the same theory as in the T2Si section above, gave very similar values to that of the Si implanted samples (53 meV), further indicating that no information about dopant levels in the implanted region can be extracted, because of negligible probing of this volume.

4.1.6 Si implanted ZnO - effects of doping and defect annealing

To summarize, the SIMS data show that the distribution of implanted Si atoms is stable for annealing temperatures up to 1000°C. Thus, to overcome the activation energy for Si diffusion higher annealing temperatures have to be applied. RBS results give good indications of strong annealing kinetics of Si implanted ZnO. The lattice recovers better and at lower temperatures than for many other elements [43, 52], and an annealing temperature of 800°C gives a very close to virgin ZnO crystal quality. SSRM characterization indicate a donor generation in the implanted region, with a significant reduction in resistance in the as-implanted sample, as well as the additional samples, implying that Si is activated as a donor already at room temperature. It also shows compensation effects which are most likely due to high Li concentrations present, and acceptor defects known to arise after implantation [29–32]. Hall effect measurements support the SSRM results, and further indicate that Si is an efficient n-type

dopant in ZnO by lowering resistivity several orders of magnitude in high resistive ZnO samples. The 1 μm approximation seems to work well on the high resistive ZnO series T1Si, at least for the 600C sample, where the Li concentration remains high in the implanted region and beyond. The higher mobility in the T1Si-800C sample compared to the 600C and 1000C further agrees with RBS measurements, indicating good annealing kinetics. The increase in mobility could be caused by that the Li depletion seen in the SIMS results (Fig. 4.1) lead to the current probing the un-implanted bulk beyond the implanted region in addition to the highly Si doped implanted layer, due to a decreased difference in resistivity in the implanted layer and bulk. This Li depletion can extend for tens of microns into the material, as showed in Fig. A.1 in appendix A and by Azarov and Neuvonen et al. [35, 36]. This is compliant with SSRM measurements as well where a lower resistance is measured behind the implanted region, compared to the rest of the samples. The 1000C sample in T1Si show a lower resistance near the surface, but higher values than the rest of the samples in the implanted region, and high resistance values beyond. This is consistent with Li concentrations measured by SIMS, showing a small Li depletion near the surface, and large concentrations beyond.

TDH effect measurements done on low resistive samples, are however, not as conclusive due to indications that current probes a larger region than the 1 μm implanted area applied as the sample thickness as a first approximation. This is likely due to the low concentration of compensating Li in the low resistive ZnO samples, making the difference in resistivity between the implanted layer and bulk too small for the 1 μm approximation, where bulk current is assumed to be negligible. The high mobility reached in most TDH effect measurements further substantiate this by showing bulk values. The Si implanted samples did, however, show a slightly lower resistivity than the Zn implanted samples, further indicating that Si is an efficient donor. This is to some extent inconsistent with results presented by Izawa et al. [50], where the main resistivity reduction in Si implanted ZnO was related to generation of Zn_i. Results gathered in this thesis indicate that Si is the dominant donor at annealing temperatures from 600-750°C. This is because the extreme case of Zn implanted ZnO is expected to produce more Zn_i than an Si implantation, and even though Zn implantation seemed to reduce ZnO resistivity, measurements done on the Si implanted material resulted in a larger reduction. However, caution must be taken due to the influence of the large Li depleted region which is low resistive and may contribute to the conductivity, as seen from SSRM measurements. Calculations of the energy levels of present dopants in the TDH measured samples were done, where common bulk values for Al (52 meV) or Ga (55 meV) was indicated.

In addition SIMS show a Li buildup after annealing at 1000C for the T1Si sample, but a substantial buildup is seen already at the 700C sample in T2Si, and is increased for higher annealing temperatures. This is likely related to change in the Li concentration between T1Si (high resistive) and T2Si (low resistive), or that sequential annealing was preformed on the T2Si 750C and 800C samples. The build up could be due to either a Si-Li complex, or that the Li is trapped near R_p. At high Fermi levels ZnO has been shown to self compensate, by creating V_{Zn}, which could indicate that as the dopant activation of Si increases, more V_{Zn} will be available to trap diffusing Li_i, thus vacancy trapping is a valid candidate.

4.2 Ge implanted ZnO

Ge implanted ZnO is a key research area in this thesis, and because of interesting structural observations it is more extensively characterized than the Si implanted samples. Mainly the

results presented are gathered from the T1Ge series, where structural, electrical and optical measurements were utilized to monitor the properties of Ge implanted ZnO after annealing at 600°C, 800°C, and 1000°C. XRD and optical transmission were done on the sputtered ZnO thin films in T2Ge.

4.2.1 SIMS results

Fig. 4.11 shows the results from SIMS characterization of the T1Ge series, where Ge ions have been implanted in bulk ZnO with a dose of 1×10^{16} cm^{-2}, an energy of 800 keV, and a simulated R_p near 350 nm. The as-implanted and 600C sample have peak concentrations on the order of $\sim2\times10^{20}$ cm^{-3}, with a peak depth slightly deeper than R_p. The peaks in both samples show the approximately the same shape, indicating little diffusion of Ge at 600°C. Some diffusion may be present in the tail of the implantation peak, and can be caused by an increased amount of defects in this area, due to implantation damage. The 800C sample, on the other hand, has a substantial increase in SIMS intensity. Since the implanted dose is the same for all samples, and no other source of Ge is expected during annealing, this strongly indicates a matrix effect in the Ge signal, i.e. change in the ionization efficiency of secondary ions. This implies that the local environment around the Ge during the ionization process has changed, which one would expect from a precipitation or formation of another phase. The 1000C sample shows the same matrix effect, but at this temperature there is peak formation in the SIMS intensity, indicating larger accumulation of Ge at these depths. This further indicates either an increased growth of phases also existent in the 800C sample.

Fig. 4.11b) shows the Li secondary ion signal gathered from the samples. The results are very similar to the the Si implanted samples for the 800C and 1000C sample. The 800C sample shows depletion at R_p, while the 1000C shows an slightly higher signal than the rest, with the same fluctuations seen in the Si series. The two lower temperatures, however, seems to act slightly different. The as-implanted sample has a small depletion region around 1000 nm, while the 600C sample shows a quite large depletion beyond ∼1100 nm. The latter is similar to the depletion around 1000 nm in the Si implanted 600C samples, but both samples show signs of charge buildup-effects during SIMS measurement. It is especially visible in the as-implanted sample, where the intensity is reduced and noise increased, and then after sufficient time and charge buildup, an electric breakdown occurs, and the secondary ion concentration increases. This is could also explain why the as-implanted Ge profile has a lower value than the 600C sample in the implantation tail.

The higher Li concentration in the 1000C sample is as mentioned above similar to the T1Si 1000C sample. This could further indicate that there is in fact a Li complex present, and could mean that the hypothesis of Li_i recombining with Zn_v is more likely, or that, since Ge_{Zn} and Si_{Zn} is expected to have similar qualities [44], similar Ge-Li complexes, as proposed for Si, could be made.

4.2.2 XRD results

XRD was executed on both the T1Ge and T2Ge series. Starting with T1Ge, the measurements were preformed with 2θ angles ranging from 10 to 80°, and are shown in Fig. 4.12. In the as-implanted sample, several peaks are present. The ZnO (0002) is observed at ∼34.4° and the ZnO (0004) at ∼72.5°. Smaller peaks diffracted from the sample stage of the instrument occur at ∼44.2°, 64,5°, and 77.5°. The 600C and 800C show no change compared to the as-

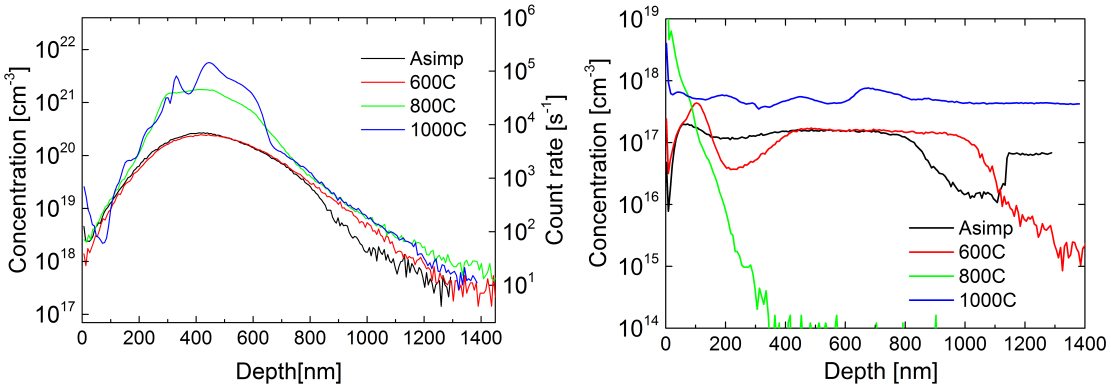

(a) Ge concentration and count rate

(b) Li concentration

Figure 4.11: T1Ge SIMS results, where the Ge concentration and count rate is plotted against temperature (a) an the Li concentration against depth (b).

implanted sample, except ZnO(0001) and ZnO(0003) both showing at 800C. This is dependent on the sample orientation, and will be discussed later. The 1000C sample does show a new phase, identified as Zn_2GeO_4. Three different reflections of the same crystal direction are visible, giving a very good indication that the phase is present. The preferential growth direction seems to be $(11\bar{2}0)$ for the Zn_2GeO_4 crystals. This is consistent with the 1000C T1Ge SIMS results, where there is strong indications of the presence of new phase. That no new phase is observable in the 800C sample for XRD, as indicated by SIMS, could be because the crystallites are too small, or few to be detected, and will further be elaborated in section 4.2.5.

Fig. 4.12b) shows a diffractogram including the four annealing stages of the T2Ge series, with 2θ values varied from 20-60°. The results support those of the T1Ge samples, regardless of large differences in the fabrication method. In the as-implanted sample only the ZnO (0002) peak is visible, with a significantly lower peak intensity than the bulk samples. This is most likely due to more imperfections in the crystal, i.e. poor crystal quality, in the sputtered ZnO films in general. No new phases are visible in the 600C and 800C samples, but in the 1000C there is an indication of the Zn_2GeO_4 phase, seen in the bulk sample as well, but with lower intensity than in T1Ge. In addition it is shifted about ∼0.5°, from ∼25° to 25.5°. This signifies a smaller d value, and that the crystallites might be subject to large strain in these films, causing a reduced bond length.

The FWHM values of the ZnO (0002) peaks in the diffractograms of both series can be seen in Fig. 4.13. For T1Ge, in Fig. 4.13a), a clear improvement of crystal quality can be seen. Here too, the as-implanted sample has a lower value than the 600C and 800C samples, but from 600-1000°C a clear reduction can be seen with increased annealing temperature. This indicates that annealing of defects takes place in this range, because a sharper peak in the XRD diffractogram indicates less deviations from the perfect lattice. Secondly the FWHM-values are generally higher than those seen in the Si implanted samples. Both latter observations are in good agreement with the RBS-results.

Fig. 4.13b) shows the FWHM values for T2Ge. Here a more pronounced trend is seen, with a halving of the FWHM value from as-implanted to the 1000C sample. The large reduction can be ascribed to the increase in sputtered film quality with annealing, shown in [37], and not only due to implantation damage. Compared with bulk ZnO FWHM values from the earlier

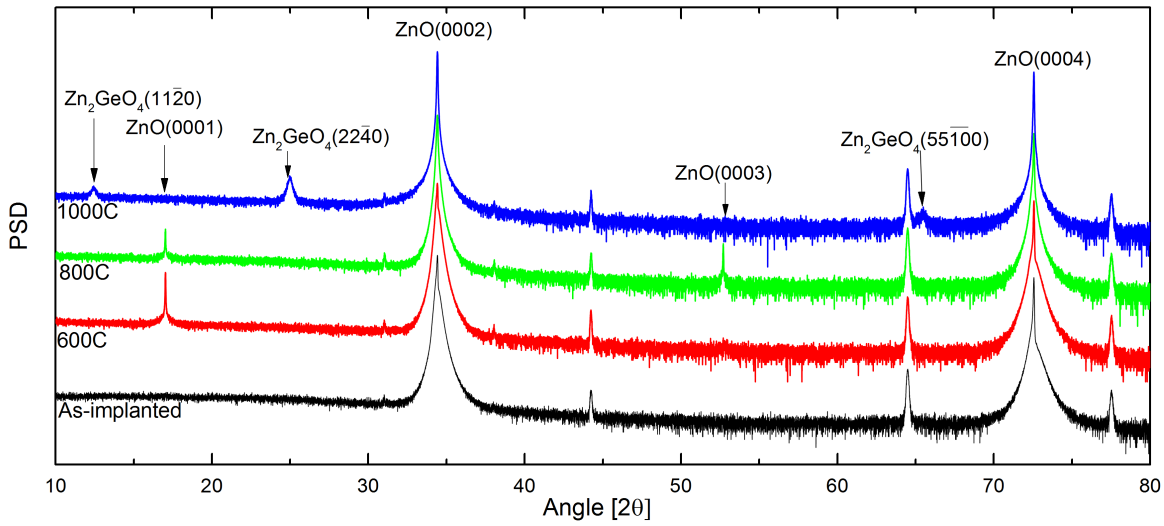

(a) T1Ge

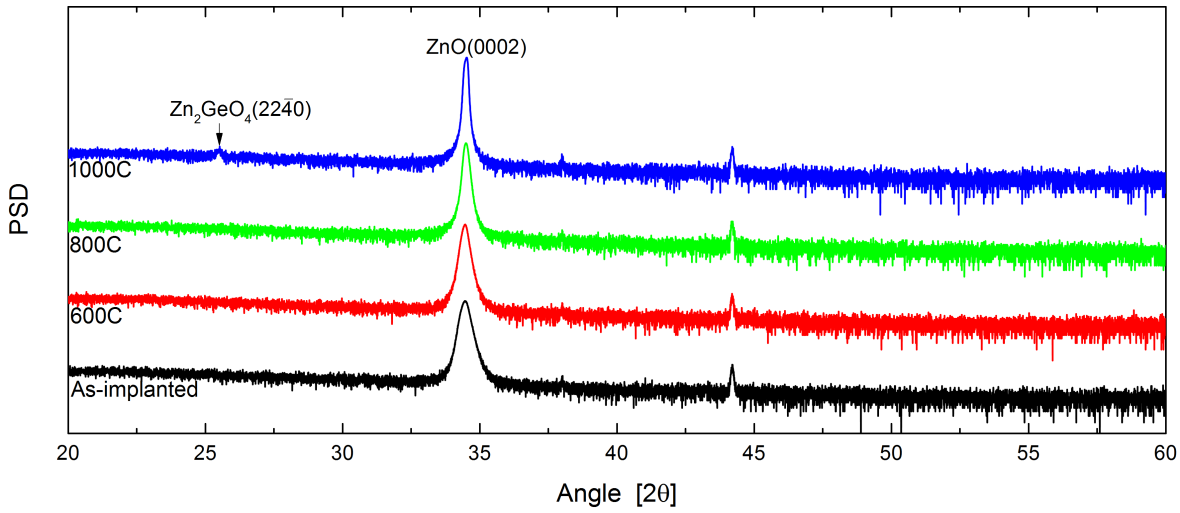

(b) T2Ge

Figure 4.12: XRD results of both Ge temperature series.

series, there is a close to 5 times higher value for the sputtered films, further supporting an overall improvement of the film.

The ZnO (0001) and (0003) peaks have been mentioned and observed in several of the bulk ZnO diffractograms. This is normally forbidden reflections, not visible in bulk samples, and the fact that they are visible here is often related to a good material quality for a range of materials [87]. A phi scan was done, and the result can be seen in Fig. 4.14. Interestingly, the (0001) peak show a rotational period, with a peak at every $\sim 5°$. The intensity in between peaks are zero. Similar behavior is seen for the (0003) reflection as well, except for a longer period of $\sim 10°$. The third reflection seen in the figure is the (11$\bar{2}$4) reflection of ZnO. It is a peak known to vary with phi rotation, and is there for comparison. Moreover, the (0001) and (0003) signals seem to be extinguished at the (11$\bar{2}$4) reflection angles. Therefore, the phi-scan

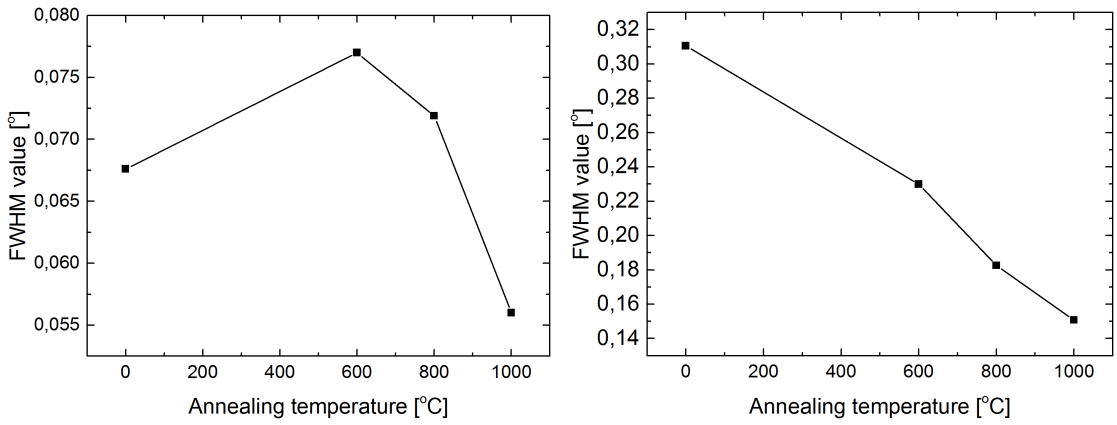

(a) T1Ge (b) T2Ge

Figure 4.13: FWHM-values of the (0002) ZnO peak plotted against annealing temperature for T1Ge (a) and T2Ge(b).

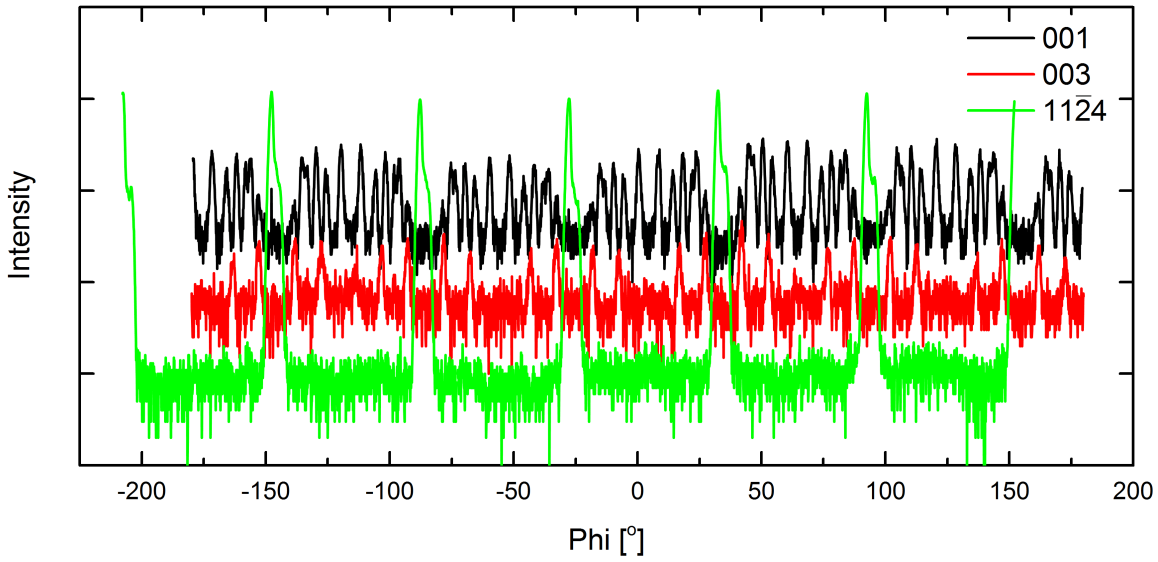

Figure 4.14: T1Ge XRD phi scan results, showing the XRD intensity as a function of phi-angle.

explains the occurrence of the (0001) and (0003) reflections in figs. 4.2 and 4.12, but the origin of the behavior seen in Fig. 4.14 was not investigated further.

4.2.3 RBS results

The RBS results obtained from T1Ge are shown in Fig. 4.16. The random signal is the same as in the Si implanted series, while the as-implanted sample signal is significantly higher. Near the implantation peak (∼400 nm) the backscattered yield is increased by 1000 counts, and deeper into the material it is near doubled. This strongly indicates more implantation damage in the ZnO matrix, with more point defects at R_p and a larger presence of extended defects. This can be accounted to Ge being both bigger and heavier than Si, and the acceleration

voltage increase from 375 keV for Si to 800 keV for Ge. This increase was necessary to get the R_p of the Ge implantation to the Si depth, because of increased stopping power in ZnO for Ge. This is supported by the Monte Carlo simulations of the vacancy generation using the SRIM code for the implantation of 500 Ge ions with the same parameters as in T1Ge, shown in Fig. 4.15. A similar first approximation calculation as done in section 4.1.3 gives a generated vacancy concentration of 2.05×10^{22} cm^{-3}, which is close to three times higher than that of the Si implanted samples.

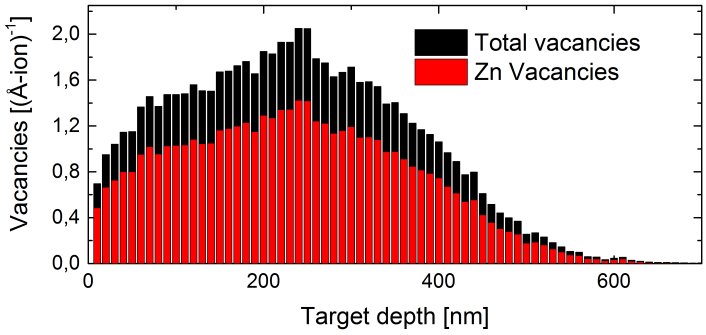

Figure 4.15: The average vacancy generation after simulation of 500 Si impacts.

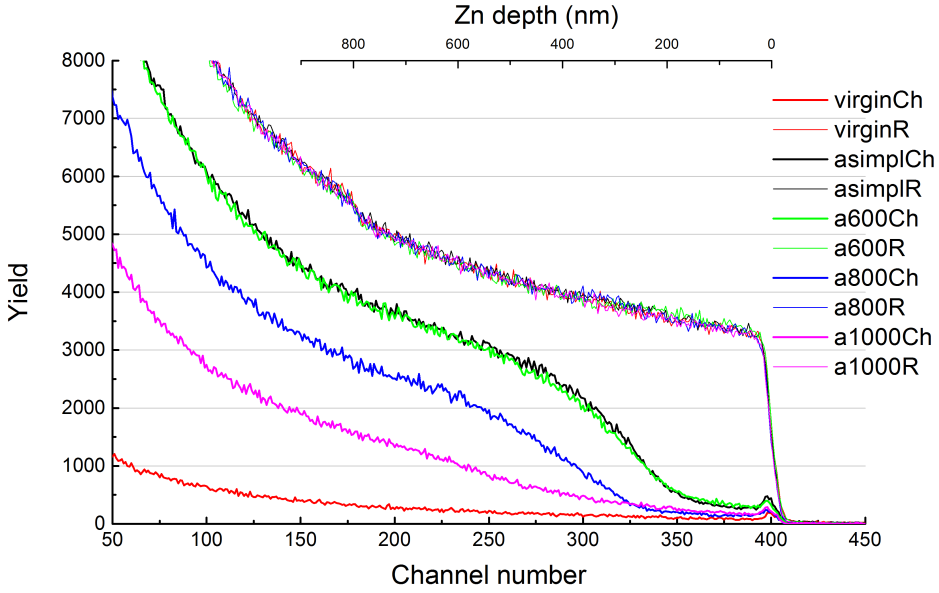

Figure 4.16: T1Ge RBS spectra.

No difference in RBS yield is observed for the 600C compared to the as-implanted sample. A reduction is seen for the 800C sample, and further a slightly larger reduction is seen in the 1000C sample. This indicates that 600°C is not a high enough temperature to promote diffusion, and thus recover the crystal structure of the material. This is consistent with RBS measurements from the Si series, and to some extent XRD, where there is little change between the as-implanted and 600C sample at this annealing temperature. The larger accumulation of damage during implantation could account for the changes observed in the Li distribution

for the as-implanted and 600C Ge samples, compared to the same samples in the Si series. Annealing at 800°C improves lattice quality, with a further increase in quality at 1000°C, meaning that both temperatures are sufficient to anneal out defects, but that 1000°C is a more efficient temperature. But even after a 60 minute 1000°C anneal, the concentration of defects in the Ge samples are similar to that of the as-implanted samples in the Si series. This ca be due to the increased implantation damage accumulated with Ge, but contributions from the new phases indicated by SIMS may also play a role, or Ge could be a poorer fit at ZnO lattice sites, and thus remain interstitial to a larger extent. The latter is inconsistent with first principle calculations done by Lyons et al. [44], where Ge_{Zn}^{2+} is expected to have slightly lower formation energy than Si_{Zn}^{2+}, and Gei is calculated to be higher in energy by at least 10 eV.

The ratio of minimum yield of the channeled beam right below the surface and the random beam is shown in Fig. 4.17. The ratio for the as-implanted and the 600C samples, 8.4 % and 8.9 % respectively, are significantly higher than the equivalent samples in the Si series, which further indicates the larger amount of disorder accumulated in the sample, compared to Si, when Ge is implanted. Even at annealing temperatures of 800°C and 1000°C the the ratio remains 4.7 % and 5 %, respectively, which is close to the as-implanted values for the T1Si samples (4.8 %).

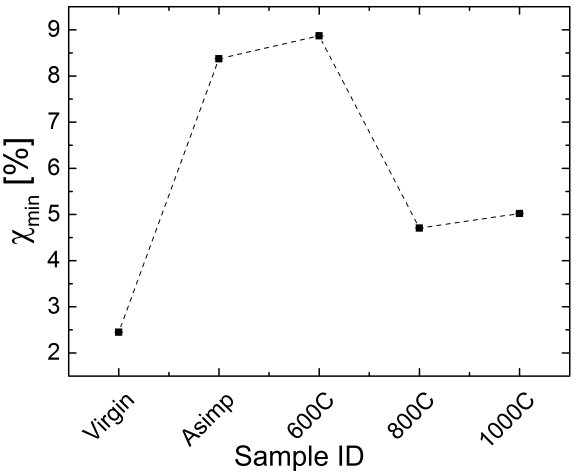

Figure 4.17: The ratio of the minimum yield after the surface peak and the random signal at the same depth, χ_{min}, from the RBS measurements of T1Ge plotted against sample ID.

4.2.4 SEM results

The morphology of the surface in the craters formed for PL in T1Ge were obtained by scanning electron microscopy. The result can be seen in Fig. 4.18, where a) and b) show the bottom of the shallow craters, while c) and d) show the crater edges in the 800 and 1000C sample, respectively. Fig. B.1 in appendix B show a lower magnification of the craters in the 800C sample. Crater size is approximately 300×300 μm^2. Starting with Fig. 4.18a), the bottom of the shallow crater of the 800C sample at 60k magnification, a very rough surface is observed where the material looks close to amorphous, with pores in the ∼10-20 nm range. The same is observed in the 1000C sample, in Fig. 4.18b) at 45k magnification, where larger grains ∼100 nm can be seen as well. These grains could indicate the presence of a precipitate or second

phase being formed in this sample. The porous surface is likely to stem from the sputtering of craters, and thus be traces of ion bombardment. Further indications of this can be seen in Fig. B.3 in appendix B, showing a image series starting inside the crater and moving towards the sample surface.

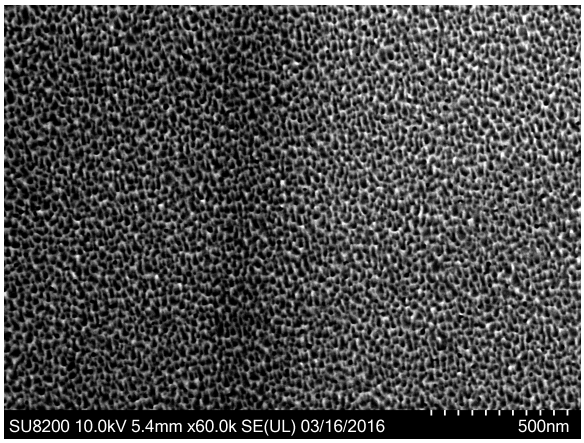

(a) Crater bottom 800°C

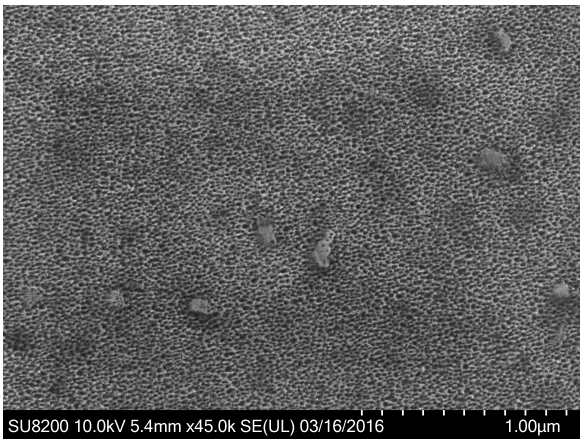

(b) Near crater bottom 1000°C

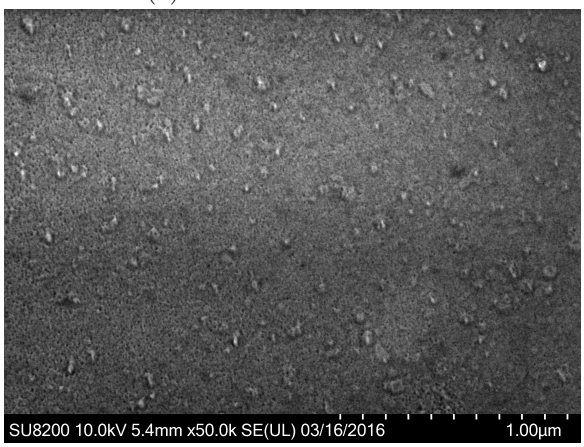

(c) Crater edge 800°C

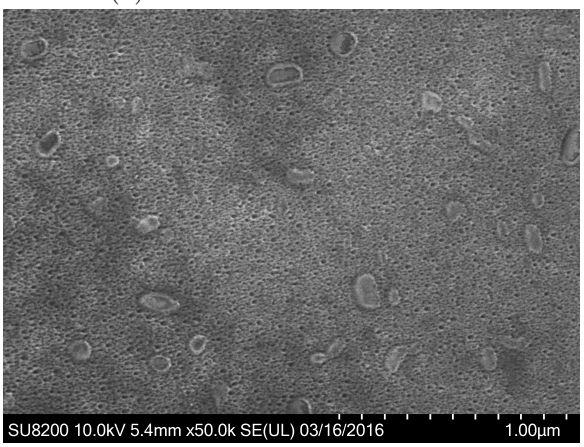

(d) Crater edge 1000°C

Figure 4.18: T1Ge SEM images in the crater edges. a) shows the 800C sample, with $\sim$ 30nm crystallites visible. b) shows the 1000C sample, here the crystallites have substantially increased in size to $\sim 100 - 150$nm.

Closer investigation of the crater edge of the 800C sample revealed the presence of small grains, seen in Fig. 4.18c), with sizes of about $\sim$30 nm judging from the 1 μm scale bar in the bottom right corner. Fig. 4.18b) shows the crater edge in the 1000C sample at the same magnification. In this sample grains are observed as well, and show sizes >100 nm. This further indicates what has been seen in SIMS, XRD, and RBS, where indications of new phases have been found. The different size observed in the two samples can either be due to Oswald ripening, i.e. bigger crystals grow at the expense of smaller crystals at higher temperature [88], or the phases in the two samples are different. The latter implies that the growth of the phase in the 800C sample is not the thermodynamically energetically favored at 1000C, and a new phase appears. Interestingly, there were no sign of foreign crystals at the shallow crater bottoms in Fig. 4.18a) and b), they were only visible in the crater edges.

One could speculate that this has to do with the crater sputtering process, or that crystals are present only on shallower depths than R_p. The latter is in conflict with the SIMS results, who show a matrix effect beyond R_p.

That said, the 1000C XRD result show a presence of Zn_2GeO_4, making this a likely candidate at least in this sample, if not both. The increased size in the 1000C sample is in good accordance with XRD and SIMS. It could explain why the 800C crystals are not visible by XRD, yet still show the matrix effect in the SIMS measurement. Because the implantation peak width is only ∼900nm, and as X-rays can probe several microns into the sample [89], it is possible that the smaller crystals diffraction was not intense enough to be detected. Further, the lack of crystallites at the shallow crater bottom could indicate a preferential sputtering of the phase assumed to be Zn_2GeO_4.

4.2.5 TEM results

Further structural investigation of the 800C and 1000C T1Ge samples were done with TEM. Fig. 4.19 shows a medium angle annular dark field (MAADF) STEM image of the cross section of the implanted volume in the 800C sample, taken with a JEOL-TEM at 100k magnification. In MAADF-images the dominant contrast is strain induced diffraction, meaning that the brighter areas indicate a larger strain. On top of this the Ge distribution inside the sample as measured with SIMS is plotted to scale. High amounts of strain can be seen from ∼350 nm

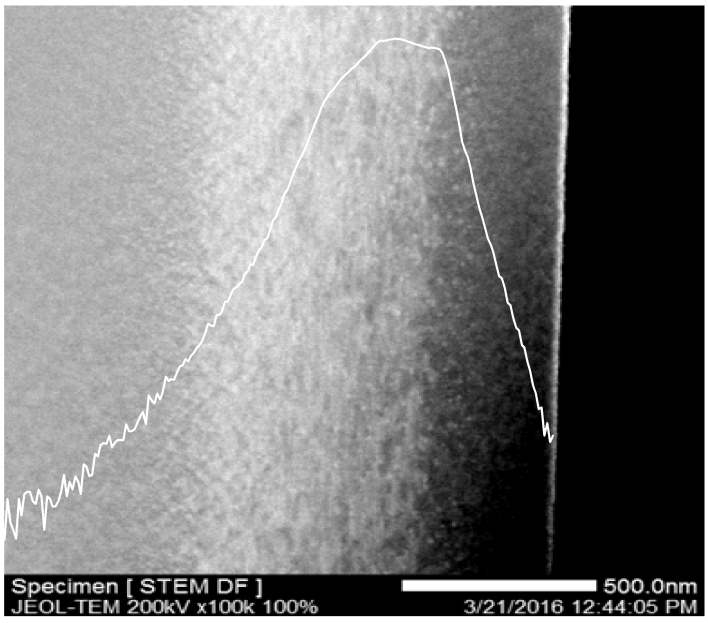

Figure 4.19: MAADF STEM picture of the 800C sample, with the sample edge on right side. The 800C SIMS profile is plotted to scale on top of the STEM image.

into the sample, which is slightly shallower than R_p, and it continues approximately 600-700 nm further into the sample. This is consistent with RBS measurements where a large lattice disorder is observed in the 800C sample. That the strain is located near the Ge concentration peak could further indicate that Ge as a dopant strains the lattice. Additionally, small circular areas of higher strain can be seen, and could indicate a new phase or precipitates, which would be consistent with the matrix effect observed with SIMS.

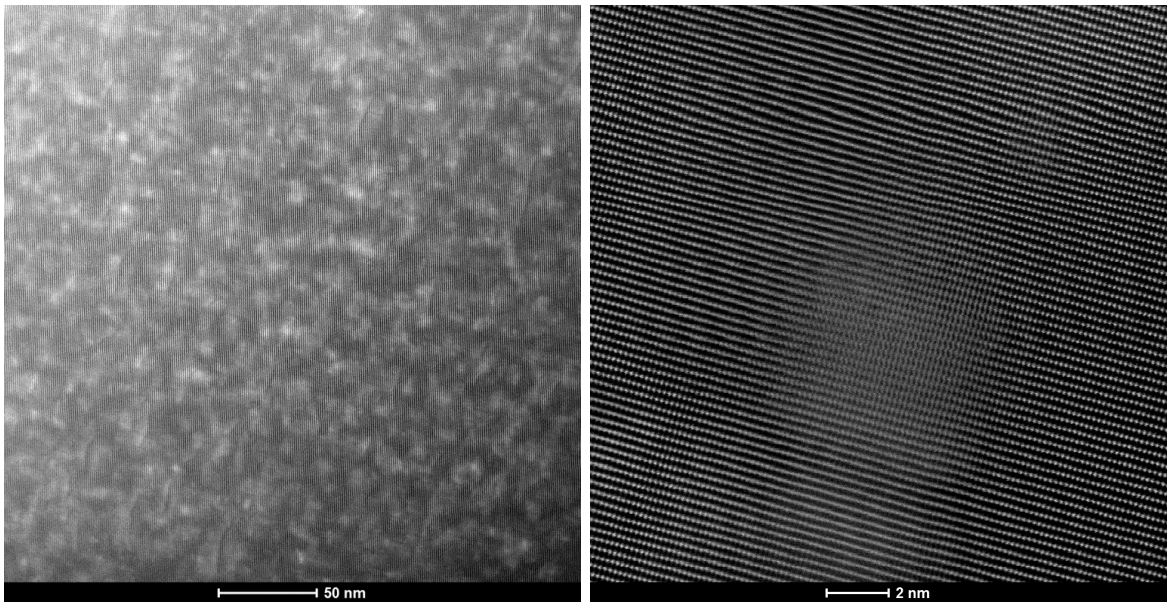

(a) (b)

Figure 4.20: HAADF STEM image of the sample, a) overviews the sample, and b) is zoomed in on one of the white areas seen in a).

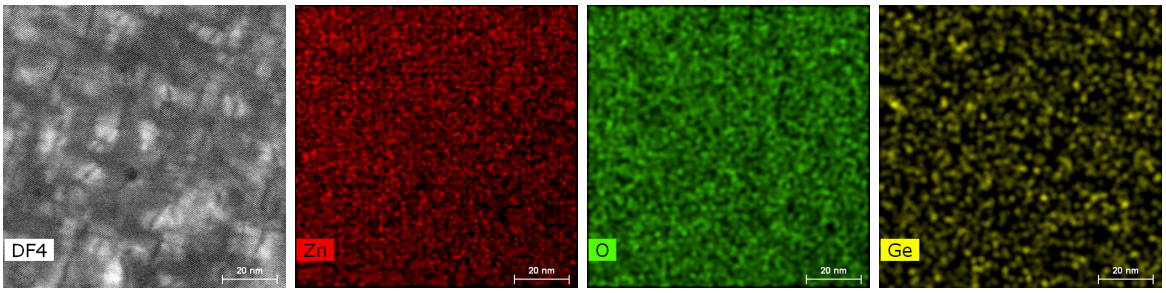

(a) TEM image (b) Zn signal (c) O signal (d) Ge signal

Figure 4.21: TEM EDS results of the 800C sample.

Fig. 4.20 shows high angle annular dark field (HAADF) STEM images of the 800C sample taken with the TITAN TEM at 300kV acceleration voltage, i.e. the contrast is mainly mass-thickness, and thus the brighter areas are of larger mass-density. Fig. 4.20a) shows the general strained area seen in Fig. 4.19 at a higher magnification. The large amounts of brighter areas indicate that there is a lot of areas with denser atomic packing, or heavier elements. Further analysis, Fig. 4.20b), shows one of the brighter areas in a) at even higher magnification, and a disruption, ∼4 nm wide, in the periodic ZnO lattice can be seen. EDS analysis of a similar area, shown in Fig. 4.21, in the same sample reveals no accumulation of Ge in this phase, indicating that it is not a Ge rich phase, e.g. a precipitation. It could, however, be the initial growth stage of another phase, as indicated by SEM.

The 1000C sample was investigated in a similar way, and Fig. 4.22 shows a MAADF STEM image taken by a JEOL-TEM at 200kV, with a magnification of 120k. The Ge concentration as measured by SIMS is plotted on top. The wide strained area observed for the 800C sample in

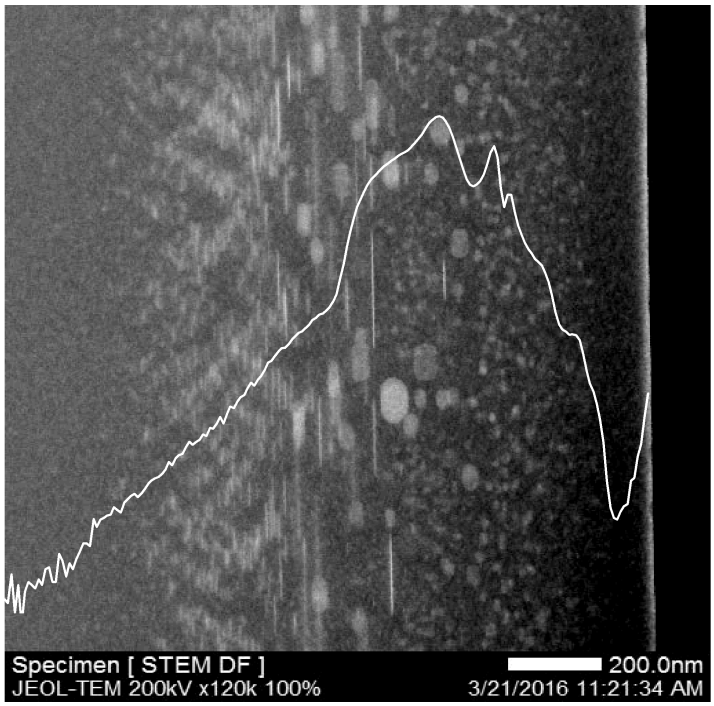

Figure 4.22: STEM HAADF picture of the sample, with the edge on right side. On top the 1000C SIMS profile is shown, to get a view on where there is most Ge.

Fig. 4.19 is to a large extent gone, replaced by separate spherical strained areas ranging from ∼5 to 100 nm in size. The small ones are at shallower depths than R_p, while the large ones are at R_p and slightly deeper. The general improvement of the ZnO lattice between the strained phases is consistent with RBS, where the 1000C sample shows a significant improvement from the 800C sample. Further the large phases are compliant with SEM, where Oswald ripening was indicated. The thin lines parallel with the sample surface behind the implantation peak indicate a high amount of extended defects at this depth. The peaks seen in the SIMS profile can to some extent be detected as well. Especially the reduced Ge concentration at ∼350-370 nm is visible as columns with reduced strain.

A closer look at some of the strained areas revealed dark spots in the HAADF STEM images seen Fig. 4.23. Fig. 4.23a) shows several of these darker areas at small scale, with distances 30-40 nm between them, while Fig. 4.23b) shows a high resolution image of a hexagonal darker area. In b) there is no sign of a uneven or mismatched lattice, and the dark color in mass-thickness contrast imply a lower density of material. This could indicate that the darker areas are in fact voids inside the material. The atoms seen inside the darker area could be from above or below the cavity. In addition, the shape of the assumed cavities are triangular and hexagonal. This is consistent with findings done by Chan et al. [90]. They implanted ZnO with a high dose of H, and saw cavities emerging after annealing at 800°C and 950°C for an hour. The concentration was highest around R_p as well. The cavities were related to implantation damage, and this was related to the stability of different directional surfaces in ZnO. Calculations by Bang et al. [91] proposed the cavities formed due to clustering of V_{Zn} - V_O vacancy pairs, with further growth due to attraction of mono vacancies. Similar results were shown by Marstein et al. [92] after a high dose Ge implantation in SiO_2, with spherical

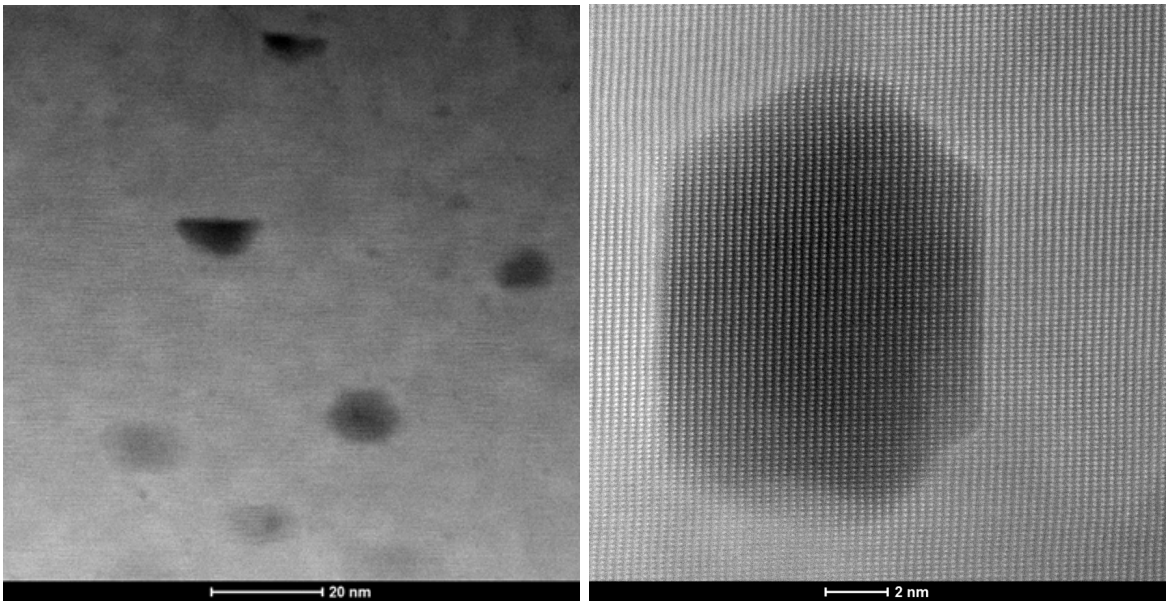

(a) STEM image overview (b) Zoomed in on a black dot

Figure 4.23: STEM HAADF image of the sample, a) overviews the sample, and b) is zoomed in on one of the dots visible.

voids observed after annealing at 1000°C.

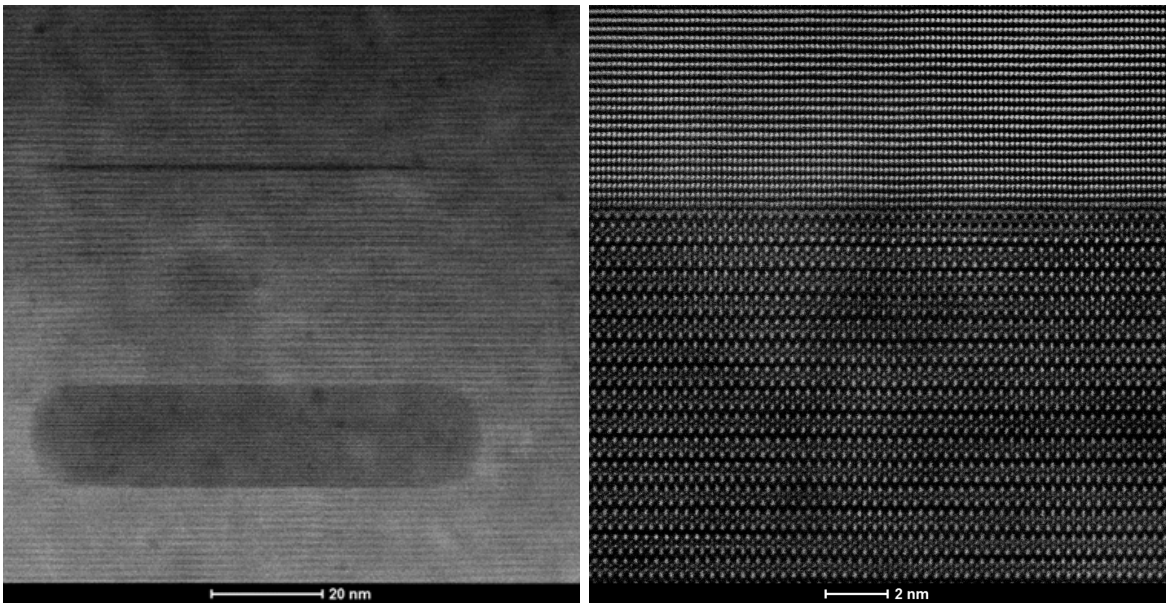

(a) STEM image of the rod shaped phase (b) Zoomed in on the rod shaped phase

Figure 4.24: STEM HAADF image of the rod shaped phase present in the 1000C sample. a) Shows the whole structure, while b) shows a higher magnification of the structure and the phase transition.

In addition to cavities, rod like shapes were observed, and is shown in Fig. 4.24. a) shows

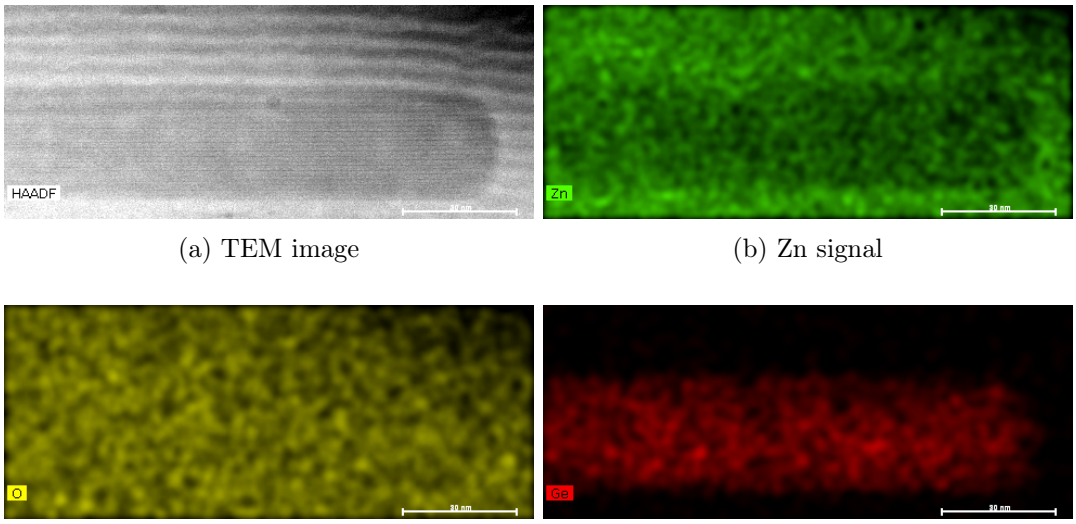

(a) TEM image (b) Zn signal

(c) O signal (d) Ge signal

Figure 4.25: TEM EDS results in the rod shapes.

the whole rod, while b) has zoomed in to get a better view of the crystal structure. Lengthwise the rod is close to 150 nm, with a width of ∼35 nm. Judging the crystal structure shown in b) this might be the Zn_2GeO_4-phase seen in XRD. It would imply that its c-axis goes to the left in the image. The phase transition seems to be close to epitaxial quality, with very little interface defects. The phase identity is backed up by Fig. 4.25, showing an EDS analysis done on the rod. It has a weaker Zn signal from the rod than the ZnO structure around, but the O signal is unchanged. Ge on the other hand is located within the rod, and not observed in the ZnO lattice around. The reduction in Zn signal is probably due to change in the Zn density in the Zn_2GeO_4 phase, compared to ZnO. Further, additional EDS analysis over a wider area showed that the Ge had a tendency to cluster, at least in the 1000C sample(Fig. C.1 in appendix C).

EELS analysis of the T1Ge were carried out at a low acceleration voltage of 60 kV, to get a higher energy resolution than the 300 kV beam. Fig. 4.26a-c) shows the result of the EELS analysis of the 800C T1Ge sample, while d) show plasmon energies measured inside and outside a similar particle. The probed area is sown by a MAADF image in Fig. 4.26a), the resulting spectra in b), and a mapping of intensities from 4.9-5.4 eV in c). Beginning with a), the EELS analysis is done around a brighter particle of size ∼10 nm. The EELS spectra in b) is measured outside the bright particle. Here band gaps of 3.3 eV and 5.06 eV are observed, respectively. The same measurement done inside the particle resulted in only one observed band gap of 3.29 eV. The mapping done in Fig. 4.26c) illustrates this, by showing areas transmitting the most 4.9-5.4 eV electrons of the area inside the green square in a). The red areas indicate high intensity, and blue areas indicate low intensity. Low intensity in the 4.9-5.4 eV range is observed inside, but much more is visible around the particle. If the 3.3 eV signal is from ZnO, while the 5.06 eV signal is from Zn_2GeO_4, this indicates that the particle is not composed of the Zn_2GeO_4 phase, but that the surrounding region may contain Zn_2GeO_4. This could be further substantiated by the change in plasmon energy observed in- and outside the particle shown in Fig. 4.26c). Experimental values for Ge nanoparticles made by the evaporation method, presented by Yamada [93], show a plasmon energy of ∼16.4 eV for

a nanparticle diameter of 12 nm. Nanoparticles observed in this thesis has a size of ∼10 nm, which in accordance with theory presented by Yamada, should give a slightly larger energy. This is consistent with the measured plasmon energy of ∼16.7 eV in the T1Ge 800C sample.

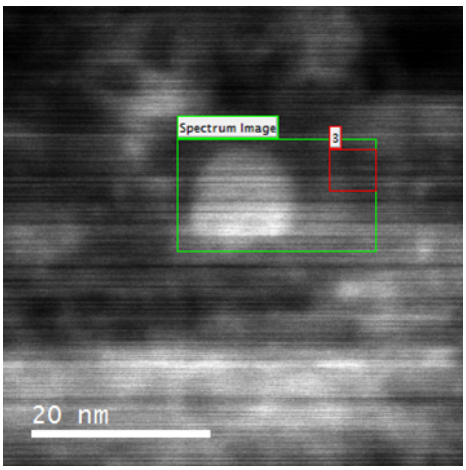

(a) MAADF image of scanned area

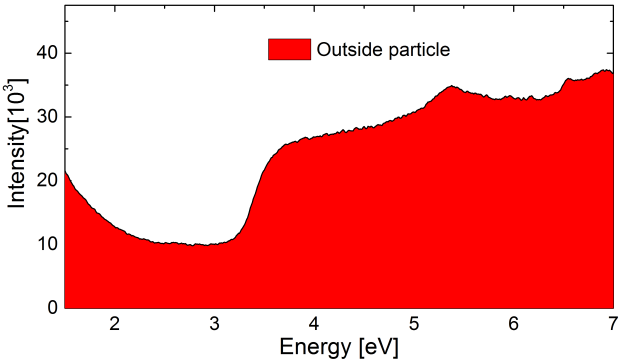

(b) EELS spectra of outside the particle

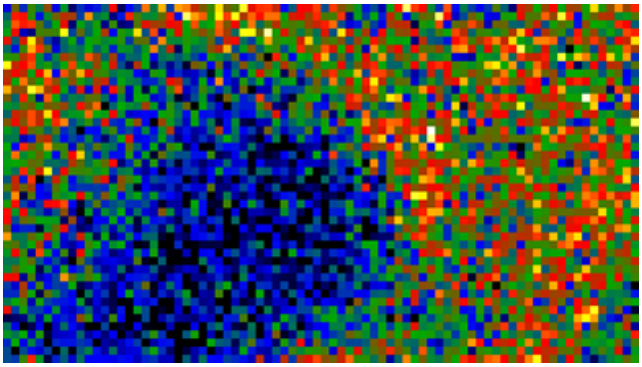

(c) Mapping of 4.9-5.4 eV intensity

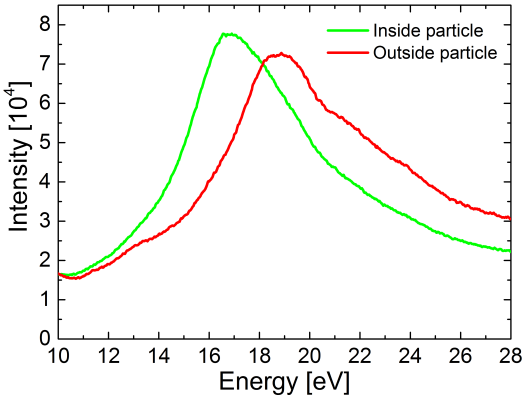

(d) Plasmon peaks

Figure 4.26: TEM EELS results in the 800C sample

Further investigation done on a similar particle in the same sample using EDS, Fig. 4.27, show a significant depletion of Zn and O, and a strong accumulation of Ge in the particle. This is different from the results gathered from the rod in the 1000C sample shown in Fig. 4.25, where EDS showed a clear Zn depletion, and no O depletion, in addition to Ge accumulation, and thought to be Zn_2GeO_4. This further substantiates that the observed particles in the 800C sample is a new phase, including high Ge concentrations. Similar EELS measurements, done on the 1000C T1Ge sample, is shown in Fig. 4.28. a) shows the scanned areas, where one is inside a rod shaped structure and the second is not, while b) shows the plotted results both inside and outside the rod. The rod shapes inside are very similar to the rods observed at higher acceleration voltage, and is assumed to be the same phase. Looking at the EELS spectra in b), the red area is from measurements outside the rod, while the green is from inside. An extra band gap is observed at ∼3.26 eV outside the rod, while inside an additional band gap at 5.04 eV is seen. This is in accordance with the observed band gaps for the 800C

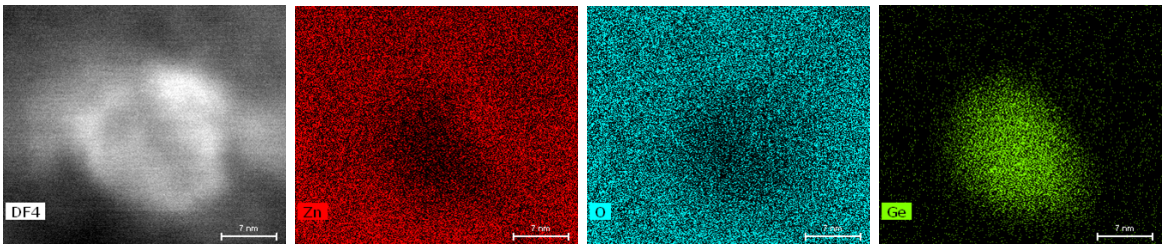

(a) TEM image (b) Zn signal (c) O signal (d) Ge signal

Figure 4.27: TEM EDS results of the 800C sample at acceleration voltage of 60 kV.

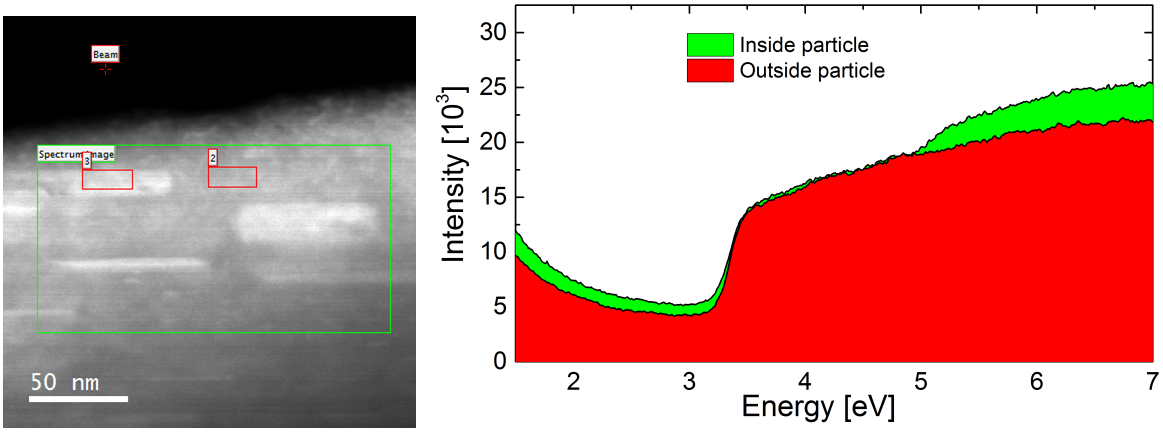

(a) Scanned area (b) EELS spectra

Figure 4.28: EELS measurements on the 1000C T1Ge sample.

sample, and substantiates that the second phase observed at 5.04 eV is in fact Zn_2GeO_4.

4.2.6 SSRM results

To measure the conductivity of the samples as a function of depth scanning spreading resistance microscopy was applied to the T1Ge series, measuring the cross section of the sample. Fig. 4.29 shows the average resistance scanned over a square area of 3×3 μm. The sample edge (the implanted surface) is near the left side in each plot. The tip scanned close to but not over the edge, resulting in an uncertainty in the depth profile of ∼100-200 nm.

All samples show a lower resistance in the vicinity of R_p. The as-implanted sample shows the largest general resistance, but even without annealing it is reduced substantially relative to the bulk. This could be due to both implantation damage giving an average n-type material, and the Ge dopants being activated at room temperature. In the 600C sample, it is a much more pronounced resistance reduction than in the rest of the samples at R_p, and high resistance beyond. This is in compliance with the SIMS measurement, where there still is a high amount of Li behind R_p. Further the 800C sample has a low resistance around R_p, and it stays low beyond. This is also consistent with SIMS measurements, where the Li is depleted beyond R_p. Further aiding the small difference between bulk and R_p could be the creation of the new phase shown in SEM measurements. This will probably reduce the Ge dopant effect, and thus consume some of the dopant concentration. The 1000C shows a similar resistance

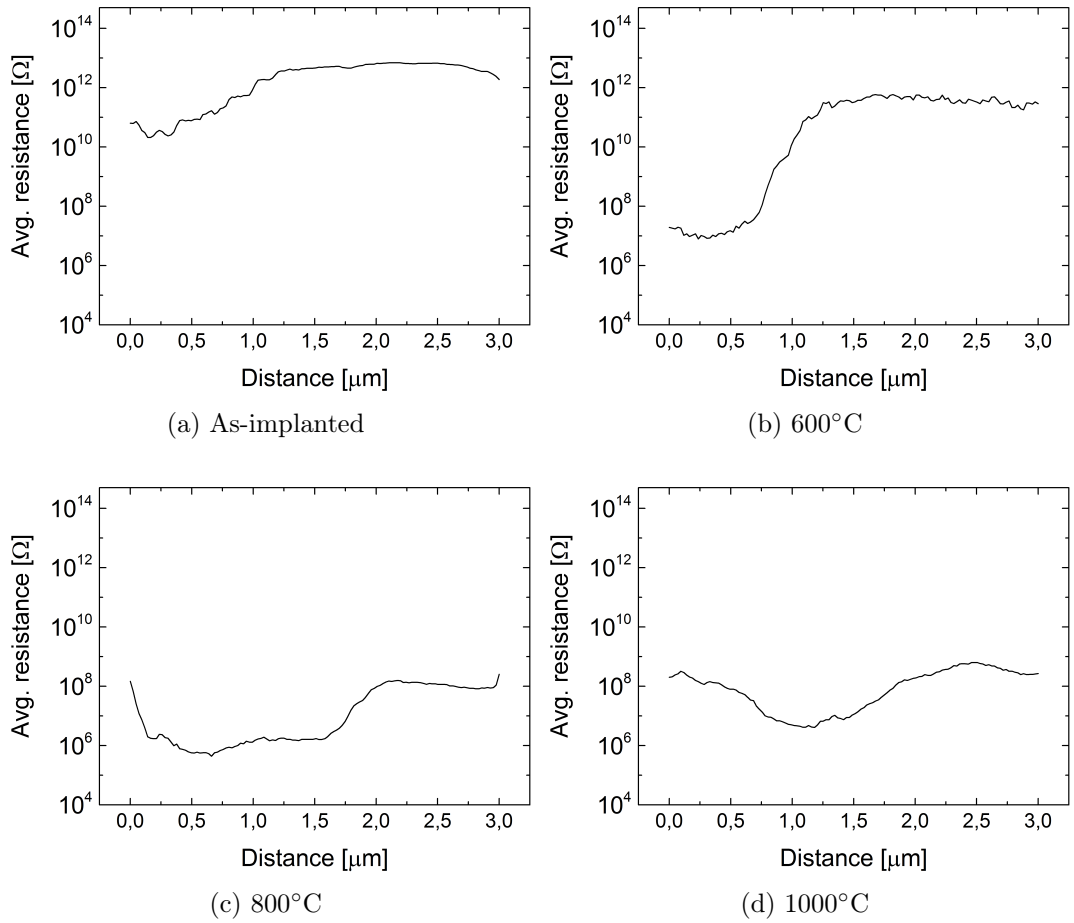

(a) As-implanted (b) 600°C

(c) 800°C (d) 1000°C

Figure 4.29: SSRM average resistances from all samples in T1Ge, gathered from scanning a quadratic area of the cross section of the sample.

as the 800C. A reduction occurs near R_p, but the resistance does not increase as much as for the as-implanted and 600C samples, which both have slightly lower Li concentrations. In Fig. 4.22 high amounts of strain can be seen in what is assumed to be extended defects behind R_p. Here there could be several defect complexes present, decreasing resistivity.

4.2.7 Hall effect measurement results

The resistivity, carrier concentration, and mobility was studied using TDH measurements. Similar to that of the Si implanted samples, the measured Hall resistance will be a combination of the implanted region and the bulk ZnO, and the 1 μm approximation[2] is applied for this series as well.

The measurement results showing the resistivity, carrier concentration, and mobility can be seen in Fig. 4.30 a), b), and c), respectively. The as-implanted and 600C samples show a close to degenerated behavior for resistivity, carrier concentration, and mobility, i.e. neither is dependent on temperature, and remain unchanged. This is caused by a large amount of shallow donors, making the temperature range too small for freeze out. A carrier concentration

[2]The 1 μm approximation is explained in section 4.1.5.

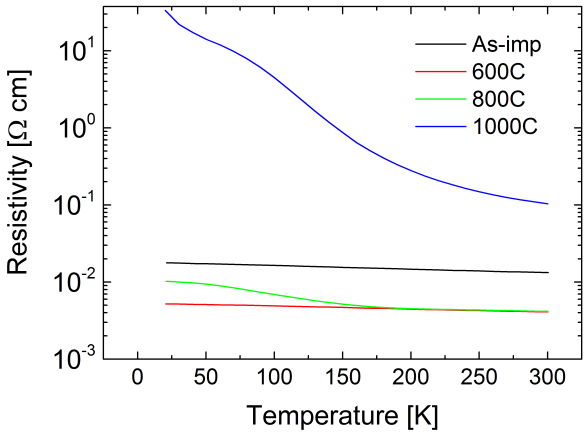

(a) Resistivity

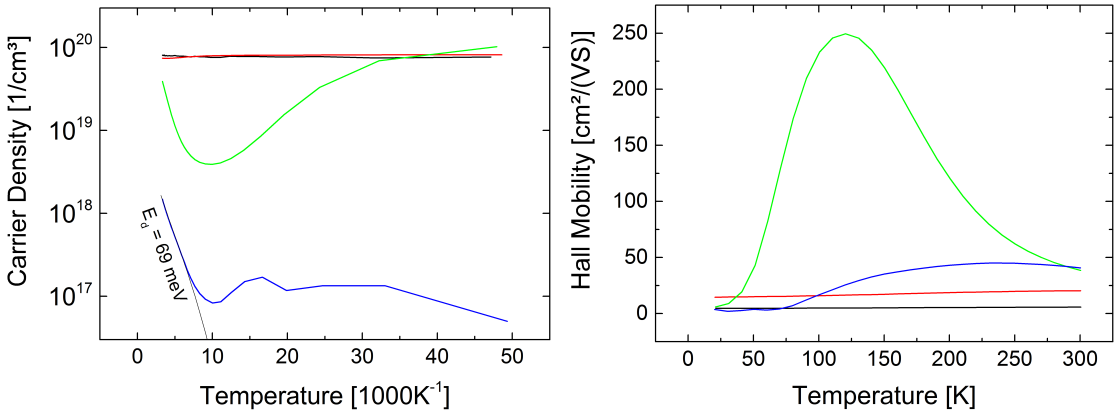

(b) Carrier concentration

(c) Mobility

Figure 4.30: T1Ge TDH measurement results.

of $\sim 7.6 \times 10^{19}$ cm^{-3} in both these samples can only be caused by the implanted region, since the carrier concentration of high resistive Tokyo Denpa samples is too low. This is consistent with SSRM measurements, and substantiates that Ge is activated as a donor already at room temperature. The low and degenerated mobility in both samples indicate high amounts of implantation damage. The mobility is however, increased from 5 cm^2/Vs in the as-implanted sample at 300K to 20 cm^2/Vs in the 600C sample, indicating that the lattice disorder has decreased slightly during 60 minutes at 600°C. This is further reflected in the decreased resistivity of $\sim 4.2 \times 10^{-3}$ Ω-cm as compared to the as-implanted samples $\sim 1.3 \times 10^{-2}$ Ω-cm. The 800C sample shows a resistivity close to equal of the 600C sample at room temperature, but it is reduced slightly at lower temperatures. The carrier concentration is reduced considerably with temperature, from $\sim 3.2 \times 10^{19}$ cm^{-3} at 300K to $\sim 3.9 \times 10^{18}$ cm^{-3} at 100K. But as temperature is decreased further it begins to increase, and ends up at $\sim 1 \times 10^{20}$ cm^{-3} at 20 K. This is assumed to be due to surface currents, as observed in the Si implanted samples as well, and a more thorough explanation is given in the TDH part of section 4.1.5. In addition a high peak mobility value of $\sim$250 cm^2/Vs is observed in the 800C sample. This is close to bulk numbers, and is thus in conflict with RBS measurements. The 1000C sample shows a

higher resistivity more dependent on temperature than the three former samples. This is due to the carrier concentration being lower, $\sim 1.5 \times 10^{18}$ cm^{-3} at room temperature, and that the measurements seem to be less affected by surface currents. A low peak mobility value of ∼45 cm^2/Vs is observed, indicating that the 800C value might be too high for the current only to probe the implanted layer.

Calculations of the energy level was done for the 1000C sample, in a similar fashion as in section 4.1.5 since this exhibited the less surface currents than the 800C sample, and the as-implanted and 600C samples are degenerated. The donor level energy is calculated to be 69 meV. This could be related to In (63 meV) [86], or it could be related to Ge as a dopant.

4.2.8 PL results

The samples were further characterized by PL. Measurements were done at 10 K. In order to obtain depth information from the samples, the measurements were done inside sputtered craters with predefined depth. The primary beam of a Cameca 7F SIMS instrument was utilized to make the craters in which PL could be preformed, one deep, well beyond R_p and one shallow, at $\sim R_p$. The deep crater (Fig. 4.31c) and d)) mainly reflects the bulk ZnO spectra, while the shallow (Fig. 4.31a) and b)) investigates properties unique to the implanted region depth. Fig. 4.31 a) and c) show the entire measured spectra with wavelengths from 350-810 nm, while b) and d) show a more detailed look at the near band edge emission (NBE) (∼350-450 nm), showing wavelengths from 350-490 nm.

In both craters there is a clear evolution with increased annealing temperature, where deep level emission (DLE) (∼450-800 nm) generally increase with annealing temperature. In the shallow crater in Fig. 4.31a) and b) the luminescence signal is low, probably due to light trapping from the ion induced defects, generating mostly a low output intensity. Some of this is still present in the 600C sample, but a deep level band grows visible from ∼550-750 nm, a small peak at ∼490 nm, and a wide NBE peak, probably originating from several recombination paths, is visible around the band gap energy of ZnO (∼365-450 nm). The 800C sample is similar to the 600C, but with increased intensity over the whole spectrum. The deep level band is broadened, and seems to contain contributions from beyond 700 nm. At 490 nm the small peak visible in 600C has grown, and the NBE emission has increased significantly as well. In the 1000C sample similar features appear, but it seems that the 490 nm emission has become dominant, increasing by about two orders of magnitude from the 800C sample, and it has red shifted with 10-20 nm. This peak has been observed in ZnO for decades, and is often related to Cu in the material [94, 95]. In addition the tails in the NBE emission has become shorter, with a more irregular pattern, indicating more discrete transitions, and thus more ordered material. A comparison of the NBE emission for all annealed samples show that the 600C and 800C is blue shifted with respect to the 1000C peak. This indicate substantial doping of ZnO in these samples, causing the so called Burstein-Moss shift, effectively increasing band gap size by pinning the Fermi level in the conduction band. Alternatively it could be emission from a phase with a wider band gap than ZnO, like deep defect states from the suggested Zn_2GeO_4, that continue beyond the detector range. The deep cater measurements (Fig. 4.31c) and d)) show similar trends, but the spectra are still significantly different. The NBE emission of the as-implanted and 600C samples are close to non-existent, but both show a wide deep level emission, with contributions from beyond 700-800 nm. The 800C sample is closely related, with an order of magnitude increase in the deep level emission, and the presence of a small series NBE emission peaks, seemingly matching the ones in the 1000C

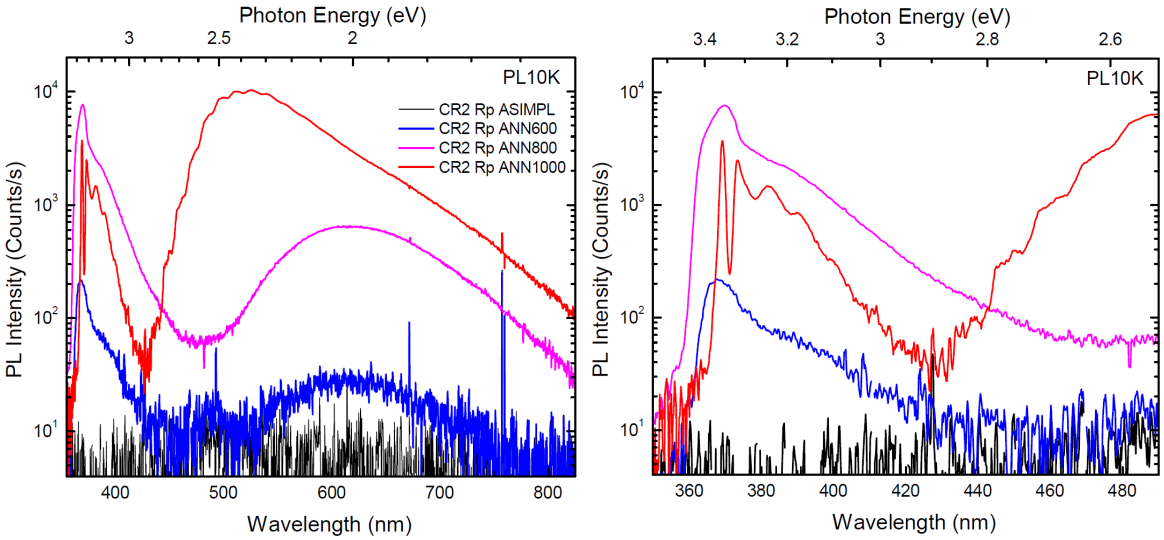

(a) Shallow crater emission

(b) Shallow crater NBE

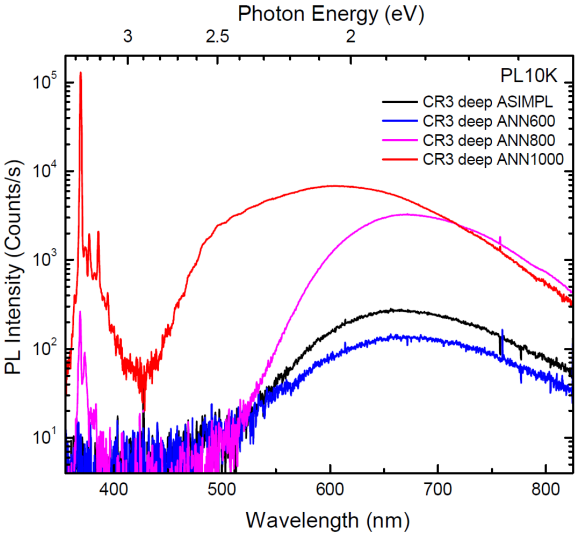

(c) Deep crater emission

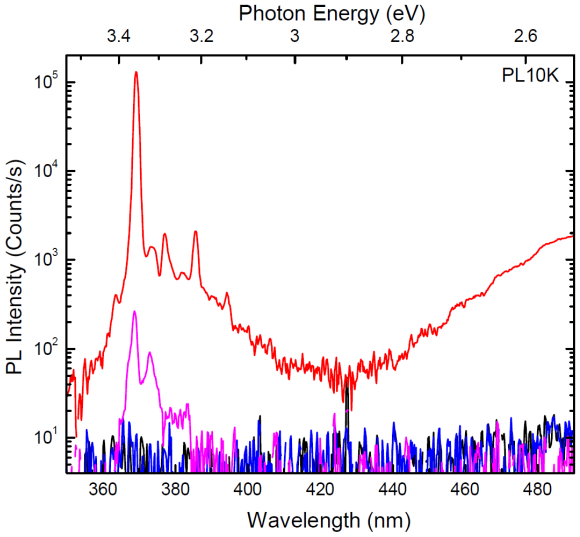

(d) Deep crater NBE

Figure 4.31: T1Ge PL results at 10 K.

samples shallow crater. In addition the 490 nm emission is gone in all samples except 1000C, witch has a pronounced 490 nm emission, broadening the deep level band quite significantly. The NBE emission has a smaller tail than in the shallow crater, and is sharper in general.

4.2.9 Spectrophotometer results

The transparency of the tin films in T2Ge samples was measured using a spectrophotometer. This was done to see if there were any indications of phases with a smaller band gap than ZnO. They would be identified with a reduced transmission at the wavelength corresponding to the new phase band gap energy. The results are shown in Fig. 4.32. 4.32a) shows the whole spectrum from 290-2500nm (∼0.5 eV - 6.2 eV), while b) shows a more detailed view

at the transmission between 340 and 405 nm. Noise at ∼800 - 1000 nm is related to change of detector during measurement, and nothing physical in the sample. Generally the films show the same behavior, except the as-implanted film, which show a reduced transmission from ∼900-2500 nm. This is related to high carrier concentrations [96], and caused by the materials high electron plasma frequency. This frequency is an increasing function of the carrier concentration, and all radiation with frequencies lower than the plasma frequency is reflected. Meaning that this indicates a high amount of carriers in the as-implanted film. Fluctuations in the transmittance can be seen as well. These are due to constructive and destructive interference of reflected light from the film-substrate interface and the film-air interface. So at certain wavelengths the light reflected from the substrate-film interface will interfere destructively with waves reflected from the film-air interface, and lead to an increase in transmitted intensity. The opposite happens when the reflected light at both interfaces positively interfere, and increases reflection. The same seems to happen in the 1000C sample, but to a much lower extent.

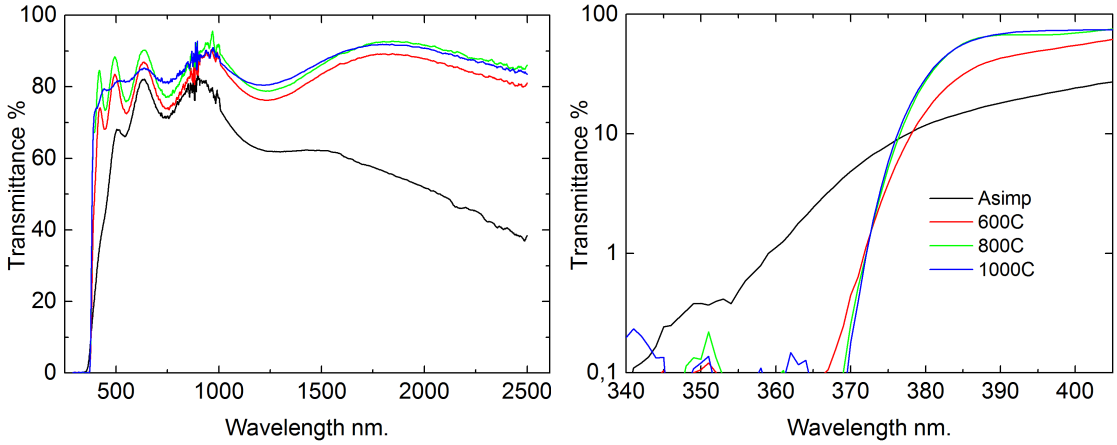

(a) Spectra between 290 - 2500 nm

(b) Cutout at 350 - 400 nm

Figure 4.32: T3Ge spectrophotometer results.

Further a Burstein-Moss blue shift is observed in the as-implanted sample.This means the material is degenerate. It can be seen in the 600C and somewhat in the 800C sample, but much less pronounced. This means that the 1000C sample is expected to have the lowest carrier concentration, which is consistent with TDH and PL measurements done on the bulk samples. It could also possibly be related to the film quality, where high defect concentrations could induce, to some extent, the same pinning effect. There is no obvious evidence for reduced transmission due to band gap absorption in any of the samples.

4.2.10 Ge as a dopant in ZnO - some aspects

Ge as a dopant in ZnO is similar to Si, but the increased amount of disorder indicates that it is less suitable, i.e. a poor lattice fit, and that implantation produces more compensating defects, extended defects, and precipitates. The precipitation at higher annealing temperatures, especially 1000°C, leads to a decrease in carrier concentration and resistivity shown by TDH measurements. This is consistent with PL and to some extent transmission measurements, where a Burstein-Moss blue shift occurs for the lower temperature samples, but is

not present in the 1000°C annealed sample. The 1 μm approximation seems to be valid for the as-implanted and 600C sample, but the higher temperature samples, especially the 800C sample, seems to be probed in a larger volume. This is indicated by the small difference in resistivity between the implanted layer, and the volume below, as shown by SSRM, and the high carrier mobility shown in the 800C and partly the 1000C sample.

A large amount of lattice disorder is indicated by RBS, for all the T1Ge samples. In the 1000°C sample the amount of measured RBS yield is close to that of the as-implanted Si samples at greater depth. This is observed by TEM as well, where a large amount of near continuous strain is observed around R_p in the 800C sample. The 1000C sample show well-defined separated strained areas near R_p, and what seems to be a large concentration of extended 2D defects beyond. This could be a possible contribution to the low resistivity seen in the 1000C sample, despite high Li concentration, and possible reduction of Ge donors due to clustering, after annealing at 1000°C, the sample still shows a wide area of low resistance in SSRM. The resistivity measured with TDH is to some extent in conflict with the SSRM measurement, because here the 1000C sample by far has the highest resistivity and lowest carrier concentration, which is supported by the PL and large amount germanium cluster-phases found in the sample using TEM. In addition the buildup of Li near R_p is expected to increase the resistivity in this region.

4.2.11 Ge related precipitation and embedded nanostructures in ZnO by ion implantation

Annealing temperatures at 800 and 1000°C caused the implanted Ge distribution to change significantly, and precipitations and new phases emerge, which is very different to the observed behavior of Si. This indicates that Ge is more suited for nanostructuring. Nanocrystalline phases have been observed after heat treatment at 800 and 1000°C using TEM. In the 800°C treated sample indications of a $\sim$ 10 nm sized Ge phase has been observed inside a surrounding Zn_2GeO_4 layer using EELS and EDS. The nanocrystalline phases are not observed by XRD, but supported by SIMS measurements where a substantially higher ionization efficiency is observed, as expected from a different phase. Further observation of a red shift in the plasmon energy, matching observed and calculated plasmon energies for Ge nanoparticles [93]. The decrease in plasmon energy can not be related to the Zn_2GeO_4, since decrease in size should increase the Zn_2GeO_4 plasmon energy inside the particle, compared to larger structures around the particle. The 1000C sample showed indications of a present $(11\bar{2}0)$ oriented Zn_2GeO_4 phase using XRD. Further investigation with TEM revealed rod structures of Zn_2GeO_4, $\sim$20 nm wide and $\sim$100 nm long, which were further substantiated using EELS. The growth of the Zn_2GeO_4 rods seem to be very controlled, and interfaces between the crystallites looks very close to epitaxial, with very little defects.

Images produced of the 800C and 1000C samples using SEM shows significantly larger particles than what is observed using TEM. This could be because the particles are enveloped by strained volumes, of either Zn_2GeO_4 or ZnO, making it possible to distinguish them. It is however, important to note that all particles were sputtered away from the crater, only surviving in the crater edges, where there is less sputtering. This could indicate that there is a potential preferential sputtering of the phases. In addition this reduces the chance of finding particles with PL in the 800C and 1000C samples. With crystallites only in the sample edge the measured signal will most likely be scarce. This would thus reduce the probability of the ZnO band gap blue shift being because of deep Ge precipitate energy levels.

Chapter 5

Summary and Conclusion

In conclusion Si is a promising candidate for n-type doping in ZnO, particularly suitable for implantation processing, due to the strong defect annihilation and promising donor qualities. The samples show a substantial decrease in measured resistivity after implantation using RTH, and annealing at 800°C gives a near virgin ZnO crystal quality as observed by RBS. After annealing at higher temperatures a buildup of Li (naturally occurring in HT grown Tokyo Denpa ZnO) in the implanted region is observed by SIMS, and the resistivity is shown to increase in the same area by SSRM. TDH measurements were done on both Si implanted ZnO and Zn implanted ZnO, but due to low resistive samples the current was indicated to probe more than the implanted layer, due to large mobilities. This was further substantiated by calculations of the dominating donor energy level, which was attributed to either Al (52 eV) or Ga (55 eV) which are common background n-dopants in ZnO.

Ge shows similar doping capabilities as Si, but the high amount of extended and compensating defects related to the implantation, and precipitation of new phases after annealing at higher temperature, makes it less suitable as a dopant introduced by implantation processing. Ge does, however, show great promise in nanostructuring and additional phases are observed after annealing temperatures of 800°C. Ge implanted material RBS shows a high amount of defects in the material, and TEM observes high amounts of extended defects, even after 1000°C annealing. Degenerated behavior of resistivity is measured for as-implanted and 600°C annealed samples using TDH, and lower resistivity is observed in the implanted region by SSRM. For samples annealed at 800°C and 1000°C the carrier concentration is reduced, which is suggested to be related to precipitation of phases containing Ge. This is supported by PL measurements, where a Bursein-Moss blue shift is indicated for low temperature samples, but disappears in samples annealed at 1000°C.

Closer study of the precipitates indicate a Ge phase surrounded by Zn_2GeO_4 using EELS and EDS in TEM, after annealing at 800°C. Further indications that Ge nanoparticles are present is given by measurements of plasmon energy inside the particle, compared to outside. The plasmon energy is lowered inside the particle, compared to outside, and the energy inside matches energies calculated and reported by Yamada [93]. The Ge precipitates are likely oxidized to Zn_2GeO_4 during annealing, which would explain the Zn_2GeO_4 surrounding the Ge particles in the 800C sample, due to that after annealing at 1000°C, XRD indicates a significant increase of Zn_2GeO_4, which is further substantiated by EELS and EDS in TEM. The Zn_2GeO_4 phases are crystallized as both spherical particles and rods.

5.1 Suggestions for further work

While implantation of ZnO by Si has shown a increase in carrier concentration, no dopant energy level related to Si has been extracted here. An alternative technique for this would be implantation into high quality thin films, using a isolating substrate. This would make it easier to probe only the active implanted region using electrical measurements like TDH, and thus acquire more accurate results. A wider box-implant here would further widen the doped layer, and hot implantation in combination with RT implantation of similar samples would give a better understanding of defects related to implantation in ZnO and the effect on resistivity, by using TDH ans SSRM measurements. Studies of the amount of defect annihilation, using e.g. RBS and PL, in thin films with increased annealing temperature could increase the understanding of the effect of donor- and acceptor defects related to implantation, and thus take steps towards use of Si implantation in fabrication of e.g. transparent thin film transistors. Thin films often contain a higher amount of grain boundaries than bulk samples. The effect these grain boundaries on the good implantation damage annihilation would be interesting, and relevant for future application. Transmission measurements of implanted Si would give further insight regarding the effect of Si implantation and doping on the transmittance of films. Additionally more research on the mechanisms involving the Li buildup, and possible complex formation, near R_p in samples annealed at higher temperatures could be done using SIMS and deep level transient spectroscopy (DLTS).

Further work on the donor properties of Ge implanted in to ZnO could effectively be studied using the techniques and methodology mentioned above, and since Ge introduces larger concentrations of defects than Si, hot and shallow box implantations could be especially interesting for this system. Smaller implantation doses would decrease Ge concentrations and thus likely make it easier to observe electrical properties of Ge, due to less precipitation and formation of new phases, or to monitor the stability of Ge as a donor at high annealing temperatures.

The observed precipitations of Ge and Zn_2GeO_4 should be further researched using small annealing steps in the temperature range from 600-800°C and monitor the the precipitation of Ge and subsequent oxidation with e.g. TEM, the goal of being able to control growth of both observed phases. Further absorption and emission experiments could monitor band gaps, recombination times, and MEG effects in Ge of precipitate sizes. Additionally the Zn_2GeO_4 phase properties in ZnO is an area where limited work have been published, and with relatively unknown applications, making it an interesting material for all types of characterization. Investigating of higher band gap phases like Zn_2GeO_4 increased range into the UV-region of the electromagnetic spectrum is paramount, and wider PL spectra should be measured. Confocal PL could give a spatial mapping of emission, and thus be very useful as well. Shallower implantation box profiles would be beneficial for most of these characterization methods. Lastly, the effect of lower than bulk quality ZnO on the Ge precipitation should be studied. Lower quality material could mean precipitations in grain boundaries or defect complexes that could alter the results observed in bulk ZnO.

Appendices

Appendix A

Si samples Li depletion

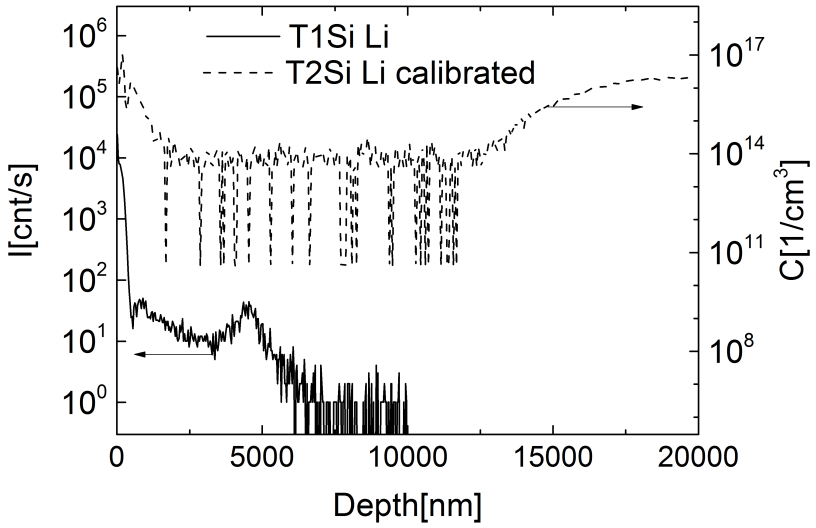

Figure A.1: The measured extent of the Li depletion observed in the T1Si 800C and T2Si 700C samples.

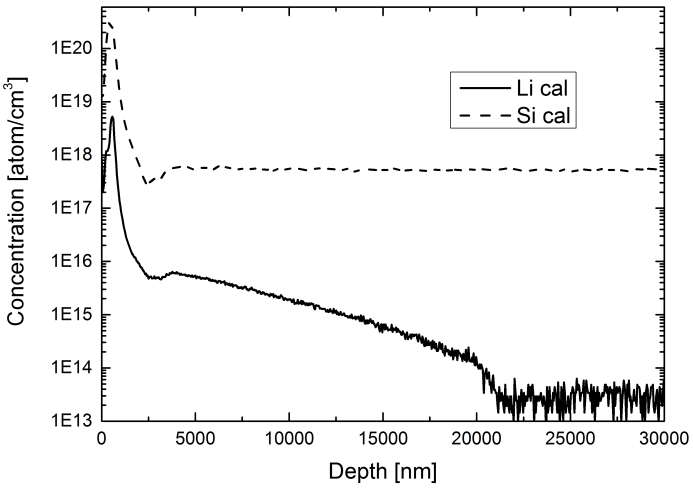

Figure A.2: The T4Si Li and Si concentrations plotted as a function of large depths. The Li and Si profiles can be seen to be similar for approximately 3.5 nm, where Li is reduced with increased depth and Si is constant. The reason for the shape of the Li reduction has not been studied.

Appendix B

SEM images not included in Results

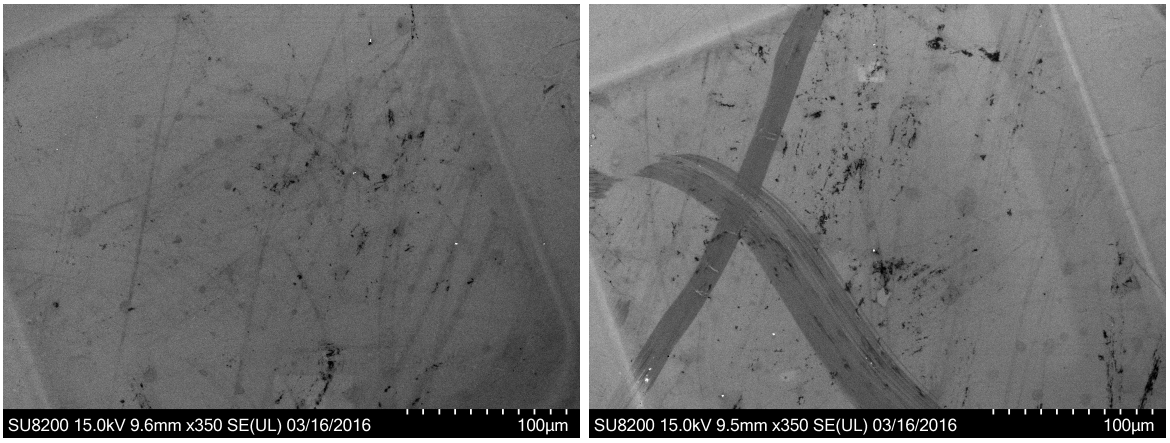

(a) Shallow (b) Deep

Figure B.1: The shallow (a) and the deep (b) craters imaged by SEM at a magnification of 350.

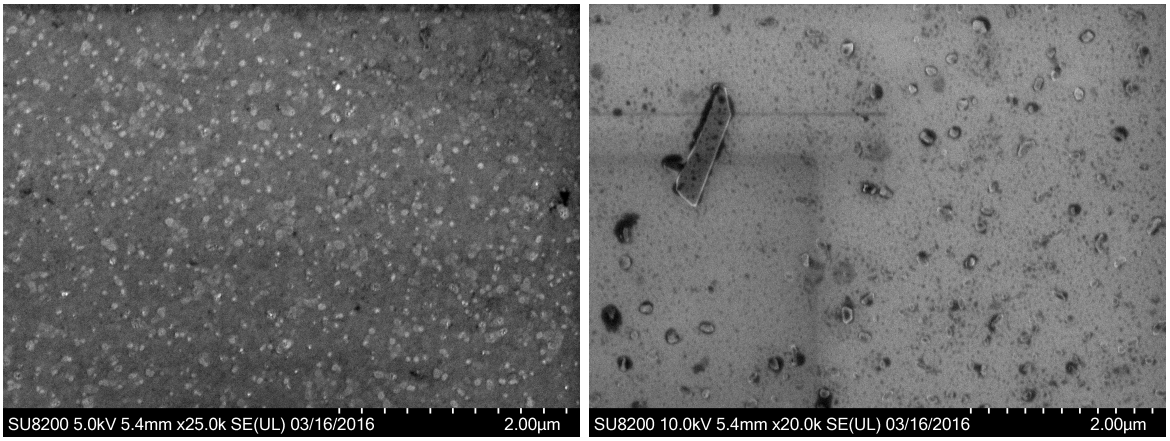

(a) 800°C (b) 800°C

Figure B.2: The surface of the 800C (a) and 1000C (b) sample imaged by SEM at a magnification of 25k and 20k, respectively.

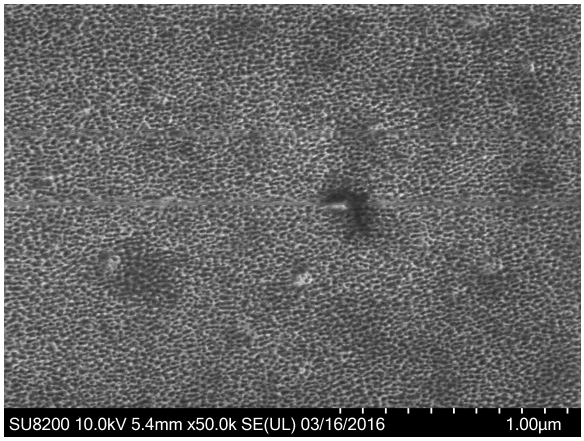

(a)

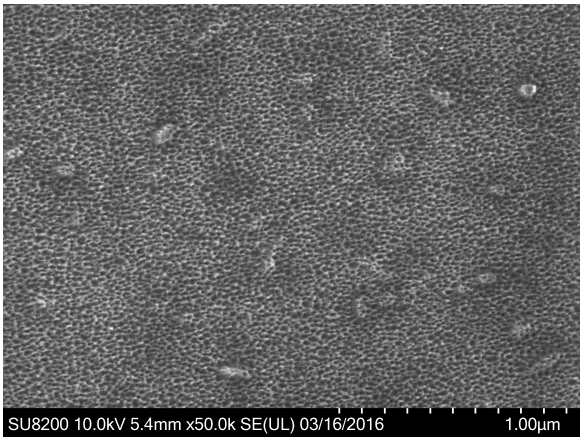

(b)

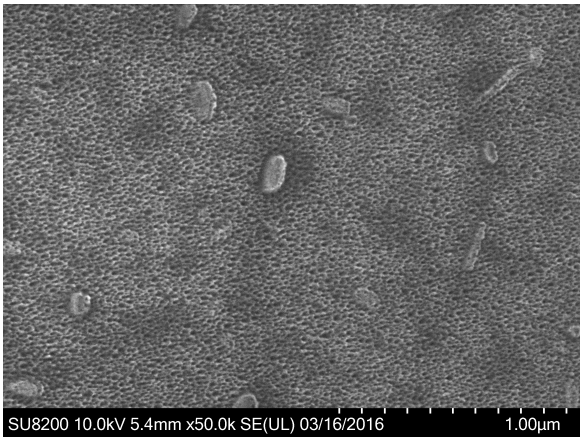

(c)

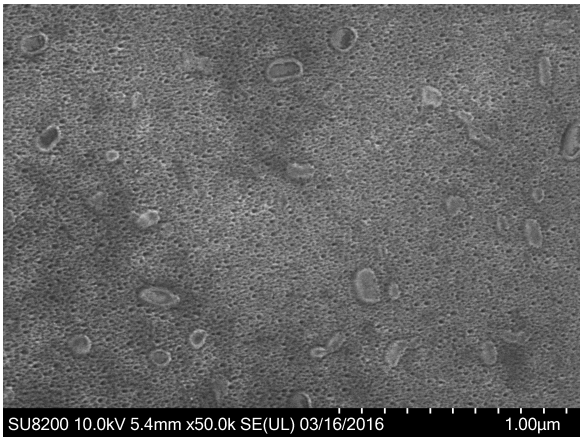

(d)

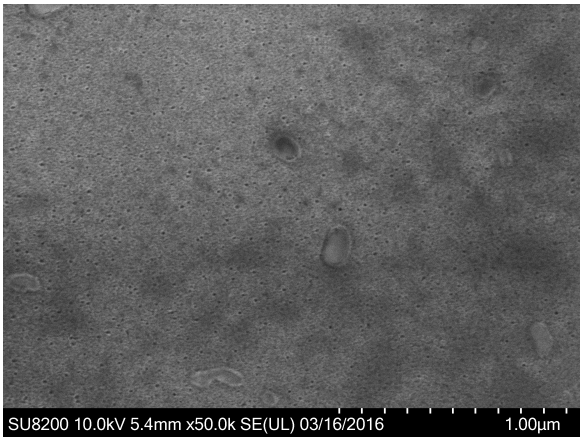

(e)

Figure B.3: T1Ge SEM images in the crater edge of the 1000C sample at a magnification of 50k. a) to e) show the crater edge from deeper (a) and almost to outside the crater (e).

Appendix C

TEM images not included in Results

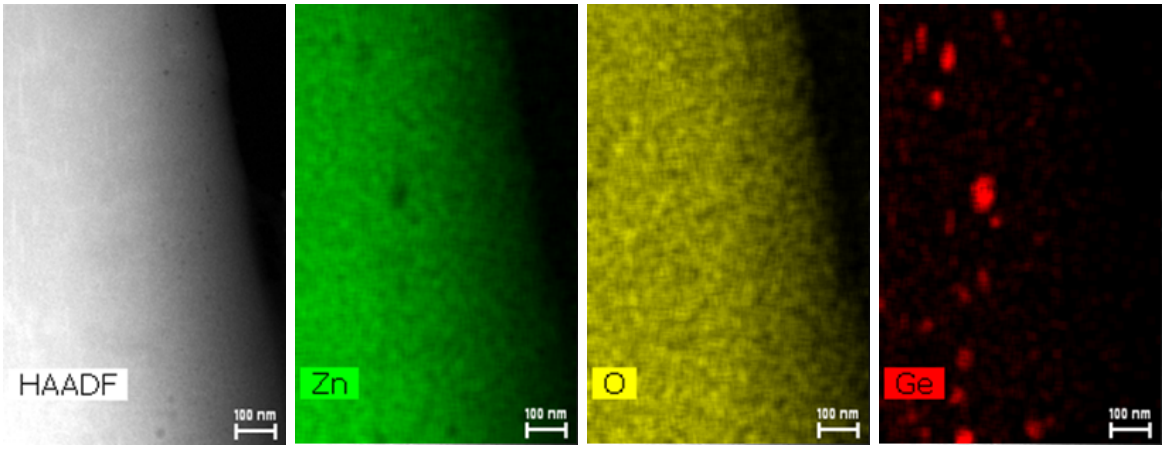

(a) TEM image (b) Zn signal (c) O signal (d) Ge signal

Figure C.1: TEM EDS results of the 800C sample.

References

[1] International Energy Agency, "World energy outlook 2015," November 2015.

[2] Intergovermental Panel on Climate Change, "IPCC fifth assesment report: Climate change," 2014.

[3] W. Shockley and H. J. Queisser, "Detailed balance limit of efficiency of p-n junction solar cells," *Journal of Applied Physics*, vol. 32, no. 3, pp. 510–519, 1961.

[4] T. Trupke, M. A. Green, and P. WÃ¼rfel, "Improving solar cell efficiencies by down-conversion of high-energy photons," *Journal of Applied Physics*, vol. 92, no. 3, pp. 1668–1674, 2002.

[5] P. T. Landsberg, H. Nussbaumer, and G. Willeke, "Band-band impact ionization and solar cell efficiency," *Journal of Applied Physics*, vol. 74, no. 2, pp. 1451–1452, 1993.

[6] C. Kittel and P. McEuen, *Introduction to solid state physics*. Wiley, 8th ed., 2005.

[7] P. Hemmer, *Faste stoffers fysikk*. Tapir forlag, 1987.

[8] D. J. Griffiths, *Introduction to quantum mechanics*. Pearson Education International, 2nd ed., 2005.

[9] B. Streetman and S. Banejee, *Solid state electronic devices*. Pearson Prentice Hall, 6th ed., 2006.

[10] A. P. Alivisatos, "Perspectives on the physical chemistry of semiconductor nanocrystals," *The Journal of Physical Chemistry*, vol. 100, no. 31, pp. 13226–13239, 1996.

[11] M. Beard and R. Ellingson, "Multiple exciton generation in semiconductor nanocrystals: Toward efficient solar energy conversion," *Laser & Photonics Reviews*, vol. 2, no. 5, pp. 377–399, 2008.

[12] Ü. Özgür, Y. I. Alivov, C. Liu, A. Teke, M. A. Reshchikov, S. Doğan, V. Avrutin, S.-J. Cho, and H. Morkoç, "A comprehensive review of ZnO materials and devices," *Journal of Applied Physics*, vol. 98, no. 4, p. 041301, 2005.

[13] M. D. McCluskey and S. J. Jokela, "Defects in ZnO," *Journal of Applied Physics*, vol. 106, no. 7, p. 1, 2009.

[14] B. Claflin and D. Look, *Zinc Oxide materials for electronic and optoelectronic Device application*, ch. Electrical Transport properties in Zinc Oxide, pp. 61–86. Wiley, 2011.

[15] H. Karzel, W. Potzel, M. Köfferlein, W. Schiessl, M. Steiner, U. Hiller, G. M. Kalvius, D. W. Mitchell, T. P. Das, P. Blaha, K. Schwarz, and M. P. Pasternak, "Lattice dynamics and hyperfine interactions in ZnO and ZnSe at high external pressures," *Phys. Rev. B*, vol. 53, pp. 11425–11438, May 1996.

[16] E. H. Kisi and M. M. Elcombe, "u parameters for the wurtzite structure of ZnS and ZnO using powder neutron diffraction," *Acta Crystallographica Section C*, vol. 45, pp. 1867–1870, Dec 1989.

[17] S. Pearton, D. Norton, K. Ip, Y. Heo, and T. Steiner, "Recent progress in processing and properties of ZnO," *Progress in Materials Science*, vol. 50, no. 3, pp. 293 – 340, 2005.

[18] D. C. Look, G. C. Farlow, P. Reunchan, S. Limpijumnong, S. B. Zhang, and K. Nordlund, "Evidence for native-defect donors in n-type ZnO," *Phys. Rev. Lett.*, vol. 95, p. 225502, Nov 2005.

[19] Y.-S. Kim and C. H. Park, "Rich variety of defects in zno via an attractive interaction between o vacancies and zn interstitials: Origin of n-type doping," *Phys. Rev. Lett.*, vol. 102, p. 086403, Feb 2009.

[20] S. F. J. Cox, E. A. Davis, S. P. Cottrell, P. J. C. King, J. S. Lord, J. M. Gil, H. V. Alberto, R. C. Vilão, J. Piroto Duarte, N. Ayres de Campos, A. Weidinger, R. L. Lichti, and S. J. C. Irvine, "Experimental confirmation of the predicted shallow donor hydrogen state in zinc oxide," *Phys. Rev. Lett.*, vol. 86, pp. 2601–2604, Mar 2001.

[21] J. M. Gil, H. V. Alberto, R. C. Vilão, J. Piroto Duarte, N. Ayres de Campos, A. Weidinger, J. Krauser, E. A. Davis, S. P. Cottrell, and S. F. J. Cox, "Shallow donor muonium states in ii-vi semiconductor compounds," *Phys. Rev. B*, vol. 64, p. 075205, Jul 2001.

[22] X. Chen, B. Xu, J. Xue, Y. Zhao, C. Wei, J. Sun, Y. Wang, X. Zhang, and X. Geng, "Boron-doped zinc oxide thin films for large-area solar cells grown by metal organic chemical vapor deposition," *Thin Solid Films*, vol. 515, no. 7-8, pp. 3753 – 3759, 2007.

[23] T. Makino, Y. Segawa, S. Yoshida, A. Tsukazaki, A. Ohtomo, and M. Kawasaki, "Gallium concentration dependence of room-temperature near-band-edge luminescence in n-type zno:ga," *Applied Physics Letters*, vol. 85, no. 5, pp. 759–761, 2004.

[24] K.-K. Kim, S. Niki, J.-Y. Oh, J.-O. Song, T.-Y. Seong, S.-J. Park, S. Fujita, and S.-W. Kim, "High electron concentration and mobility in al-doped n-zno epilayer achieved via dopant activation using rapid-thermal annealing," *Journal of Applied Physics*, vol. 97, no. 6, p. 066103, 2005.

[25] T. Yamada, T. Morizane, T. Arimitsu, A. Miyake, H. Makino, N. Yamamoto, and T. Yamamoto, "Application of low resistivity ga-doped zno films to transparent electromagnetic interference shielding material," *Thin Solid Films*, vol. 517, no. 3, pp. 1027 – 1031, 2008. 35th International Conference on Metallurgical Coatings and Thin Films (ICMCTF).

[26] M. N. Jung, J. E. Koo, S. J. Oh, B. W. Lee, W. J. Lee, S. H. Ha, Y. R. Cho, and J. H. Chang, "Influence of growth mode on the structural, optical, and electrical properties of in-doped zno nanorods," *Applied Physics Letters*, vol. 94, no. 4, p. 041906, 2009.

[27] L. S. Vlasenko and G. D. Watkins, "Optical detection of electron paramagnetic resonance for intrinsic defects produced in ZnO by 2.5-mev electron irradiation *in situ* at 4.2 k," *Phys. Rev. B*, vol. 72, p. 035203, Jul 2005.

[28] S. O. Kucheyev, J. S. Williams, C. Jagadish, J. Zou, C. Evans, A. J. Nelson, and A. V. Hamza, "Ion-beam-produced structural defects in ZnO," *Phys. Rev. B*, vol. 67, p. 094115, Mar 2003.

[29] L. Vines, J. Wong-Leung, C. Jagadish, V. Quemener, E. V. Monakhov, and B. G. Svensson, "Acceptor-like deep level defects in ion-implanted zno," *Applied Physics Letters*, vol. 100, no. 21, p. 2106, 2012.

[30] L. Vines, J. Wong-Leung, C. Jagadish, E. Monakhov, and B. Svensson, "Ion implantation induced defects in zno," *Physica B: Condensed Matter*, vol. 407, no. 10, pp. 1481 – 1484, 2012. Proceedings of the 4th South African Conference on Photonic Materials (SACPM 2011).

[31] A. Titov, P. Karaseov, and S. Kucheyev, "Furthering the understanding of ion-irradiation-induced electrical isolation in wide band-gap semiconductors," *Nuclear Instruments and Methods in Physics Research Section B: Beam Interactions with Materials and Atoms*, vol. 243, no. 1, pp. 79 – 82, 2006.

[32] S. O. Kucheyev, C. Jagadish, J. S. Williams, P. N. K. Deenapanray, M. Yano, K. Koike, S. Sasa, M. Inoue, and K.-i. Ogata, "Implant isolation of zno," *Journal of Applied Physics*, vol. 93, no. 5, pp. 2972–2976, 2003.

[33] L. Vines, E. V. Monakhov, R. Schifano, W. Mtangi, F. D. Auret, and B. G. Svensson, "Lithium and electrical properties of ZnO," *Journal of Applied Physics*, vol. 107, no. 10, p. 3707, 2010.

[34] K. M. Johansen, A. Zubiaga, I. Makkonen, F. Tuomisto, P. T. Neuvonen, K. E. Knutsen, E. V. Monakhov, A. Y. Kuznetsov, and B. G. Svensson, "Identification of substitutional Li in n-type ZnO and its role as an acceptor," *Phys. Rev. B*, vol. 83, p. 245208, Jun 2011.

[35] P. T. Neuvonen, L. Vines, B. G. Svensson, and A. Y. Kuznetsov, "Intrinsic point-defect balance in self-ion-implanted ZnO," *Phys. Rev. Lett.*, vol. 110, p. 015501, Jan 2013.

[36] A. Y. Azarov, K. E. Knutsen, P. T. Neuvonen, L. Vines, B. G. Svensson, and A. Y. Kuznetsov, "Impurity sublattice localization in ZnO revealed by Li marker diffusion," *Phys. Rev. Lett.*, vol. 110, p. 175503, Apr 2013.

[37] H. N. Riise, "Substrate, doping and annealing effects on sputtered zinc oxide thin films," Master's thesis, University of Oslo, 2013.

[38] T. Minami, "New n-type transparent conducting oxides," *MRS Bulletin*, vol. 25, pp. 38–44, 8 2000.

[39] R. Schifano, M. Schofield, L. Vines, S. Diplas, E. V. Monakhov, and B. G. Svensson, "Al and Si doping of sputtered ZnO thin films," *IOP Conference Series: Materials Science and Engineering*, vol. 34, no. 1, p. 012007, 2012.

[40] Q. You, H. Cai, K. Gao, Z. Hu, S. Guo, P. Liang, J. Sun, N. Xu, and J. Wu, "Highly transparent and conductive Al-doped ZnO films synthesized by pulsed laser co-ablation of Zn and Al targets assisted by oxygen plasma," *Journal of Alloys and Compounds*, vol. 626, pp. 415 – 420, 2015.

[41] Y. Liu, Y. Li, and H. Zeng, "ZnO-based transparent conductive thin films: Doping, performance, and processing„" *Journal of Nanomaterials*, vol. 2013, p. 196521, 2013.

[42] P. Gondoni, M. Ghidelli, F. D. Fonzo, V. Russo, P. Bruno, J. Martí-Rujas, C. Bottani, A. L. Bassi, and C. Casari, "Structural and functional properties of Al:ZnO thin films grown by pulsed laser deposition at room temperature," *Thin Solid Films*, vol. 520, no. 14, pp. 4707 – 4711, 2012. Proceedings of the EMRS 2011 Spring Meeting Symposium D: Synthesis, Processing and Characterization of Nanoscale Multi Functional Oxide Films III.

[43] T. Oga, Y. Izawa, K. Kuriyama, K. Kushida, and A. Kinomura, "Origins of low resistivity in Al ion-implanted ZnO bulk single crystals," *Journal of Applied Physics*, vol. 109, no. 12, p. 3702, 2011.

[44] J. L. Lyons, A. Janotti, and C. G. Van de Walle, "Role of Si and Ge as impurities in ZnO," *Phys. Rev. B*, vol. 80, p. 205113, Nov 2009.

[45] W. Körner and C. Elsässer, "Density functional theory study for polycrystalline ZnO doped with Si or Nb," *Phys. Rev. B*, vol. 83, p. 205306, May 2011.

[46] M. D. Schofield, "ZnO deposited by magnetron sputtering incorporating Si nanocrystals," Master's thesis, University of Oslo, June 2011.

[47] L.-W. Lai, C.-H. Liu, C.-T. Lee, L.-R. Lou, W.-Y. Yeh, and M.-T. Chu, "Investigation of silicon nanoclusters embedded in ZnO matrices deposited by cosputtering system," *Journal of Materials Research*, vol. 23, pp. 2506–2511, 9 2008.

[48] A. K. Das, P. Misra, and L. M. Kukreja, "Effect of Si doping on electrical and optical properties of ZnO thin films grown by sequential pulsed laser deposition," *Journal of Physics D: Applied Physics*, vol. 42, no. 16, p. 165405, 2009.

[49] J. Liu, X. Fan, C. Sun, and W. Zhu, "Transparent conductivity modulation of ZnO by group-IVA doping," *Chemical Physics Letters*, vol. 649, pp. 78 – 83, 2016.

[50] Y. Izawa, K. Matsumoto, K. Kuriyama, and K. Kushida, "Evaluation of zinc interstitial in si-ion implanted zno bulk single crystals by a rutherford backscattering study: An origin of low resistivity," *Nuclear Instruments and Methods in Physics Research Section B: Beam Interactions with Materials and Atoms*, vol. 268, no. 11 - 12, pp. 2104 – 2106, 2010. 19th International Conference on Ion Beam Analysis.

[51] Y. Lv, Y. Dai, K. Yang, Z. Zhang, W. Wei, M. Guo, and B. Huang, "Density functional investigation of structural, electronic and optical properties of Ge-doped ZnO," *Physica B: Condensed Matter*, vol. 406, no. 20, pp. 3926 – 3930, 2011.

[52] K. Kamioka, T. Oga, Y. Izawa, K. Kuriyama, and K. Kushida, "Characterization of the lattice defects in Ge-ion implanted ZnO bulk single crystals by rutherford backscattering:

Origins of low resistivity," *Nuclear Instruments and Methods in Physics Research Section B: Beam Interactions with Materials and Atoms*, vol. 307, pp. 366 – 369, 2013. The 18th International Conference on Ion Beam Modifications of Materials (IBMM2012).

[53] C. S. Garoufalis, "Optical gap and excitation energies of small Ge nanocrystals," *Journal of Mathematical Chemistry*, vol. 46, no. 3, pp. 934–941, 2009.

[54] M. Voros, S. Wippermann, B. Somogyi, A. Gali, D. Rocca, G. Galli, and G. T. Zimanyi, "Germanium nanoparticles with non-diamond core structures for solar energy conversion," *J. Mater. Chem. A*, vol. 2, pp. 9820–9827, 2014.

[55] C. Sevik and C. Bulutay, "Auger recombination and carrier multiplication in embedded silicon and germanium nanocrystals," *Phys. Rev. B*, vol. 77, p. 125414, Mar 2008.

[56] Y. Yu, G. Kim, B. Min, and S. Kim, "Optical characteristics of Ge doped ZnO compound," *Journal of the European Ceramic Society*, vol. 24, no. 6, pp. 1865 – 1868, 2004. Electroceramics VIII.

[57] T. Zheng, Z. Li, J. Chen, K. Shen, and K. Sun, "Transitions of microstructure and photoluminescence properties of the Ge/ZnO multilayer films in certain annealing temperature region," *Applied Surface Science*, vol. 252, no. 24, pp. 8482 – 8486, 2006.

[58] U. Pal, G. C. Segura, and O. Z. Corona, "Preparation of Ge/ZnO nanocomposites by radio frequency alternate sputtering," *Solar Energy Materials and Solar Cells*, vol. 76, no. 3, pp. 305 – 312, 2003. CANCUN 2001 Nanoscale materials & devices.

[59] D. Fan, Z. Ning, and M. Jiang, "Characteristics and luminescence of Ge doped ZnO films prepared by alternate radio frequency magnetron sputtering," *Applied Surface Science*, vol. 245, no. 1 - 4, pp. 414 – 419, 2005.

[60] M. Jiang, Z. Wang, and Z. Ning, "Study of structural and optical properties of Ge doped ZnO films," *Thin Solid Films*, vol. 517, no. 24, pp. 6717 – 6720, 2009.

[61] A. Ceylan, L. T. Yildirim, S. Ozcan, and S. I. Shah, "Rapid thermal annealing induced formation of Ge nanoparticles in ZnO thin films: A detailed SAXS study," *Materials Science in Semiconductor Processing*, vol. 34, pp. 8 – 13, 2015.

[62] A. Ceylan, A. E. Gumrukcu, N. Akin, S. Ozcan, and S. Ozcelik, "Formation of ST12 phase Ge nanoparticles in ZnO thin films," *Materials Science in Semiconductor Processing*, vol. 40, pp. 407 – 411, 2015.

[63] S. A. Campbell, *Fabrication Engineering at the Micro- and Nanoscale*. Oxford University Press, fourth ed., 2013.

[64] D. Morgan, ed., *Channeling: Theory, Observation and Applications*. Wiley, 1973.

[65] J. F. Ziegler, M. Ziegler, and J. Biersack, "SRIM - The stopping and range of ions in matter (2010)," *Nuclear Instruments and Methods in Physics Research Section B: Beam Interactions with Materials and Atoms*, vol. 268, no. 11 - 12, pp. 1818 – 1823, 2010. 19th International Conference on Ion Beam Analysis.

[66] P. van der Heide, *Secondary Ion Mass Spectrometry: An Introduction to Principles and Practices*. John Wiley & Sons, Inc., 2014.

[67] M. Birkholz, P. Fewster, and C. Genzel, *Thin Film Analysis by X-Ray Scattering*. WILEY-VCH, 2006.

[68] M. R. Sardela Jr., *Practical Materials Characterization*, ch. X-Ray Diffraction and Reflectivity, pp. 1–41. Springer New York, 2014.

[69] H. Bakhru, "Rutherford backscattering spectroscopy," in *Encyclopedia of Materials: Science and Technology (Second Edition)* (K. H. J. Buschow, R. W. Cahn, M. C. Flemings, B. Ilschner, E. J. Kramer, S. Mahajan, and P. Veyssière, eds.), pp. 8242 – 8247, Elsevier, 2nd ed., 2001.

[70] R. Egerton, *Physical principles of electron microscopy: An introduction to TEM, SEM, and AEM*. Springer US, 2005.

[71] D. Brandon and W. D. Kaplan, *Microstructural Characterization of materials*. Wiley, 2 ed., 2008.

[72] Y. Leng, *Materials characterization introduction to microscopic and spectroscopic methods*. John Wiley and sons (Asia) Pte Ltd, 2008.

[73] P. Blood and J. Orton, *The electrical characterization of semiconductors: Majority carrier and electron states*. Academic Press, 1992.

[74] L. J. van der Pauw, "A Method of Measuring Spesific Resistivity and Hall Effect of Discs of Arbitrary Shape," *Philips Research Reports*, vol. 13, pp. 1–9, 1958.

[75] P. M. Hemenger, "Measurement of high resistivity semiconductors using the van der pauw method," *Review of Scientific Instruments*, vol. 44, no. 6, pp. 698–700, 1973.

[76] K. T. Roro, G. H. Kassier, J. K. Dangbegnon, S. Sivaraya, J. E. Westraadt, J. H. Neethling, A. W. R. Leitch, and J. R. Botha, "Temperature-dependent hall effect studies of ZnO thin films grown by metalorganic chemical vapour deposition," *Semiconductor Science and Technology*, vol. 23, no. 5, p. 055021, 2008.

[77] P. Eyben, *Scanning spreading resistance microscopy : High resolution two-dimensional carrier profiling of semiconductor structures*. PhD thesis, KATHOLIEKE UNIVERSITEIT LEUVEN, 2004.

[78] J. A. Soares, *Practical Materials Characterization*, ch. Introduction to Optical Characterization of Materials, pp. 43–92. Springer New York, 2014.

[79] G. Gilliland, "Photoluminescence spectroscopy of crystalline semiconductors," *Materials Science and Engineering: R: Reports*, vol. 18, no. 3 - 6, pp. 99 – 399, 1997.

[80] G. Pettinari, A. Polimeni, and M. Capizzi, *Semiconductor Research: Experimental Techniques*, ch. Photoluminescence: A Tool for Investigating Optical, Electronic, and Structural Properties of semiconductors, pp. 125–170. Springer-Verlag Berlin Heidelberg, 1 ed., 2012.

[81] NANOSENSORS, part of the Nano World Group, "Nanosensors™CDT-NCHR." http://www.nanosensors.com/Conductive-Diamond-Coated-Tip-Non-Contact-Tapping-Mode-High-Resonance-Frequency-Reflex-Coating-afm-tip-NS-CDT-NCHR. (Visited May 11th 2016).

[82] L. Vines, E. V. Monakhov, J. Jensen, A. Y. Kuznetsov, and B. G. Svensson, "Effect of spatial defect distribution on the electrical behavior of prominent vacancy point defects in swift-ion implanted si," *Phys. Rev. B*, vol. 79, p. 075206, Feb 2009.

[83] B. G. Svensson, C. Jagadish, A. Hallén, and J. Lalita, "Generation of vacancy-type point defects in single collision cascades during swift-ion bombardment of silicon," *Phys. Rev. B*, vol. 55, pp. 10498–10507, Apr 1997.

[84] D. Look, H. Mosbacker, Y. Strzhemechny, and L. Brillson, "Effects of surface conduction on hall-effect measurements in ZnO," *Superlattices and Microstructures*, vol. 38, no. 4 - 6, pp. 406 – 412, 2005. E-MRS 2005 Symposium G: ZnO and Related MaterialsPart 1 2005 European Materials Research Society Spring Meeting.

[85] R. Schifano, E. V. Monakhov, L. Vines, B. G. Svensson, W. Mtangi, and F. D. Auret, "Defects in virgin hydrothermally grown n-type zno studied by temperature dependent hall effect measurements," *Journal of Applied Physics*, vol. 106, no. 4, p. 3706, 2009.

[86] B. K. Meyer, H. Alves, D. M. Hofmann, W. Kriegseis, D. Forster, F. Bertram, J. Christen, A. Hoffmann, M. Straßburg, M. Dworzak, U. Haboeck, and A. V. Rodina, "Bound exciton and donor-acceptor pair recombinations in zno," *physica status solidi (b)*, vol. 241, no. 2, pp. 231–260, 2004.

[87] E. Rossmanith, "Approximate calculation of multiple-diffraction patterns based on Renninger's kinematical 'simplest approach'," *Journal of Applied Crystallography*, vol. 33, pp. 921–927, Jun 2000.

[88] V. G. Dubrovskii, *Nucleation Theory and Growth of Nanostructures*. NanoScience and Technology, Springer Berlin Heidelberg, 1 ed., 2014.

[89] T. Mitsunaga, "X-ray thin-film measurement techniques," *The Rigaku Journal*, vol. 25, no. 1, pp. 7 – 12, 2009.

[90] K. S. Chan, L. Vines, L. Li, C. Jagadish, B. G. Svensson, and J. Wong-Leung, "Equilibrium shape of nano-cavities in H implanted ZnO," *Applied Physics Letters*, vol. 106, no. 21, 2015.

[91] J. Bang, Y.-S. Kim, C. H. Park, F. Gao, and S. B. Zhang, "Understanding the presence of vacancy clusters in ZnO from a kinetic perspective," *Applied Physics Letters*, vol. 104, no. 25, 2014.

[92] E. Marstein, A. Gunnæs, U. Serincan, S. Jørgensen, A. Olsen, R. Turan, and T. Finstad, "Mechanisms of void formation in Ge implanted SiO2 films," *Nuclear Instruments and Methods in Physics Research Section B: Beam Interactions with Materials and Atoms*, vol. 207, no. 4, pp. 424 – 433, 2003.

[93] S. Yamada, "Structure of germanium nanoparticles prepared by evaporation method," *Journal of Applied Physics*, vol. 94, no. 10, pp. 6818–6821, 2003.

[94] R. Dingle, "Luminescent transitions associated with divalent copper impurities and the green emission from semiconducting zinc oxide," *Phys. Rev. Lett.*, vol. 23, pp. 579–581, Sep 1969.

[95] D. Byrne, F. Herklotz, M. O. Henry, and E. McGlynn, "Unambiguous identification of the role of a single Cu atom in the ZnO structured green band," *Journal of Physics: Condensed Matter*, vol. 24, no. 21, p. 215802, 2012.

[96] J. R. Bellingham, W. A. Phillips, and C. J. Adkins, "Intrinsic performance limits in transparent conducting oxides," *Journal of Materials Science Letters*, vol. 11, no. 5, pp. 263–265, 1992.